Rapid Approximate Simulation Of Multiple Hydraulic Fractures

by

Cheng Cheng

B.E. in Geological Engineering, China University of Petroleum, China, 2011

B.S. in Geology, University of Missouri, USA, 2013

M.S. in Petroleum Engineering, University of Pittsburgh, USA, 2015

Submitted to the Graduate Faculty of the

Swanson School of Engineering in partial fulfillment

of the requirements for the degree of

Doctor of Philosophy

University of Pittsburgh

2020

UNIVERSITY OF PITTSBURGH

SWANSON SCHOOL OF ENGINEERING

This dissertation was presented

by

Cheng Cheng

It was defended on

October 21, 2020

and approved by

Robert M. Enick, Ph.D., Professor, Department of Chemical and Petroleum Engineering

Badie I. Morsi, Ph.D., Professor, Department of Chemical and Petroleum Engineering

William Slaughter, Ph.D., Associate Professor, Department of Mechanical Engineering & Materials Science

Dissertation Director: Andrew P. Bunger, Ph.D., Associate Professor, Department of Civil and Environmental Engineering & Department of Chemical and Petroleum Engineering

Rapid Approximate Simulation Of Multiple Hydraulic Fractures

Cheng Cheng, PhD

University of Pittsburgh, 2020

Hydraulic fracturing enables oil and gas extraction from low-permeability reservoirs, but there remains a need to reduce the environmental footprint. Resource use, contaminant-bearing flowback water, and potential for induced seismicity are all scaled by the volume of injected fluid. Furthermore, the greenhouse gas emissions associated with each extracted unit of energy can be decreased by improving resource recovery. To minimize fluid use while maximizing recovery, a rapidly-computing model is developed and validated to enable the thousands of simulations needed to identify opportunities for optimization. Lower pumping pressure approaches that minimize pressure loss through the wellbore perforations combined with non-uniform spacing are shown to be capable of substantially reducing fluid consumption and/or increasing created fracture surface area when the stress variation is mainly from fracture interaction instead of in-situ stress. When in-situ stress variation is dominant, “limited entry” methods promote more uniform growth but with higher pumping pressures and energy consumption.

Table of Contents

List of Tables

List of Figures

Preface

This material is based upon work supported by the University of Pittsburgh Center for Energy, Swanson School of Engineering, Department of Chemical and Petroleum Engineering, and Department of Civil and Environmental Engineering. Additional support for recent advances to this work was provided by the National Science Foundation under Grant No. 1645246.

I. Introduction

Hydraulic fracturing (HF), a well stimulation technique, serves as an important industrial application in mining, waste disposal, and enhanced geothermal systems Jeffrey et al. (2009); Abou-Sayed et al. (2003); Regenauer et al. (2015). The most well-known application is increasing the recovery of shale gas and oil, named that found trapped within unconventional reservoir that ordinarily have insufficient permeability to allow significant fluid flow to a wellbore. In 2019, about 75% of total U.S. dry natural gas EIA (2020) and 63% of total U.S. crude oil production EIA (2020) is provided by the shale gas and shale oil extracted through hydraulic fracturing. The shale formation is fractured by the pressurized liquid with carried granular materials known as proppants, which hold fractures open to allow hydrocarbon flow more freely through the fractures when hydraulic pressure is removed from the well. The resulting improved conductivity stimulates more oil or gas recovered from wells. For vertical wells, there is 70-year history of hydraulic fracturing used in this way and significant progression is made in horizontal well fracturing specifically for the unconventional resources in last several decades Carl and Michael (2010). Basically all unconventional reservoirs are treated by horizontal wells in widely used manner, a sequential hydraulic fracturing from the "toe" to the "heel" of the well (see description in e.g. Lecampion and Desroches (2015)). Several clusters are uniformly perforated within each of these sequential "stages" as reservoir entry points, where the fluid is injected though Figure I.1. This process is repeated stage by stage though lateral length, the productive portion of wellbore.

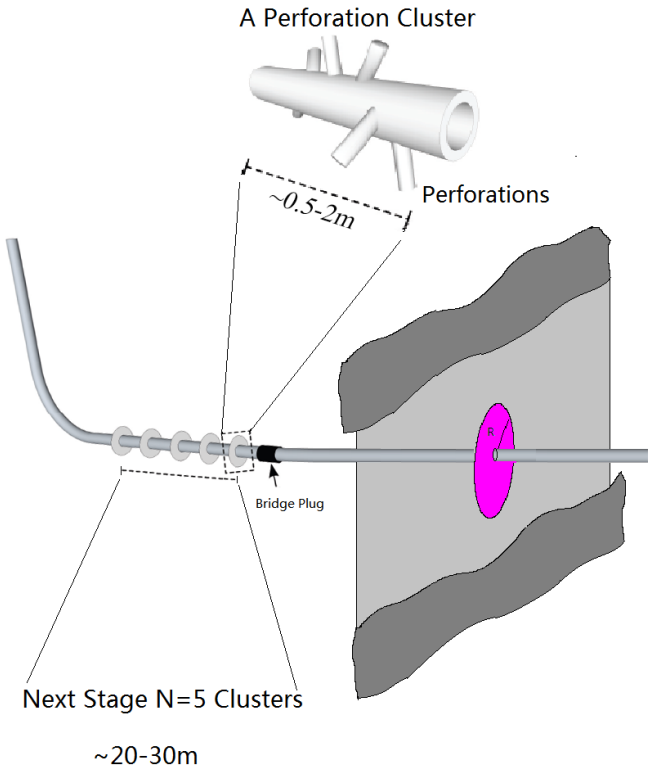

Figure I.1: Sketch of perforation clusters, modified from Lecampion and Desroches (2015).

Ideally, injected fluid should distribute uniformly among the clusters, stimulating uniform crack growth Figure I.2a. However the analysis of production logs over several basins tends to show that between 20 to 40 percent of perforation clusters do not contribute to production Miller et al. (2011), meaning crack growth is not uniform as intended Figure I.2b.

a)

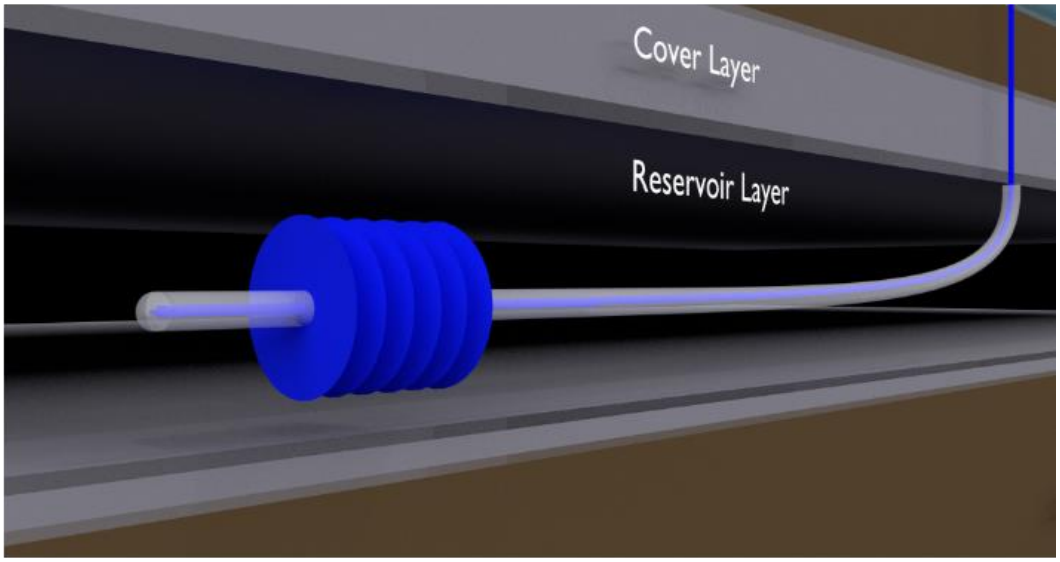

b)

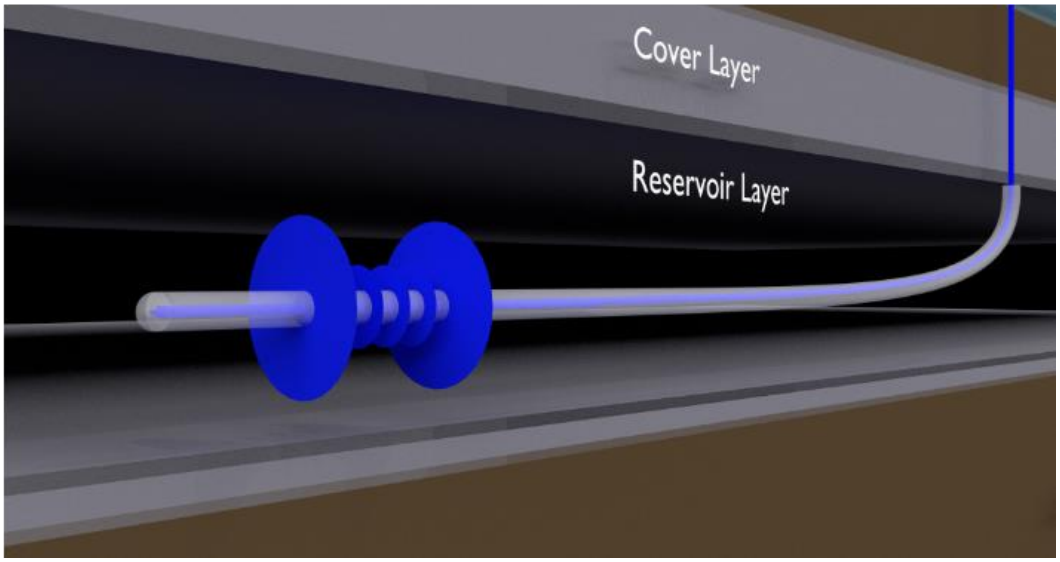

Figure I.2: Illustration of multiple, simultaneous HFs in one stage showing. (a) Ideal, uniform result, and (b) Result in which central fractures are suppressed.

This phenomenon is mainly due to the non-uniformity of reservoir properties also called variability, which could be identified as two types. The first type is human induced due to the fluid injection Sesetty and Ghassemi (2013); Abass et al. (2009); Fisher et al. (2004). When fluid flow with increasing of the crack opening, the internal net pressure act on the fracture surface performs as a compressive stress on the nearby fractures. Especially when spacing between entry points, typically perforation clusters, is small relative to the final fracture length and/or height. The fracture that is impacted the least by compressive stress interaction will be favored with more crack growth (Fig. 1b as previously discussed by e.g. Germanovich et al. (1997); Fisher et al. (2004); Abass et al. (2009); Olson (2008); Kresse et al. (2013); Wu and Olson (2013); Lecampion et al. (2015) For example, consider one stage that includes three fractures. In this case, growth of the outer two fractures in the array would typically dominate. Meanwhile, locally elevated compressive stress sourced from outer fracture will suppress the propagation of inner fractures. Instead of the ideal case of uniform hydraulic fracture growth (Figure I.2a), non-uniform hydraulic fractures will be achieved (e.g. Fisher et al. (2004); Abass et al. (2009); Meyer and Bazan (2011); Germanovich et al. (1997)). This issue has become well-recognized and known as “stress shadowing” (see e.g. field evidence in Bunger and Cardella (2015)).

The naturally varied rock property due to the sedimentation and tectonic movement (8-9) is another factor responsible for the non-uniform hydraulic fracture growth. For example, if considering 10% variation for 30 MPa in-situ stress along the well e.g. Baihly et al. (2010); Cipolla et al. (2011), there will be 3 MPa of stress variability. As a comparison, the stress variability induced by interaction stress is usually less than 1 MPa. So, for some cases, the in-situ stress dominates the stress distribution and further manipulates the flow distribution into each fracture. Based on the non-uniform flow rate, the non-uniformity of fractures is strengthened by heterogeneous toughness, elasticity, and other rock properties.

Due to the non-uniformly stimulated reservoir, the oil or gas recovery is lowered. There is not only a monetary, but also an environmental and societal cost to every well, scaled by the efficiency of resource usage Vengosh et al. (2014); Entrekin et al. (2018); Ellsworth (2013). The injection pressure is powered by the pump with greenhouse gas emissions, also exist in drilling and completion of wells. The non-uniformity induced low "estimated ultimate recovery" (EUR) increases the greenhouse gas (GHG) emissions per unit of energy produced (i.e. kg CO2eq/MWh) (Laurenzi and Jersey (2013); Vafi and Brandt (2016)). The use of water, thickening agent, proppants, and other additives in fracking fluid is substantial because between 8-40 million liters (2-10 million gallons) of water is used to stimulate a single well Kargbo et al. (2010). Hence, an overall commonality is that water management presents one of the greatest challenges to both the present and future development of onshore oil and gas development throughout the world. Water-related challenges and impacts can include resource scarcity (e.g., Smakhtin et al. (2004); Scanlon et al. (2014); Kondash et al. (2018)), flowback of contaminated water (e.g., Shrestha et al. (2017); He et al. (2017); Sun et al. (2013); Xiong et al. (2016)), pollution associated resource transportation (e.g., Brantley et al. (2018); Mitchell et al. (2013); Vengosh et al. (2014); Entrekin et al. (2018)),

and injection-induced seismicity (e.g., Ellsworth (2013); Fischer (2011); Guglielmi et al. (2015)). These, and indeed most water-related challenges, risks, and impacts essentially scale in magnitude with the volume of fluid used for hydraulic fracturing (Vengosh et al. (2014); Entrekin et al. (2018); Ellsworth (2013)).

The inhibited resource efficiency, such as energy and water usage, could get optimized through maximizing recovery rate by ensuring the best-possible uniformity. Hydraulic fracturing simulator certainly indicates the capability to identify approaches to uniformly stimulating the reservoir rock (see e.g. Lecampion et al. (2015); Peirce and Bunger (2015)). Recently, a model called ILSA ("Implicit Level Set Algorithm") developed by Peirce and Detournay (2008) was extended to a parallel-planar HF model with full 3D elastic coupling between the simultaneously propagating fractures by Peirce and Bunger (2015). Although ILSA is a benchmark in this research area with high fidelity, it requires a week or more to compute a single multi-fracture result on typical reservoir length and time scales. Optimization of HF design requires hundreds or thousands of model runs. Hence, the simulations' computational intensity makes it not practical with this or other models with run times on the order of tens of hours to days.

The goal of this research is to quantify the growth of multiple fracture by developing a new algorithm used in simulation, enabling the validation with benchmark model but with orders higher computation speed. Application of the model illustrates the promising potential for optimizing the production of hydrocarbon and the resource efficiency. This research is divided into the following sections.

II. Reduced Order Model For Simultaneous Growth Of Multiple Closely-Spaced Radial Hydraulic Fractures

A. Preamble

With the intention to evaluate possible optimization through thousands of simulations runs, a simulator that could benchmarked with high fidelity models at high computation speed is in need. Approximate model "C2Frac", which is previously demonstrated the feasibility and basic concept Cheng and Bunger (2016), shows good agreement with ILSA II. It is the use of asymptotic solution and energy balance, semi-analytical method could be built and greatly improves the calculation efficiency with much less time required for each evaluation. However, in this prototype model, the HFs are restricted to remain small in radius compared to their separation, not accounting for near field stress interaction. The C2Frac estimates diverge from fully coupled benchmark solutions when the fracture radii become similar to the fracture spacing. The necessary model improvement is made by developing a novel algorithm using the Sneddon solution for the stresses around of circular fracture. Hence, the approach accurately describe the stress distribution in neighboring cracks. The asymptotic solution of pressure is also updated correspondingly, concerning the spatial varied interaction stress. Following new algorithm, C3Frac could approximate with fully coupled ILSA II regardless the radii and spacing and capture the complex behavior when fractures transit from far field to near field. The model, and its validation are detailed in Part II with a brief overview provided here Cheng (2019a).

B. Abstract

A new reduced order model (ROM) provides rapid and reasonably accurate prediction of the complex behavior of multiple, simultaneously growing radial hydraulic fractures. The method entails vastly reducing the degrees of freedom typically associated with fully-coupled simulations of this multiple moving boundary problem by coupling together an approximation of the influence of the stress interaction among the fractures ("stress shadow") with an approximation of fluid flow and elasticity, ensuring preservation of global volume balance, global energy balance, elasticity, and compatibility of the crack opening with the inlet fluid flux. Validating with large scale ("high-fidelity ") simulations shows the ROM solution captures not only the basic suppression of interior hydraulic fractures in a uniformly-spaced array due to the well-known stress shadowing phenomenon, but also complex behaviors arising when the spacing among the hydraulic fractures is non-uniform. The simulator's usefulness is demonstrated through a proof-of-concept optimization whereby non-uniform spacing and stage length are chosen to maximize the fracture surface area and/or the uniformity of growth associated with each stimulation treatment.

C. Introduction

Reduced order models (ROMs) have a great potential for enabling optimization and uncertainty quantification for hydraulic fracturing. However, ascertaining the essential ingredients necessary for a reasonably accurate and suitable efficient ROM for simulating systems of multiple, simultaneously-growing hydraulic fractures remains a challenging and open problem.

Hydraulic fracturing (HF) is a well stimulation technique used in many industrial applications include mining, waste disposal, and enhanced geothermal systems Jeffrey et al. (2009); Abou-Sayed et al. (2003); Regenauer et al. (2015). The most well-known application is its use for increasing the rate at which oil and gas can be extracted from wells. In this application, pressurized fluid drives growth of cracks through the reservoir rock, carrying granular proppant that is left behind in the created fractures. The resulting high conductivity pathways promote an increased flow of hydrocarbons from the reservoir formation towards the well (as described in further detail by e.g. Economides and Nolte (2000)). Both vertical and horizontal wells are stimulated in this way, with vertical well simulation comprising most cases over the 70 year history of hydraulic fracturing and horizontal well fracturing comprising the essential advance for unlocking unconventional (low-permeability) resources in the past two to three decades Carl and Michael (2010). Essentially all horizontal wells in unconventional reservoirs (such as shale gas and oil) are treated by hydraulic fracturing, and the most common approach is to stimulate in a sequential manner from the "toe" to the "heel" of the well (see description in e.g. Lecampion and Desroches (2015)). Within each of these sequential "stages", multiple clusters of perforations comprise the reservoir entry points, with the intention that injected fluid is reasonably uniformly distributed among these possible entry points, thereby uniformly stimulating the reservoir rock. Although such a multistage technique has enabled tremendous cost savings, analysis of production logs over several basins tends to show that between 20 to 40 percent of perforation clusters do not contribute to production Miller et al. (2011), indicating current simulation strategies are highly non-optimal. One contributing factor is the non-uniformity of reservoir properties, including the in-situ stresses along the well e.g. Baihly et al. (2010); Cipolla et al. (2011). Another factor is almost certainly the widely recognized phenomenon known of "stress shadowing" (see e.g. field

evidence in Bunger and Cardella (2015)). Stress shadowing refers to suppression of some HFs as a result of the compressive stresses exerted on them by other, nearby HFs (e.g. Fisher et al. (2004); Abass et al. (2009); Meyer and Bazan (2011)). One result is that the ideal case of uniform hydraulic fracture growth (Figure II.1a) is probably never achieved. Instead, some hydraulic fractures are suppressed due to the presence of locally elevated compressive stress (Figure II.1b as previously discussed by e.g. Germanovich et al. (1997); Fisher et al. (2004); Abass et al. (2009); Olson (2008); Kresse et al. (2013); Wu and Olson (2013); Lecampion et al. (2015)).

a)

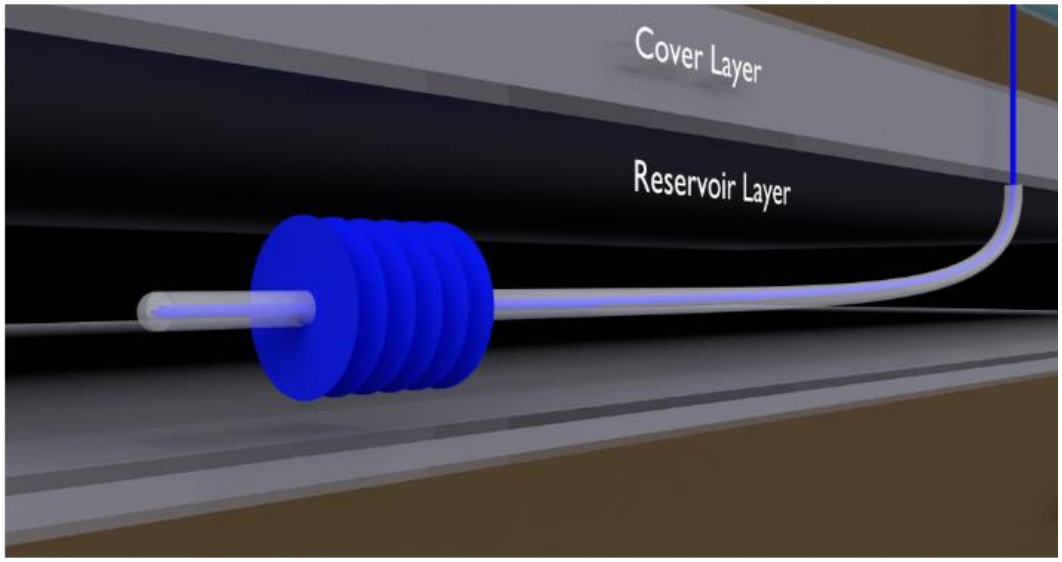

b)

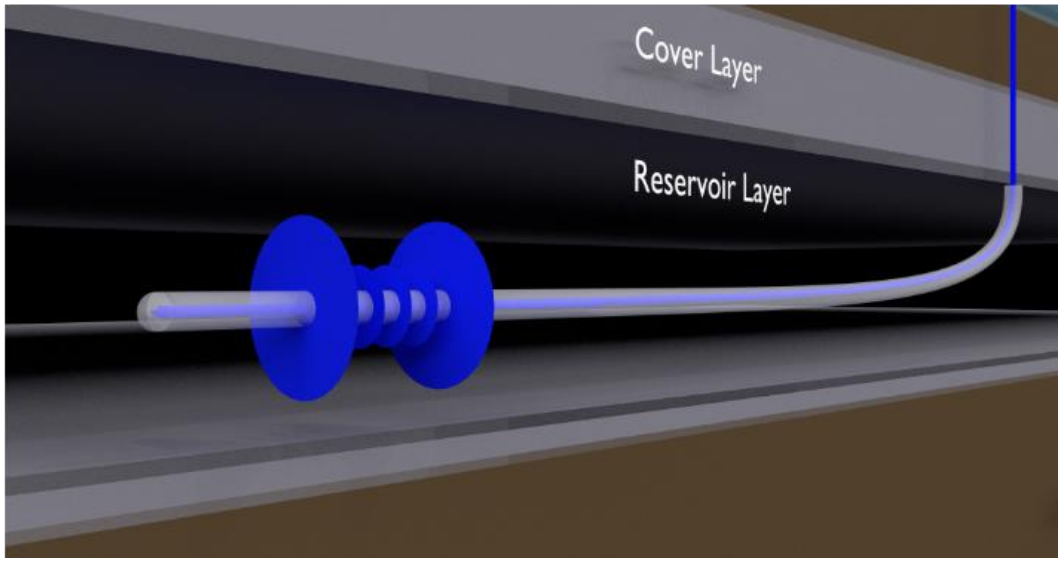

Figure II.1: Illustration of multiple, simultaneous HFs in one stage showing. (a) Ideal, uniform result, and (b) Result in which central fractures are suppressed.

While there are certainly demonstrations showing use of hydraulic fracture simulators to identify approaches that improve uniformity of stimulation (see e.g. Lecampion et al. (2015); Peirce and Bunger (2015)), optimization is challenging because of the simulations' computational intensity. Overcoming this challenge has opened a growing area of interest in generating reduced order models for hydraulic fractures, for example following formalisms that involve order reduction via an empirical search for eigenfunction bases that can be used to capture system behavior over some subdivision of the time domain (Izadi and Dubljevic (2013); Izadi and Dubljevic (2013); Sidhu et al. (2018); Narasingam and Kwon (2017); Narasingam et al. (2017)). Here we follow a different approach, but the goal is the same, namely, to obtain a reduced order model that provides a useful approximation to the full model, and with the key feature being capturing interaction of simultaneously growing hydraulic fractures.

While there are several possible threads in the literature that aim generally at simulating and optimizing multistage completions, here we will briefly introduce the background most relevant to the current contribution. The Implicit Level Set Algorithm, or "ILSA" Peirce and Detournay (2008) was extended by Peirce and Bunger (2015) for multiple parallel-planar HFs, including full 3D elastic coupling between the simultaneously propagating fractures ("ILSA II"). This simulator has been used to demonstrate that the stress shadow effect can be reduced with appropriate placement of interior HFs close to the outer HFs to inhibit their growth relative to the other fractures in the array.

Although ILSA II is a fully coupled benchmark simulator (to use terminology commonly contrasted with ROMs, we also can call this a "large scale" or "high-fidelity" model), implementing state of the art approaches to enable accurate calculations on very coarse meshes, the model can require several days, and sometimes over one week, to compute a multi-fracture

result at typical reservoir length and time scales (note timing is for single node calculations, ~2.5 GHz processor speed). Hence, optimization of HF design, which can require hundreds or thousands of model runs, is not practical with this or other models with run times on the order of tens of hours to days. Similarly, uncertain quantification, which also can require thousands or model evaluations, is not typically possible. A first step is, therefore, addressing the need for rapid, even if approximate, simulation. Such ROM simulators can be used to do broad explorations of high dimensional parametric spaces, identifying combinations of parameters, which can be examined in detail by a few, fully-coupled simulations.

We previously demonstrated the feasibility and basic concept of a new HF simulator, called "C2Frac", which very rapidly estimates the growth of an array of HFs Cheng and Bunger (2016). In this prototype model, the HFs are restricted to radial, planar growth - as in the current version presented here - but under the additional limitation that fractures remain small in radius compared to their separation. The method uses semi-analytical HF solutions (after Savitski and Detournay (2002)), coupling a far field approximation of the interaction stress via an overall energy balance. In this way, the model predicts each HF's aperture $W_i(t)$, net pressure $P_i(t)$, radius $R_i(t)$, and inflow rate $Q_i(t)$ for different choices of uniform or non-uniform spacing among N HFs. The validating shows good agreement between C2Frac and ILSA II benchmarks, however, because of the use of a far-field approximation of the interaction stress between the HFs, the C2Frac estimates diverge from fully coupled benchmark solutions when the fracture radii become similar to the fracture spacing. Additionally, because the prototype model does not account for near field stress interaction, it does not capture some of the complex behaviors predicted by fully coupled simulations when the fracture spacing is non-uniform. In particular, the previous model cannot capture when the interior fractures switch from being suppressed to accepting the majority of the

fluid, as observed in fully-coupled simulations by Peirce and Bunger (2015). Simulating this phase is essential for obtaining accurate predictions, but it can only be captured when the impacts of near field stress interaction between very closely spaced fractures are appropriately modeled.

The necessary model improvements are here enabled by developing a new algorithm leading to numerical simulations approximating the benchmark solutions for all times, regardless of fracture radius and spacing, while running 10^3-10^6 times faster than the fully coupled benchmark simulator. In this paper, the new model, called "C3Frac", is developed and validated. We begin by presenting the governing equations. We then introduce a new approach to approximation of the interaction stress from each fracture based on a uniformly pressurized crack with equal volume and radius to the actual HF. Next, we describe an interaction stress coupled elasticity function, which preserves volume balance by ensuring the elasticity solution is consistent with the inlet flow rate boundary condition. Then, the system of governing equations is completed by requiring that the fluid is partitioned among the multiple entry points so as to maintain equality of the wellbore pressure predicted for each fracture while also conserving the fluid injected into the wellbore. These final conditions are required by both the fully coupled and approximate simulator. In the case of the fully coupled simulator the wellbore pressure is predicted by carefully simulating fluid flow at all locations within the fracture so as to obtain an accurate estimate of the pressure at the fracture inlet (wellbore). In contrast, the approximate simulator approximates the fluid flow in a manner preserving the main contribution to viscous energy dissipation and then predicts the inlet pressure for each fracture using global energy balance.

After presenting the model, we next show how well it approximates the fully coupled simulations. Following this validating, numerical experiments illustrate cases for uniform and non-uniform spacing designs to indicate how spacing effects the hydraulic fracture growth. Thus, we

utilize the new C3Frac model to search for optimized HF scenarios in terms of created fracture surface area, providing examples of optimized designs for different stage lengths, inflow rates, and pumping times. The work concludes with a demonstration of the benefits of optimization and the potential for non-uniform fracture spacing to promote multiple methods for promoting multiple HF growth.

D. Governing Equations

In a typical HF treatment of an oil or gas well, one or more fractures is/are created by injection of fluid. The fracture is initiated within a rock formation that contains the hydrocarbons (the reservoir), and propagates perpendicularly to the orientation of the minimum in situ confining stress σ_o. Here the HFs are considered to grow transversely to a horizontal well, as illustrated by Figure II.1. This model accounts for the growth of N fractures within a single stage and, for now, neglects the stresses induced by the previous stages Bunger et al. (2014); Roussel et al. (2012); Sesetty and Ghassemi (2013), noting that these can be important especially if they induce substantial fracture curving. Furthermore, we note that if the fracture curving is negligible (see Bunger et al. (2012) for one approach for ascertaining if the curving will be important), then these previous-stage stresses can be accounted for with a straightforward extension of the approach wherein the stresses from fractures in the previous stage(s) are accounted for in the same manner as we account for fracture induced stresses within the same stage. The model, then, considers an array of N planar fractures distributed within one stage of length Z (see Figure II.2). Hence, the spacing h_k, k=1,..N-1 between each of the fractures is such that:

$$Z = \sum_{k=1}^{N-1} h_k \tag{II.1}$$

Growth of the array of HFs is driven by injection of an incompressible fluid from a wellbore at the center of each of the radially-growing HFs (Figure II.1). The rate provided to each HF is variable and determined as a part of the solution, however, to conserve fluid in the wellbore, the influx rates to each fracture must always sum to a constant total volumetric rate Q_o. This is to say that we consider the total fluid injection rate provided to the wellbore to be a constant, but the partitioning of this fluid to each fracture to be transient. The HFs are taken to propagate quasi-statically (i.e. well below the speed of sound for the rock) in a permeable, linear elastic rock characterized by $E' = E/(1-\nu^2)$ for Young's modulus E, Poisson's ratio ν, and toughness $K' = (32/\pi)^{1/2}K_{IC}$ for fracture toughness K_{IC} (after Savitski and Detournay (2002)). Solution to the problem consists of determining the partitioning of the influx to each HF as well as each HF's crack width, net pressure, and radius. Several additional assumptions are introduced to simplify this problem:

(I) Crack propagation follows linear elastic fracture mechanics (LEFM), which assumes that the material follows a linear elastic stress-strain relationship everywhere except for in a very small "process zone" near the crack tip Rice (1968). Crack propagation will occur when the opening-mode stress intensity at the crack tip attains the material fracture toughness Irwin (1957); Kanninen and Popelar (1985).

(II) Lubrication theory is used to describe laminar flow of a Newtonian fluid within the fracture (e.g. Batchelor (1976)).

(III) The rock is impermeable, and hence the leak off term is not considered in this study (i.e. it is not considered in the fluid mass balance of Equation II.2).

(IV) All HFs grow radially and parallel to one another.

(V) Gravitational force is neglected both in the elasticity and fluid flow equations.

(VI) The fluid front is coincident with the crack front, meaning the lag between the fluid front and fracture tip is very small compared to the fracture radius, which is valid under typical high confinement conditions encountered in reservoirs Bunger et al. (2012).

(VII) The far field in situ stress σ_o is uniform and constant, although the total compressive stress acting on each fracture is, of course, non-uniform and non-constant due to the interaction with its neighbors.

For a detailed discussion of several of these common assumptions in hydraulic fracture modeling, especially regimes of small versus large viscosity and small versus large leakoff, see Detournay (2004). We also idealize that, for the entire period of growth, the fractures remain planar and radial, as illustrated by Figure II.2. Again we note that this idealization neglects deviation of the fracture path either due to interaction with natural fractures or due to stress shadowing from other HFs Kresse et al. (2013), Sesetty and Ghassemi (2013), Bunger et al. (2012), Olson and Pollard (1989), Weng (1993), Olson (1995), Olson and Dahi-Taleghani (2009). It also neglects the presence of a height growth barrier which is present in most reservoirs and leads to a transition from radial to blade-like growth (called the "PKN" geometry after Perkins and Kern (1961); Nordgren (1972). Based on similar arguments to those described in detail by Peirce and Bunger (2015), this model is expected to remain valid for gently curving HFs, as long as the impact of the curving on the energy required to drive the HFs represents a small correction to the leading order term(s) used by this model. However, it is also clearly possible that the stress interaction will be affected by the curving and, in the context of a coupled model where small perturbations can sometimes be amplified, it is possible that scenarios in which the curving significantly impacts

behavior will be discovered as a part of future research. Furthermore, ongoing efforts will aim at capturing the transition to PKN-like growth, but the present model is limited to the radial growth period that persists as long as the fracture radius does not exceed the lithologically-limited fracture height. An additional, important limitation in scope is that here the near-wellbore pressure losses due to fracture tortuosity and/or perforation friction and pressure loss associated with fluid flow through the inside of the casing between the perforation clusters are neglected. These, too, are readily accounted for, through incorporated into the power balance as one power contribution to preserve the inlet pressure condition Cheng et al. (2016); Lecampion and Desroches (2015), but not the focus of this paper. Finally, accounting for interaction with natural factures is a challenge which remains for future research and is not addressed here.

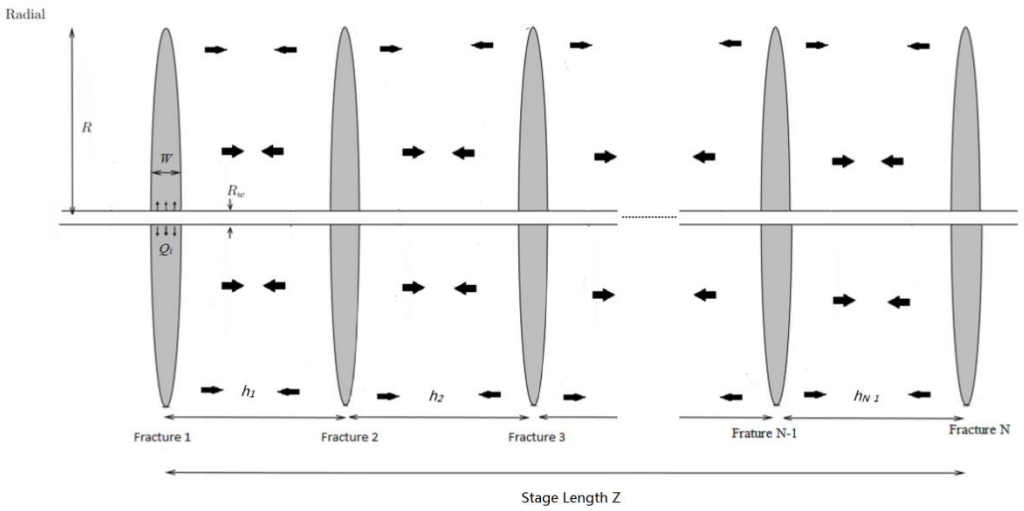

Figure II.2: Geometry of the multiple HF problem for N HFs distributed within a stage of length Z and with fracture spacing h_k . The arrows illustrate the interaction stresses between fractures.

Having established the simplifying assumption, we return to the description of the model itself. For an array of N fractures, there are $5N$ unknowns. They are, for the i^{th} fracture, the opening $w_i(r,t)$, fluid pressure $p_{f(i)}(r,t)$, fracture radius $R_i(t)$, elastic interaction stress from the other fractures $\sigma_{I(i)}(r,t)$, and inlet flow rate $Q_i(t)$, where $i=1,\ldots,N$ (see Figure II.2). These quantities are governed by a manifestation of a classical HF model bringing together elastic deformation of the HF, fluid mass balance, laminar fluid flow, and an LEFM crack propagation criterion Khristianovich and Zheltov (1955), with an addition of an elastic expression of the interaction stress (after Sneddon (1951)) and a condition of pressure and fluid continuity within the wellbore (after e.g. Peirce and Bunger (2015)). Specifically, the model begins firstly with fluid continuity (mass balance) which, based on the assumptions of an incompressible fluid and an impermeable rock, is given for the i^{th} fracture by

$$\frac{\partial w_i(r,t)}{\partial t} + \frac{1}{r}\frac{\partial r q_i(r,t)}{\partial r} = 0 \tag{II.2}$$

where q is the flow rate across the fracture aperture (width), that is, $q = \langle v \rangle w$ for mean velocity $\langle v \rangle$.

Secondly, the elastic body is considered to be deformed by a traction T_i acting across the surfaces of each fracture. In the case of interacting circular cracks, the elasticity relationship between local normal traction T and width w is given by Sneddon (1951)

$$w_i(r,t) = \frac{8R_i(t)}{\pi E'}\mathcal{F}\{\rho_i, T_i(\rho_i,t)\} \quad \rho_i = r/R_i(t) \tag{II.3}$$

Here the non-local integral operator $\mathcal{F}$ and internal traction acting on each fracture T_i are given in Section 3.

Thirdly, according to lubrication theory for an incompressible Newtonian fluid Batchelor (1967), the radial flux $q_i(r,t)$ is proportional to the gradient of the fluid pressure via the classical Poiseuille law, that is

$$q_i(t) = -\frac{w_i(r,t)^3}{12\mu}\frac{\partial p_{f(i)}(r,t)}{\partial r} \tag{II.4}$$

where μ is the dynamic viscosity. Fourthly, according to Assumption (I) (linear elastic fracture), the crack always propagates in limit equilibrium, and hence the fracture propagation criterion takes the form

$$K_I = K_{Ic} \tag{II.5}$$

where K_I denotes the mode I (opening) stress intensity factor and K_{Ic} the model I fracture toughness. For the radial fracture, K_I can be expressed as Rice (1968)

$$K_I = 2\sqrt{\frac{R_i(t)}{\pi}}\int_0^1 \frac{T_i(\rho_i,t)}{\sqrt{1-{\rho_i}^2}}\rho_i d\rho_i \tag{II.6}$$

Fifthly, injection of fluid from the borehole is imposed at the center of each fracture. Hence, based on mass balance considerations, the boundary condition at the inlet of the crack is given by the source condition for each fracture

$$2\pi \lim_{r\to R_w} r q_i(r,t) = Q_i(t) \tag{II.7}$$

where R_w is the radius of the wellbore.

Sixthly, the boundary conditions at the crack tip are given by zero opening and zero flux $w_i(R_i,t)=0$, $q_i(R_i,t)=0$ Detournay (2004); Detournay and Peirce (2014) the initial condition ($t=0$) is given by $R_i=0$, $w_i=0$, and $p_{f(i)}=0$.

Note that with these initial and boundary conditions, the fluid continuity Equation II. 2 can be integrated to give a global mass balance equation which, although it does not provide an additional independent equation (it follows directly from equations already defined), is useful for simulation. This equation is given by

$$\int_0^t Q_i(t)dt = 2\pi \int_0^{R_i(t)} w_i(r,t) r dr \tag{II.8}$$

Also, by substitution of the Poiseuille Equation II.4 into the continuity Equation II.2, we obtain the Reynold's lubrication equation given by

$$\frac{\partial w_i(r,t)}{\partial r} = \frac{1}{12\mu}\frac{1}{r}\frac{\partial}{\partial r}\left(r w_i(r,t)^3 \frac{\partial p_{f(i)}(r,t)}{\partial r}\right) \tag{II.9}$$

Recall that 5N equations are required to solve for the 5N unknown quantities: fracture opening $w_i(r, t)$, fluid pressure $p_{f(i)}(r, t)$, radius $R_i(t)$, elastic interaction stress from the other fractures $\sigma_{I(i)}(r, t)$, and inlet flow rate $Q_i(t)$. So far we have defined 3N equations which are provided by the coupled system of partial-integro-differential equations from Reynolds lubrication equation for laminar fluid flow (Equation II.9), elasticity (Equation II.3), and propagation (Equation II.5). An additional N equations are obtained from the interaction stresses which occur when multiple hydraulic fractures grow in close proximity to one another. An approximation of these stresses is described in Section 3.1. Hence, the system is closed firstly by the N-1 equations given by the constraint that the pressure is the same at every entry point (because they are tied by the wellbore)

$$p_{f(1)}(R_w, t) = p_{f(2)}(R_w, t) = \cdots = p_{f(N)}(R_w, t) \tag{II.10}$$

Note that a perforation friction loss term can be included Cheng et al. (2016); Lecampion and Desroches (2015), leaving Equation II.10 intact but providing a pressure loss between the wellbore pressure and the fluid pressure at the first point within the hydraulic fracture. The system is closed,

then, with one equation from the constraint that the sum of fluid injected to all entry points must equal the total injection rate Q_o, that is

$$\sum_{i=1}^{N} Q_i(t) = Q_o \tag{II.11}$$

These form a complete system for determining $w_i(r, t)$, $p_{f(i)}(r,t)$, $R_i(t)$, $\sigma_{I(i)}(r,t)$, and $Q_i(t)$. The problem, then, consists of finding these unknowns as a function of given quantities Q_o, μ', K', E' ,R_w, N, h_k, and t, where $\mu'=12\,\mu$, for dynamic viscosity μ, all other quantities are as previously defined, starting from known values of these quantities at an initial time t_0.

E. Approximation

1. Interaction Stress Approximation

The main challenge and interest of the problem is due to HF interaction. In general, the interaction stresses need to be computed based on the details of the pressure distribution inside each HF (as in e.g. Peirce and Bunger (2015)). However, such an approach is not compatible with the desire for rapid, approximate computation. So, for this model, we propose an approximation of the interaction stress using the uniformly-pressurized crack solution of Sneddon (1946), whereby the normal component of stress performed by neighboring crack *j* on crack *i* is determined as

$$\sigma_{j.i} = \frac{2P_j}{\pi}\left\{\delta_{j,i}{}^{-\frac{1}{2}}cos\frac{1}{2}\varphi_{j,i} - tan^{-1}\frac{\delta_{j,i}{}^{\frac{1}{2}}sin\frac{1}{2}\varphi_{j,i} + \tau_{j,i}sin\theta_{j,i}}{\delta_{j,i}{}^{\frac{1}{2}}cos\frac{1}{2}\varphi_{j,i} + \tau_{j,i}cos\theta_{j,i}}\right.$$
$$\left. + \zeta_{j,i}\delta_{j,i}{}^{-\frac{3}{2}}cos\left(\frac{3}{2}\varphi_{j,i} - \theta_{j,i}\right) - \zeta_{j,i}\delta_{j,i}{}^{-\frac{1}{2}}sin\frac{1}{2}\varphi_{j,i}\right\} \quad \text{(II.12)}$$

where

$$\tau_{j,i} = \left(1 + \zeta_{j,i}^2\right)^{\frac{1}{2}} \quad \delta_{j,i} = \left\{\left[\left(\rho_i\frac{R_i}{R_j}\right)^2 + \zeta_{j,i}^2 - 1\right]^2 + 4\zeta_{j,i}^2\right\}^{\frac{1}{2}}$$
$$\theta_{j,i} = arctan\left(\frac{1}{\zeta_{j,i}}\right) \quad \varphi_{j,i} = arccot\left\{\left[\left(\rho_i\frac{R_i}{R_j}\right)^2 + \zeta_{j,i}^2 - 1\right]/2\zeta_{j,i}\right\} \quad \text{(II.13)}$$

Recall that $\zeta_{j,i}$ is the ratio of spacing $h_{j,i}$ (between fracture i and j) to the crack radius R_j, and recalling that ρ_i is the ratio of radial position r to fracture radius R_i, $\rho_i = \frac{r}{R_i}$. Note that the $\zeta_{j,i}$ value decreases as the fracture grows, that is, as R_i increases for each fracture.

In the solution presented in Equation II.12, P_j is a uniform internal net pressure. The key to the approximation, then, is to choose this internal pressure so as to best approximate the actual interaction stress produced by HFs with non-uniform internal pressure. The approach used here is to select this uniform pressure for each HF at each time step so as to generate a fracture with the same volume as the actual HF being opened by a non-uniform internal pressure. That is, for the j^{th} hydraulic fracture the classical expression for the volume of an ellipsoidal crack resulting from uniform internal pressurization Sneddon (1946) leads directly to

$$P_j = \frac{3}{16}\frac{E'V_j}{R_j{}^3} \quad V_j = \int_0^t Q_j dt \quad \text{(II.14)}$$

The interaction stress model is completed by summation of the interaction stress for each fracture from all neighbors. Hence the interaction stresses exerted on the i^{th} hydraulic fracture is approximated as

$$\sigma_{I(i)} = \sum_{j=1}^{N, j\neq i} \sigma_{j,i}\left[\rho_i R_i / R_j, \zeta_{j,i}, V_j, t, P_j\right] \tag{II.15}$$

where $\sigma_{j,i}$ is given by Eq. (12) and P_j is given by Equation II.14.

2. Approximating Elasticity and Fluid Flow

Elasticity, crack propagation, and fluid flow are strongly coupled through Equation II.3. The non-local integral operator $\mathcal{F}$ and internal traction acting on each fracture are given by

$$\begin{aligned} \mathcal{F}\{\rho_i, T_i(\rho_i, t)\} &= \int_{\rho_i}^{1} \frac{s}{\sqrt{s^2-\rho_i^2}} \int_0^1 \frac{x T_i(xs,t)}{\sqrt{1-x^2}} dx ds \\ T_i(\rho_i, t) &= p_{f(i)}(\rho_i R_i, t) - \sigma_{I(i)}(\rho_i R_i, t) - \sigma_o \end{aligned} \tag{II.16}$$

recalling that where the σ_o is the far field stress, and $\sigma_{I(i)}$ is the interaction stress defined by Equation II.15. Additionally, $\zeta_{j,i}$ is the ratio of spacing $h_{j,i}$ (between fracture i and j) to the crack radius R_j (see Section 3.1), and $p_{f(i)}(r,t)$ is the fluid pressure, a part of the solution. In general, a complete solution is required simultaneously satisfying all of the relevant governing equations. But, the computational intensity of such a solution is the reason why fully coupled models require large computational times. To promote rapid computation, we will approximate this solution. Here we begin by expressing the fluid pressure as

$$p_{f(i)}(r,t) = \left(\frac{\mu' E'^2}{t}\right)^{\frac{1}{3}} \Pi_i(\rho_i, t) + \sigma_o, \quad \rho_i = r/R_i(t)$$

$$\Pi_i(\rho_i, t) \cong A_i(t)\left[\omega - \frac{2}{3(1-\rho_i)^{\frac{1}{3}}}\right] - B\left(ln\frac{\rho_i}{2} + 1\right), \qquad \omega \approx 2.479 \tag{II.17}$$

This form of the pressure is taken based on the solution of Savitski and Detournay (2002) for a viscosity dominated, radially-growing hydraulic fracture in an impermeable rock. When considering the self-similar solution for zero toughness and constant injection rate for an HF propagating in an infinite, homogeneous elastic rock, Savitski and Detournay (2002) shows that $A_i(t) = 0.3581$ and $B = 0.09269$. While this solution only applies for this self-similar limit, we borrow its form for our approximation because it preserves the well-known behavior of the pressure at the tip and inlet of a propagating HF Spence and Sharp (1985), which ought to also be present for interacting hydraulic fractures with non-constant influx rates, that is

$$p_{f(i)} \sim \frac{2}{3}(1-\rho_i)^{-\frac{1}{3}}, 1-\rho_i \ll 1$$

$$p_{f(i)} \sim -\ln \rho_i\,, \rho_i \ll 1 \tag{II.18}$$

The overall premise is that a solution of this form ought to be reasonably compatible with the consequences of coupling between elasticity and fluid flow in the limit where the energy dissipation associated with fluid flow is far greater than the energy dissipation associated with rock breakage (viscosity-dominated regime, see Garagash and Detournay (1999) for a more complete discussion). It remains to choose the coefficients, and we find that a usefully accurate approximation can be obtained (as shown in Section 4) by setting *B=0.09269* and solving for the values of the $A_i(t)$ coefficients that preserve global volume balance for each fracture (Equation II.8). Hence, $A_i(t)$ is a time dependent variable chosen to satisfy

$$2\pi\gamma_i(t)^2 L_i(t)^2 W_i(t) \int_0^1 \Omega_i(\rho_i, A_i(t))\rho d\rho - \int_0^t Q_i(t)dt = 0 \tag{II.19}$$

where the characteristic width

$$W_i(t) = \left(\frac{Q_i(t)\mu'}{2\pi B \left(\frac{\mu' E'^2}{t}\right)^{1/3}} \right)^{1/3} \tag{II.20}$$

represents the near well-bore width derived from Poiseuille law by extracting the leading order behavior of Equation II.4 at inlet to relate the fluid flux to the fluid pressure gradient, where $p_{f(i)} \sim B\ln(r)$ for $r \ll R_i$. Here B is the inlet asymptotic coefficient given by Savitski and Detournay (2002). Note that the dominance of this term near the inlet and the equality of the inlet pressures (Equation II.11) justify setting B equal for all HFs. Similarly, drawing again on the viscosity regime scaling from Savitski and Detournay (2002), the radius is given by

$$R_i(t) = \gamma_i(t) \left(\left(\frac{E't}{\mu'} \right)^{1/3} \int_0^t Q_i(t)dt \right)^{1/3} \tag{II.21}$$

where $\gamma_i(t)$ are unknown values of dimensionless radius for each HF. These are obtained through a requirement that the opening at the HF centers obtained from elasticity, accounting for interaction stress, is compatible for each HF with the width obtained from Equation II.20. To do this, substitution of Equation II.17 in Equation II.3 introduces a dimensionless crack opening $\Omega_i(\rho_i, A_i(t))$ which is determined by $w_i(\rho_i, A_i(t))/\, w_i(0, A_i(t))$ as

$$\Omega_i(\rho_i, A_i(t)) = \mathcal{F}\{\rho_i, T_i(\rho_i, A_i(t))\}/\mathcal{F}\{0, T_i(\rho_i, A_i(t))\} \tag{II.22}$$

with $\mathcal{F}$ denoting the non-local integral as Equation II.3 shown and $T_i(\rho, A_i(t), t)$ is the traction acting across the surfaces of the i^{th} crack given by

$$T_i(\rho_i, A_i(t), t) = \left(\frac{\mu' E'^2}{t}\right)^{\frac{1}{3}} \left\{ A_i(t) \left[\omega - \frac{2}{3(1-\rho_i)^{\frac{1}{3}}} \right] - B\left(ln\frac{\rho_i}{2} + 1 \right) \right\} - \sum_{j=1}^{N, j\neq i} \sigma_{j,i} \left[\rho_i \cdot \frac{R_i(t)}{R_j(t)}, \zeta_{j,i}, t \right] \quad \text{(II.23)}$$

where again we recall that $\sigma_{j,i}$ denotes the interaction stress performed by the neighboring fractures j loading on fracture i (see Section 3.1). The coefficient $A_i(t)$ is still unknown. The strategy, then, is to choose this correspondence between the pressure and opening via Equations II.3 and 17, and in this way we ensure compatibility of the solution with elasticity, as shown by Equation II.24.

We arrive to a system of *2N* equations for the unknown quantities $\gamma_i(t)$ and $A_i(t)$ that impose: 1) satisfying global volume balance for each HF, and 2) requiring the HF opening at the center, computed from elasticity and including the interaction stress, to be compatible with the opening required by Equation II.20. Hence

$$\left\{ \begin{array}{c} 2\pi\gamma_i(t)^2 L_i(t)^2 W_i(t) \int_0^1 \Omega_i\big(\rho_i, A_i(t)\big)\rho_i d\rho_i = \int_0^t Q_i(t)dt \\ \frac{4\gamma_i(t)L_i(t)}{\pi E'} \mathcal{F}\{0, T_i(\rho_i, A_i(t), t)\} = W_i(t) \end{array} \right\} \xrightarrow{yields} \begin{Bmatrix} \gamma_i(t) \\ A_i(t) \end{Bmatrix} \quad \text{(II.24)}$$

3. Motivation for Energy Calculation

It is useful at this point to summarize. The model presented here is constructed so that it first and foremost exactly satisfies global fluid volume balance for each fracture. The solution is also constructed so that the correspondence between the fluid pressure and HF opening exactly satisfies elasticity equation for each fracture, up to a scaling of the elasticity equation by the HF

radius, which is chosen via γ_i to ensure that the elastically-determined width at the inlet is compatible with the influx boundary condition. Hence, we have replaced the need to solve for 3N unknowns (w_i, p_i, R_i) based on 3N equations given by elasticity, propagation, and lubrication (Equations II.3, 6, and 9, respectively) with 2N unknowns (γ_i and A_i) satisfying 2N equations given by Equation II.24. These, of course, depend implicitly upon the calculation of the interaction stress, which we recall proceeds from Equation II.15 using the solution for a uniformly pressurized crack with the same volume as the actual HF.

Besides approximating the interaction stress, the present solution method replaces the propagation conditions $K_I=K_{IC}$ for each HF with a zero-toughness tip asymptote compatible with elasticity and fluid flow and which is implicit in the form of the pressure and opening solutions chosen here (see detailed discussions in Savitski and Detournay (2002); Detournay (2004); Garagash and Detournay (1999)). Hence, the solution henceforth is applicable to only the viscosity-dominated regime of hydraulic fracture propagation. Generalization to finite toughness HFs is a subject of ongoing work.

Importantly, for the present solution method, we must realize that Reynold's lubrication equation is rather harshly approximated by simply ensuring global volume balance and a functional form of the pressure and opening expected to arise at the inlet and tip of the HF. Furthermore, the pressure gradient implied by the lubrication equation is very large near the inlet (Equation II.18). Between these issues, it becomes unreliable to use the distribution of the pressure from Equation II.17 to compute the inlet pressures for the purpose of imposing the equal inlet pressure boundary condition (Equation II.10). We therefore adopt an alternative where the inlet pressure for each HF is computed in order to satisfy a global energy balance. These energetically-computed pressures are then set equal to one another, providing an additional *N-1* equations satisfying pressure

continuity along the wellbore (Equation II.10), noting that at this point additional energy loss due to perforations is readily accounted for (after Cheng et al. (2016)). When combined with the condition that the sum of the influxes equal a constant total wellbore pumping rate (Equation II.11), we obtain in total an additional N equations by which we determine the N unknown values of the fracture influxes, $Q_i(t)$.

4. Balancing Input Power

The expression for the input power is obtained by equating the hydraulic rate of work (product of the pressure and inflow rate) to terms associated with various energy storage, work, and dissipation terms, that is (after Bunger (2013); Lecampion and Detournay (2007))

$$p_{f(i)}(R_w, t)Q_i(t) = \dot{U}_\iota - \dot{W_{o(\iota)}} - \dot{W_{I(\iota)}} + D_{c(i)} + D_{f(i)} \tag{II.25}$$

where:

- U is a portion that goes into increasing the strain energy by deforming the rock strain energy – this is the recoverable elastic energy.
- W_o is the work done on the crack by the in-situ stress – the hydraulic input power must be sufficient to overcome this negative work.
- W_I is the work done on each HF by the compressive stresses induced by its neighbors – again the hydraulic input power must be sufficient to overcome this negative work.
- D_c is the dissipation rate associated with rock breakage.
- D_f is the dissipation rate associated with viscous fluid flow.

Note that, consistent with the present limitation to the viscosity regime, without further loss of generality we can assume $D_c \ll D_f$, and hence D_c is neglected. The remaining terms can be defined following from basic continuum mechanics definitions. Here we make use of the form already derived by Cheng and Bunger (2016) whereby

$$\dot{U}_\iota = \pi \int_{R_w}^{R_i} \left(T_i \frac{\partial w_i}{\partial t} + w_i \frac{\partial T_i}{\partial t} \right) r dr \tag{II.26}$$

$$\dot{W_{o(\iota)}} = -Q_i \sigma_o \tag{II.27}$$

$$\dot{W_{I(\iota)}} = -2\pi \left(\int_{R_w}^{\min(R_i R_j)} \sigma_{I(i)} \frac{\partial w_j}{\partial t} r dr + \sigma_{I(i)} \frac{dR_i}{dt} R_i w_j \left(\frac{R_i}{R_j}\right) \right) \tag{II.28}$$

$$D_{f(i)} = \frac{\pi}{\mu'} \int_{R_w}^{R_i} {w_i}^3 \left(\frac{\partial p_{f(i)}}{\partial r} \right)^2 r dr \tag{II.29}$$

Upon substitution unknowns A_i and γ_i with explicit dependence upon the unknown Q_i via the expression for W_o and with implicit dependence on Q_i via the solutions pressure, width, and radius expressions. Additionally, in order to rapidly estimate the time derivatives, they are approximated over a single time step according to the power law growth of width, length, and pressure given by the single fracture solution of Savitski and Detournay (2002). As such, the dimensionless width, length and pressure rate is set to be consistent with power law growth of 1/9, 4/9 and 1/3 powers, respectively. Bringing all of this together we obtain

$$\dot{U}_\iota = \sum_{j=1}^{N, j \neq i} \pi \gamma_i(t)^2 \left(-\frac{2}{9} \right) \left(\frac{\mu' {E'}^2 \langle Q_i(t) \rangle^3}{t} \right)^{\frac{1}{3}} \int_0^1 \Omega_i\big(\rho_i, A_i(t)\big) \Pi_{net(i)}\big(\rho_i, A_i(t)\big) \rho d\rho \tag{II.30}$$

$$\dot{W_{I(i)}} = -\sum_{j=1}^{N,j\neq i}\left\{\begin{array}{c}\pi min\{R_i,R_j\}\\ \int_0^{min\left\{\frac{R_i}{R_j},1\right\}}\sigma_{I(i)}\left(\rho_i\frac{R_i}{R_j},t\right)\frac{dw_j}{dt}\rho_j d\rho_j\\ +2\pi\left(\frac{\langle Q_j(t)\rangle\mu'}{2\pi B\left(\frac{\mu' E'^2}{t}\right)^{1/3}}\right)^{1/3} R_i\frac{dR_i}{dt}\sigma_{I(i)}(1,t)\Omega_j\left(\frac{R_i}{R_j},A_j(t)\right)\end{array}\right\} \quad \text{(II.31)}$$

$$\dot{D_{f,p(i)}} = \pi\left(\frac{\langle Q_i(t)\rangle^3 E'^2\mu'}{2\pi Bt}\right)^{\frac{1}{3}}\int_0^1 \Omega_i\big(\rho_i,A_i(t)\big)^3\left[\left(\frac{\partial\Pi_{f(i)}\big(\rho_i,A_i(t)\big)}{\partial\rho_i}\right)^2 - \left(\frac{B}{\rho_i}\right)^2\right]\rho_i d\rho_i \quad \text{(II.32)}$$

$$\dot{D_{f,\ln(i)}} = \pi\left(\frac{\langle Q_i(t)\rangle^3 E'^2\mu'}{2\pi Bt}\right)^{\frac{1}{3}}\int_0^1 \Omega_i\big(0,A_i(t)\big)^3\left(\frac{B}{\rho_i}\right)^2\rho_i d\rho_i \quad \text{(II.33)}$$

where R is given by Equation II.21.

5. Summary and Implementation

The final version of the minimalist simulator satisfies:

- Volume balance globally.
- Poiseuille flow via an approximation that preserves the appropriate behavior of the pressure near the tip and inlet, i.e. where most of the viscous dissipation takes place.
- The interaction stress based on the solution for a uniformly pressurized crack with the same radius and volume.
- The width-pressure elasticity relationship exactly.
- Propagation exactly, limiting consideration to vanishingly small fracture toughness.

- The condition of equal inlet pressures exactly, with the wellbore approximated for each HF so as to be compatible with each HF's global energy balance.
- The condition that the fracture influxes sum to the total injection rate exactly.

Such an approach allows an ROM entailing solution of 3*N* equations for 3N unknowns, with simple functional relationships connecting all other quantities. In contrast, to solve the original problem using a fully meshed simulator, even a boundary element-type (BEM) simulator, would require solving for 2*N* unknowns corresponding the HF lengths and influxes plus an additional $4NM^2$ for the nodal values of the pressure, width, flux, and interaction stress on an *MxM* mesh for each HF in the array. If the mesh consists of 10-1000 elements in each direction, the ROM represents a reduction in degrees of freedom on the order of 10^1-10^6 compared to a large-scale model. Indeed this will be shown to be on the order of the factor by which the computational times differ between the ROM and benchmark simulations. The algorithm used by C3Frac to implement this approach is as follows:

1) User inputs: Set values for the physical parameters $\{E, \nu, K_{IC}, \mu, Q, Z, \sigma_{min}, R_w, h_{i,j}\}$as well as the initial time, final time, and time step for the calculation, $\{t_0; t_f; \Delta t\}$, respectively.

2) Pre-guessed state: Set $Q_i^{(k);1} = Q_i^{(k-1)}$. Then fluid pressure $p_{f(i)}^{(k);1}$, length $R_i^{(k);1}$, width $w_i^{(k);1}$ of each HF (i = 1,…, N) is predicated according to Equations II.17, 20 and 21.

$$w_i^{(k);1}(\rho) = \left(\frac{\mu'^2\left[Q_i(t^{(k)})^{(k);1}\right]^3 t^{(k)}}{E'^2}\right)^{1/9} \Omega_i(\rho_i, A_i(t)^{(k);1})^{(k);1}$$

$$R_i^{(k);1} = \left(\left(\frac{E' t^{(k)}}{\mu'}\right)^{\frac{1}{3}} Q_i(t^{(k)})^{(k);1} t^{(k)}\right)^{\frac{1}{3}} \gamma_i^{(k);1}$$

$$P_i^{(k);1}(\rho) = \left(\frac{\mu' E'^2}{t^{(k)}}\right)^{1/3} \Pi_{net(i)}\left(\rho_i, A_i(t)\right)^{(k);1}$$

For the first-time step, the dimensionless parameters for a viscosity-dominated HF are presented by Savitski and Detournay (2002) with small adjustments to the coefficients demonstrated by Cheng and Bunger (2016). The interaction stress is estimated as Equation II.15:

$$\sigma_{I(i)}{}^{(k);1} = \sum_{j=1}^{N,j\neq i} \sigma_{j,i}{}^{(k);1}\left[\rho_i \gamma_i^{(k)} R_i{}^{(k);1}/R_j{}^{(k);1}, \frac{h_{j,i}}{R_j{}^{(k);1}}\right]$$

3) Then the $A_i^{(k);1}$ and $\gamma_i^{(k);1}$ are solved by the system Equation II.24:

$$\begin{Bmatrix} 2\pi\left(\gamma_i^{(k);1} L_i\left(t^{(k)}\right)^{(k);1}\right)^2 W_i\left(t^{(k)}\right)^{(k);1} \int_0^1 \Omega_i(\rho_i, A_i(t)^{(k);1})^{(k);1} \rho_i d\rho_i \\ -\int_0^{t^{(k)}} Q_i\left(t^{(k)}\right)^{(k);1} dt = 0\,, \qquad i = 1, \dots, N \\ \frac{4\gamma_i^{(k);1} L_i\left(t^{(k)}\right)^{(k);1}}{\pi E'} \mathcal{F}\{0, T_i(\rho_i, A_i(t)^{(k);1}, t^{(k)})\} \\ -W_i\left(t^{(k)}\right)^{(k);1} = 0, \qquad i = 1, \dots, N \end{Bmatrix}$$

4) To obtain the solution, the system of equations is solved numerically using Newton's method. Based on the above calculated value, the stress strain coupled local crack opening, net pressure and radius is numerically evaluated. We then substitute the stress coupled $\Omega_i^{(k);1}$,$\gamma_i^{(k);1}$ into the power balance function. Use non-linear solver (e.g. Matlab "fsolve") to obtain the N influxes $Q_i^{(k);2}$ simultaneously satisfying the constraints that the pressure at the inlet of all of the fractures is the same (i.e. connected by a horizontal wellbore with negligible friction loss along the wellbore between the entry points) and a further constraint that the sum of all influxes to the fractures must equal the total influx to the well. That is,

$$p_{f(1)}{}^{(k)}(R_w) = p_{f(2)}{}^{(k)}(R_w) = \cdots = p_{f(N)}{}^{(k)}(R_w), \qquad \sum_{i=1}^{N} Q_i{}^{(k)} = Q_o$$

Here a critical point is that the pressures are estimated using the energy balance equation via Equation II.25. Upon substitution of the estimates for the power terms Equations II.20, 21 and 30-33 this estimate is

$$p_{f(i)}^{(k);n}(R_w) = \sigma_o + \ldots.$$

$$\frac{1}{Q_i^{(k);n}}\left[\begin{array}{l} -\frac{2}{9}\left(\frac{E'^2\left(Q_i^{(k);n}\right)^3\mu'}{t^{(k)}}\right)^{1/3}\int_0^1 \Pi_{net(i)}^{(k);n}\Omega_i^{(k);n}\rho_i d\rho_i - \ldots \\ 2\pi\left\{\begin{array}{l}\left(\frac{1}{9}\right)\sum_{j=1}^{N,j\neq i}\left\{\begin{array}{l}\frac{w_j^{(k);n}}{t^{(k)}}\left[\min\left(R_i^{(k);n},R_j^{(k);n}\right)\right]^2 * \ldots.. \\ \int_0^{\min\left(R_i^{(k);n}/R_j^{(k);n},1\right)}\sigma_I\left(\rho_i\frac{R_i^{(k);n}}{R_j^{(k);n}},\zeta_{j,i}^{(k);n}\right)\Omega_j^{(k);n}\rho_j d\rho_j\end{array}\right\}+\ldots \\ \left(\frac{4}{9}\right)\frac{\left(R_i^{(k);n}\right)^2}{t^{(k)}}\sum_{j=1}^{N,j\neq i} w_j^{(k);n}\Omega_j^{(k);n}\left(R_i^{(k);n}/R_j^{(k);n}\right)\sigma_I\left(1,\zeta_{j,i}^{(k);n}\right)\end{array}\right\}+\ldots \\ 0.04637\left(\frac{E'^2\mu'\left(Q_i^{(k);n}\right)^3}{t^{(k)}}\right)^{1/3}\ln\left(\frac{R_w^9\mu'}{E'\left(Q_i^{(k);n}\right)^3\left(t^{(k)}\right)^4}\right)^{1/9}+\ldots \\ \left(\frac{E'^2\mu'\left(Q_i^{(k);n}\right)^3}{t^{(k)}}\right)^{1/3}\int_0^1\left(\Omega_i^{(k);n}\right)^3\left(\left(\frac{\partial\Pi_{f(i)}^{(k);n}}{\partial\rho_i}\right)^2-\frac{B^2}{\rho_i^2}\right)\rho_i d\rho_i \end{array}\right]$$

Note the simplicity of the modification, illustrating the potential to include other mechanisms (e.g. fluid leakoff, perforation loss and previous stage effect) in a straightforward manner provided their contribution to the global energy balance can be computed.

5) Check the relative difference between initially guessed $Q_i^{(k);1}$ and returned $Q_i^{(k);2}$. If the value is below a given tolerance that is

$$\left[Q_i^{(k);N} - Q_i^{(k);N-1}\right]/Q_i^{(k);N-1} < TOL$$

then output the $Q_i^{(k);2}$ as the final result. If not, iterate to convergence.

6) Repeat steps (2)-(5) until $t^{(k)} = t$.

Note that the new C3Frac bears a few similarities to the previously-published C2Frac Cheng and Bunger (2016). Similarities include they both solve the flow rate based on the power balance with Newtonian numerical method. However, the striking and important difference lies in the solution of width, radius and pressure, which is solved by using an asymptotic solution (after Savitski and Detournay (2002)) in C2Frac. In contrast, C3Frac uses Equation II.24 to obtain the non-self-similar solution caused by the inconstant flow rate with interaction stress included. The result is that C3Frac and C2Frac give very similar predictions when the fracture radii are less than the fracture spacing, and they diverge as the fractures continue their growth such that the courser approximation of the interaction stress and elasticity equation used in C2Frac becomes less accurate.

F. Validating And Overall Behavior Of The Solution

We validate and illustrate the use of the model considering cases with 5 HFs. The fractures are placed symmetrically relative to the middle fracture. Hence the "outer" fractures, 1 and 5, are identical. So also the "inner" fractures, 2 and 4, are identical. Fracture 3 always occupies the center of the array and will henceforth be called the "middle" fracture. The validating is comprised of comparison of the C3Frac approximations (ROM) to fully coupled large-scale ("high fidelity") simulations obtained using ILSA II (after Peirce and Bunger (2015), using similar validating cases to Cheng and Bunger (2016)). ILSA II is extended for multiple, parallel planar hydraulic fractures Peirce and Bunger (2015) based on the Implicit Level Set Algorithm ("ILSA") Peirce and Detournay (2008) ILSA by accounting for full 3D elastic coupling between the simultaneously propagating fractures. The Implicit Level Set Algorithm ("ILSA") is a fully coupled simulator for

3D hydraulic fractures under the constraint that fracture growth is confined to a pre-defined plane. It's utility is similar to other planar3D hydraulic fracture simulators (see review of Lecampion et al. (2018)), with the key novelty of enabling accurate solutions on very coarse meshes by embedding an appropriate tip asymptotic behavior and then computing the moving boundary condition of the advancing crack tip through an implicit time stepping method that projects the front location based on these known asymptotics. Like several other planar 3D hydraulic fracture simulators, the elasticity equation is solved using a 3D displacement discontinuity method and fluid flow is solved using the Finite Volume method. The following parameter set is used for both the C3Frac and ILSA II simulations:

E=9.5 GPa, ν=0.2, K_{IC}=0 MPa·m$^{1/2}$,

μ=1 Pa·s, $\underline{Q}_o$=0.1 m^3/s, Z=20 m,

σ_o =70 Mpa, R_w=0.2m.

For each case, we present comparisons of the time evolution of fracture radius, fluid influx to each fracture, fracture opening at the center, and total fracture area. We also present three-dimensional plots showing the radius of each HF with color scale corresponding to the HF width. Figures II.3 and 4 show results from a case where the HFs are uniformly spaced so that h_1 = 5 m and hence fracture planes have z coordinates (in meters) z_1=0, z_2=5, z_3=10, z_4=15, and z_5=20. Figures II.5 and 6 show results corresponding to a non-uniformly spaced array in which fractures 2 and 4 are moved so that h_1=3.6 m, corresponding to fracture planes having z coordinates (in meters) z_1=0, z_2=3.6, z_3=10, z_4=16.4, and z_5=20. These results presented include: The dimensionless radius $R_i(t)/Z$, the inflow rate $q_i(R_w, t)$, the crack aperture at inlet $w_i(R_w, t)$ and total fracture area defined as

$$A(t) = \sum_{i=1}^{N-1} {R_i}^2(t)\,\pi \tag{II.34}$$

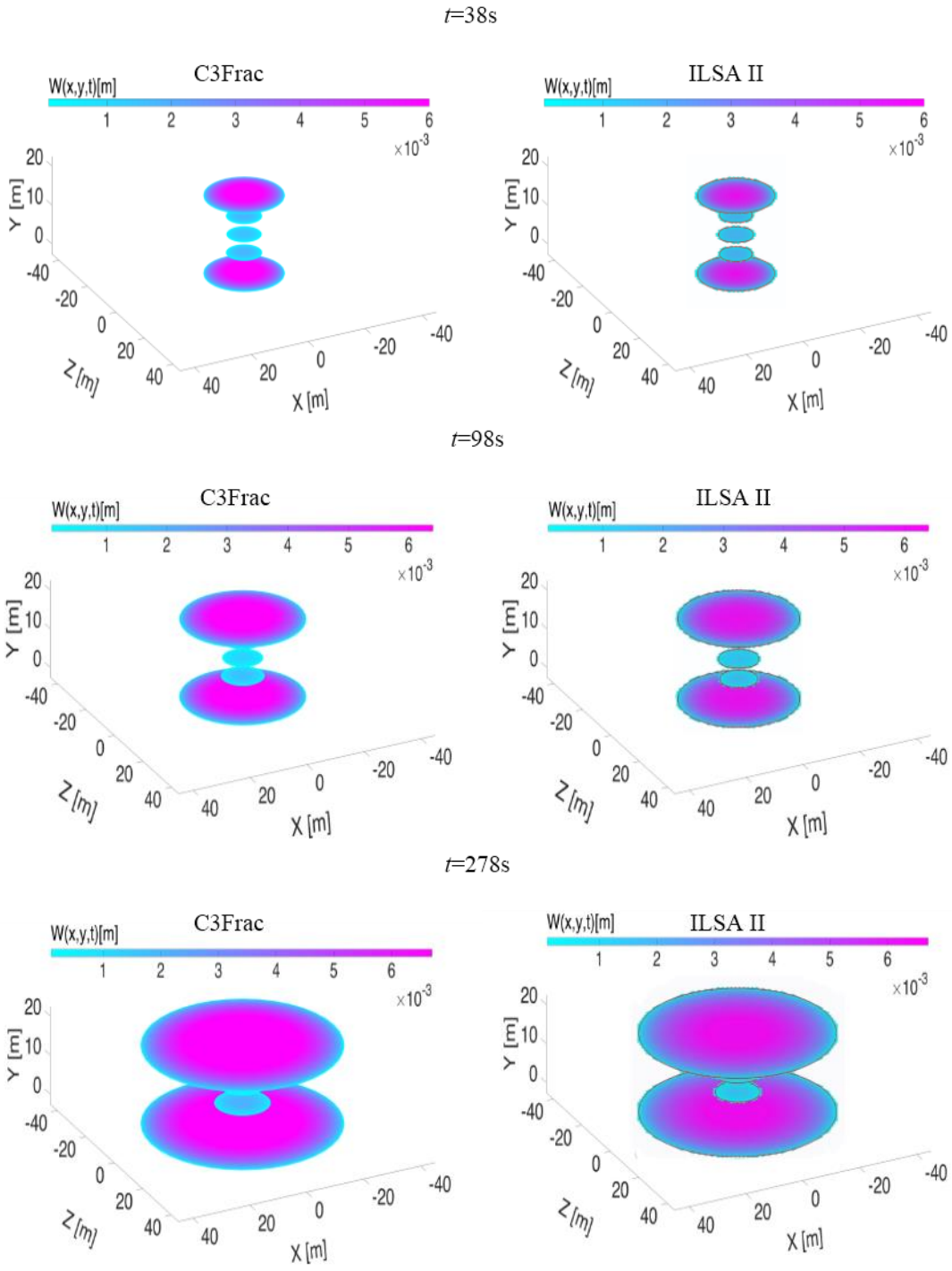

Figure II.3: Evolution for uniform spacing $h_1 = h_2 = h_3 = h_4$=5m, showing results from both C3Frac (ROM) and ILSA II (large scale).

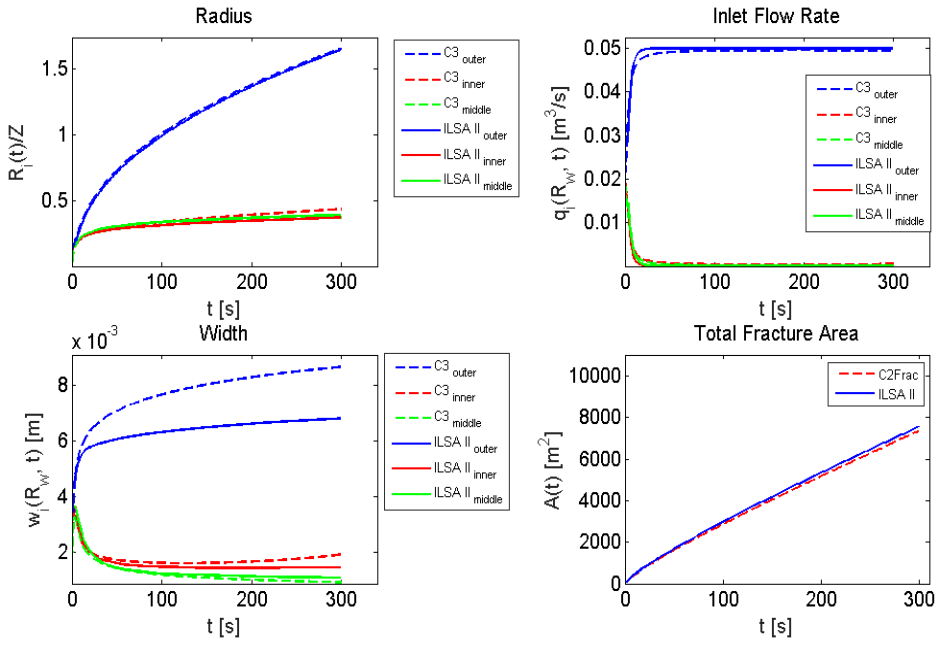

Figure II.4: C3Frac compared with ILSA II for a uniform array with $h_1 = h_2 = h_3 = h_4 = 5$m.

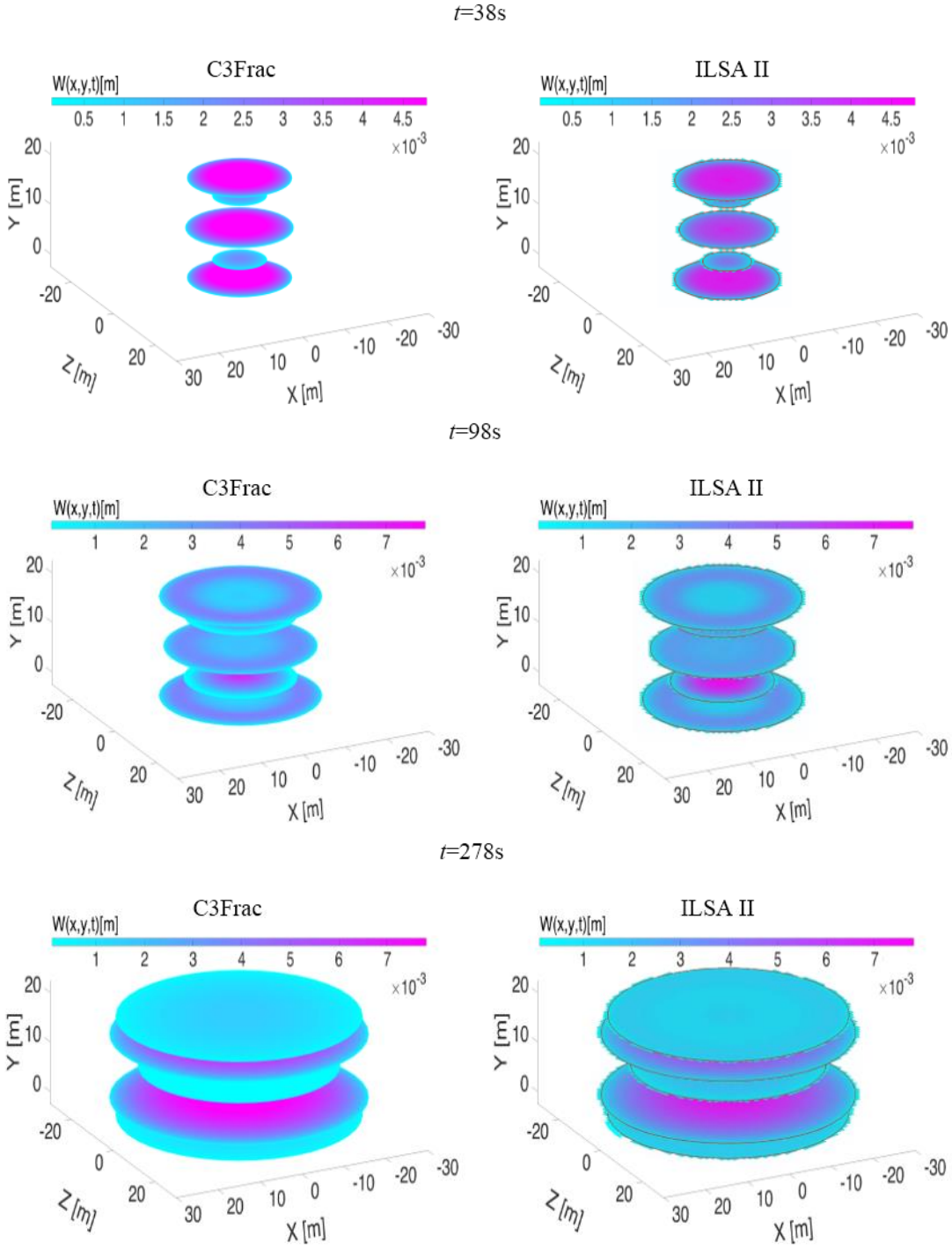

Figure II.5: Evolution for non-uniform spacing $h_1 = h_4 = 3.6$m and $h_2 = h_3 = 6.4$m.

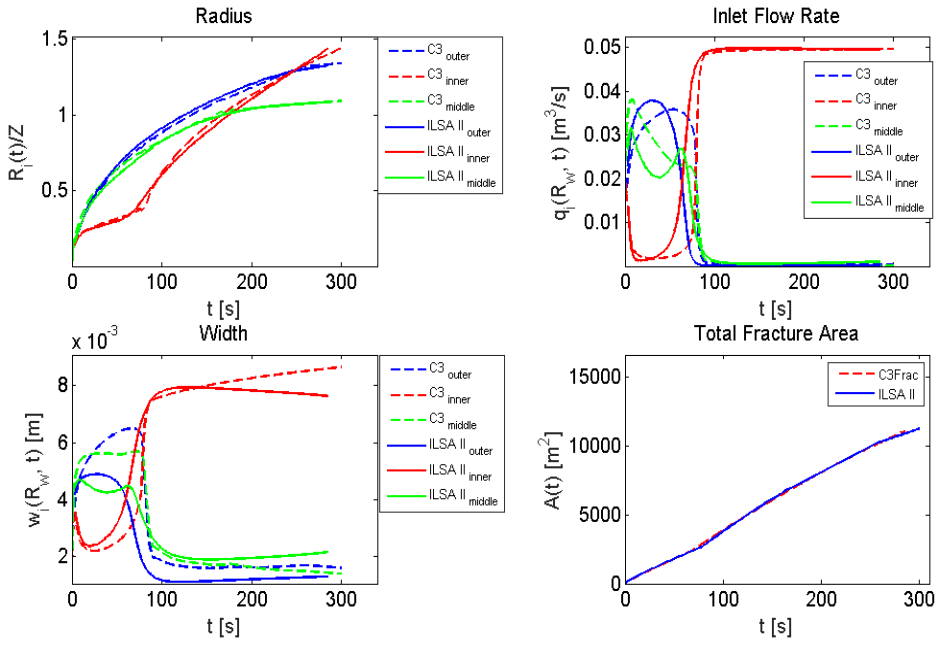

Figure II.6: C3Frac compared with ILSA II for non-uniform array with $h_1 = h_4 = 3.6$m and $h_2 = h_3 = 6.4$m.

Overall the ability of C3Frac to approximate the fracture radius and area is very good. The inlet flux is also adequately approximated, with several observations that can be made. Firstly, we observe the stress-shadowing phenomenon in which outer fractures grow preferentially while growth of the inner fractures is stunted. This phenomenon has also been observed by many others (e.g. Fisher et al. (2004); Abass et al. (2009); Meyer and Bazan (2011); Germanovich et al. (1997)), and is strongly evidenced in the uniform spacing case (Figure II.4), where the inflow to the outer fracture increases sharply to 0.05m^3/s and consumes nearly all the total injection rate after 20 seconds. The localization of growth in the outer fractures is understandable because they have no constraint on their growth from outside the array. At the same time, flow rate to the other fractures decreases to approach zero. This is understood because the interior fractures have to compete with

one another in an induced compressive stress field that is established by the outer fractures and enhanced by any additional growth by the interior fractures. The localization to the outer fractures becomes more pronounced with time while growth of the inner fractures is minimal for uniform spacing (h_1=5m) case (Figure II.3)

Upon changing the spacing h_1 from 5m to 3.6m, the induced stresses from the inner fractures on the middle fracture decrease as the spacing between the inner and middle increases. Under this spacing, the inlet flow rate to the outer fractures consumes less of the total influx to the wellbore and the middle fracture's flow rate is only slightly less while the flow rate to the inner fracture remains almost constant with time. A similar behavior was observed by Peirce and Bunger (2015).

Further fracture growth is driven by a somewhat surprising mechanism. Capturing this mechanism is critical to matching the benchmark ILSA II simulations, and this was not possible with the prototype C2Frac model presented by Cheng and Bunger (2016). The present work has focused on better approximating the stress interaction among the fractures especially when the radius exceeds the spacing. The "squeeze out" phenomenon (first observed by Peirce and Bunger (2015)) approximated by this new version C3Frac is described as follows. Due to the relative growth difference among the five fractures, the interaction stress induced from inner fractures obtains a negative value (tensile) near the tip. Combined with the impact of the moving boundary on the time derivative of the energy integral, a decreased interaction stress contribution is formed in the total energy balance for inner fractures via Equation II.28.

In the current example, the dominance of the fractures, 1, 3, and 5 is thus stopped by the reversal of the inner fractures at 50s (see Figure II.6). The fluid that was in these fractures in the region near the wellbore is subsequently displaced toward the perimeter as they are subjected to

the induced stress associated with the now rapidly inflating inner fractures. This outward squeezing of the fluid has the effect of advancing the fracture by the displacing the fluid from the vicinity of the wellbore rather than by influx from the wellbore. A new phase is reached in which the role of the inner fractures switches from being passive and accepting relatively little fluid to accepting the majority of the fluid and actively driving the dynamics of the fracture development throughout the array. The increased uptake of fluid in the inner fractures also has a suppressing effect on outer fractures. As a side effect, the middle fracture gets a chance to take in more fluid from the wellbore, which is also depicted by a small rise (Figure II.6) shortly after t_s. At t=80s, the suppression effect from inner fractures also starts to affect middle fracture, and ultimately chokes further uptake of fluid into fractures 1, 3, and 5. Note that for the uniform spacing, the inner fractures never switch from being stunted to being dominant because they do not grow sufficiently to be impacted by the negative stress induced by the ratio *h/R*.

Besides the very good agreement between C3Frac and ILSA II, the C3Frac results also indicate the temporal and spatial character of crack opening (Figure II.6 and Figure II.4) in which the penny-shaped geometry is valid until the extension of the fracture becomes of the order of the stage length. As time goes on, a compressed region, approaching closure ($w_i(\rho_i, t) \cong 0$), appears owing to the interaction stress performed by inner fractures during the reversal process (Figure II.6).

Since the total fractured area can be related to the potential recovery of hydrocarbons (e.g.[4]), total fractured area is an important metric of hydraulic fracturing effectiveness (e.g. Peirce and Bunger (2015)). Here we define $A_{total}(t)$, which is the summation of surface area $A_i(t)$ over all the fractures, where $A_i(t) = \pi R_i(t)^2$. When all the fractures are small, so that their mutual stress interactions are insignificant, all configurations generate surface area at roughly the same

rate and almost linearly with the time. However, for $t > 50$ s, because of the ever-increasing interaction effects, the h_1=3.6m case (12,000 m^2, Figure II.6) generates more area than the uniform cases (7,500 m^2, Figure II.4). Note that the same total volume is injected over the same time of pumping for these two cases. The reason for larger surface area in the non-uniform spacing case is a beneficial effect of the reversal fractures, causing dominance of fractures 2 and 4 in the latter part of the injection and an overall more uniform distribution of total volume among the 5 fractures. Hence these results show the total fractured area can be increased by more than 60% by selecting configurations for which h_1=3.6 m, as result consistent with Peirce and Bunger (2015).

Furthermore, non-uniform four and six fractures are also employed to test the validation between C3Frac and ILSA II. Figure II.7 shows results from a four-fracture case where the HFs are non-uniformly spaced so that h_1 = 5 m and hence fracture planes have z coordinates (in meters) z_1=0, z_2=5, z_3=15, and z_5=20. Figure II.8 shows results for a non-uniformly spaced six-fracture array in which fractures 2, 3, 4 and 5 are moved so that h_1=2.75 m, h_2=4.25 m, corresponding to fracture planes having z coordinates (in meters) z_1=0, z_2=2.75, z_3=7, z_4=13, z_5=17.25 and z_5=20. The level of agreement between the ROM of C3Frac and the large scale model of ILSA II is similar to what was obtained for five fracture cases. We also note that the aforementioned “squeeze-out” is observed in the six fracture case but not in the four fracture case presented here, although further numerical experimentation may lead to discovery of squeeze-out in certain non-uniform four fracture cases as well.

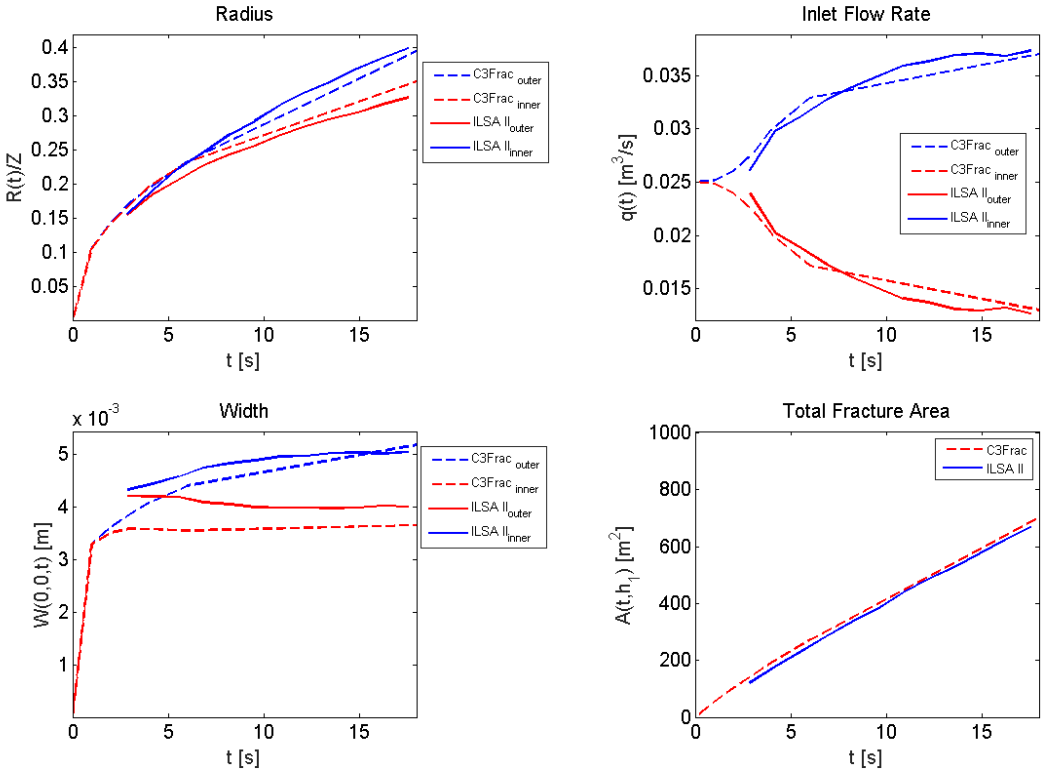

Figure II.7: C3Frac compared with ILSA II for a non-uniform four fracture array with $h_1 = h_3 = 4$m, $h_2 = 12$m.

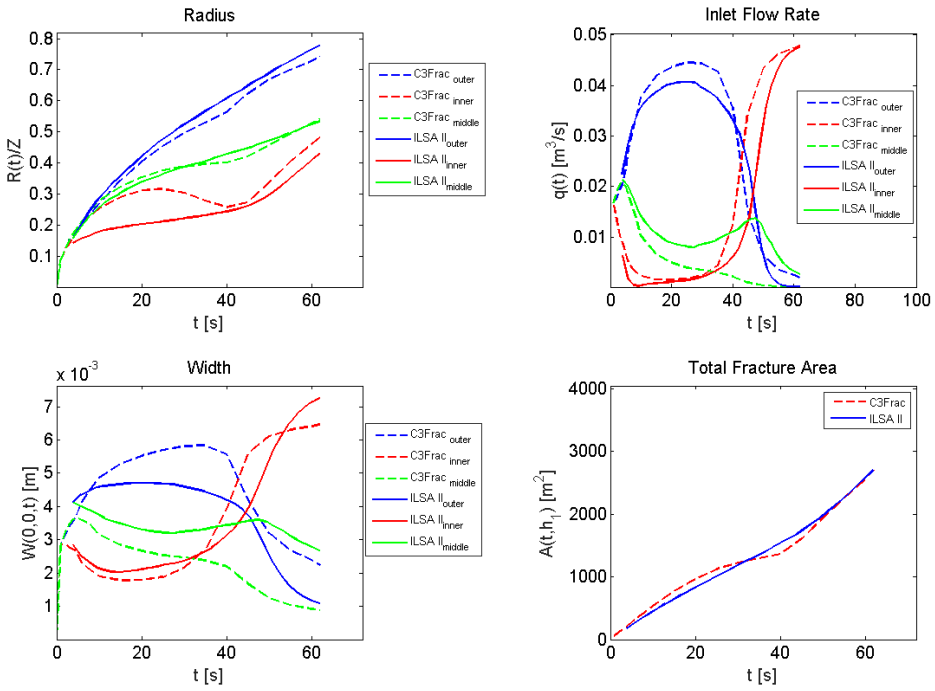

Figure II.8: C3Frac compared with ILSA II for non-uniform six fracture array with $h_1 = h_5 = 2.75$m, $h_2 = h_4 = 4.25$m and $h_3 = 6$m.

So far we have discussed the overall behavior of the system illustrated both by C3Frac and the ILSA II benchmarks. But most importantly, Figures II.3-8 show the similarity between C3Frac and ILSA II. Typically, C3Frac remains within 2% relative to the ILSA II benchmark for fracture area. The worst match is in the fracture opening at the wellbore, which is in about 10% discrepancy for the inner fracture and as much as 50% for the outer and middle fractures. Note that in the far field (short HF) previous version C2Frac Cheng and Bunger (2016), simulates the radial growth only in the range that R_{max}/Z is smaller than 0.6. Through the substantially modified solution method algorithm, the approximation to the benchmark ILSA II is achieved even after the fracture radii exceed the total stage length.

Table II.1: Computation time compare between C2Frac, C3Frac and ILSA II for uniform fracture array at same simulation time and steps.

Uniform Five	C2Frac	C3Frac	ILSA II
Computation time	1.06s	255 s	220612 s
Simulation time & Steps	t=203 s 128 steps	t=203 s 128 steps	t=203 s 128 steps
Processer & RAM	INTEL-i7 4770k 4.00 GHz. 32 GB RAM	INTEL-i7 4770k 4.00 GHz. 32 GB RAM	INTEL-XEON E5649 2.53 GHz 96 GB RAM

While achieving the previously-demonstrated accuracy, the simulator takes only minutes to compute a single multi-fracture result at typical reservoir length and time scales on a personal computer. Although this is much slower than C2Frac, which computes in a few seconds, the benefit is the ability to simulate even when the fractures are long relative to their separation. To this point, an illustration of computation time for C2Frac, C3Frac, and ILSA II is presented in Table II.1. Note, however, that the computation time of ILSA II for each time step continuously increases because the advancing front leads to an ever-increasing number of elements in the simulation, there is no such increase in computation time per model time step in C2Frac or C3Frac. We also note that there is a possibility to significantly speed up the simulations by combining C2Frac and C3Frac, where the former is used to simulate growth until the maximum fracture length reaches

some threshold (say, around half of the stage length), after which C3Frac is used to compute the rest of the growth, For example, in h_1=3.6m case, before the squeeze out effect occurs (the point in time where the C3Frac enhancement become most important), the fracture growth can be well-approximated by C2Frac in seconds, which in this case would save 3 minutes of computation time over using C3Frac only. Either way, the simulations are much faster than fully coupled simulations, which can take tens of hours and up to a week to compute on a similar computer. Because of the speed of calculation and reasonable accuracy, this new approximate simulator opens new possibilities to explore large parametric spaces, identifying combinations of parameters associated with optimal behaviors (i.e. maximizing fracture surface area) and enabling time consuming but accurate fully-coupled simulations to be focused on these regions of interest in the parametric space that governs the behavior of the system.

G. Parametric Study

A few examples illustrate the optimization enabled by the rapid computation times associated with C3Frac. The metric by which we evaluate the performance of a given configuration is taken as the total surface area of all the fractures in the array until time t, which we represent by $A(t; h_1)$. It is useful to normalize by $A^*(T)$, the total fracture area of N non-interacting fractures each taking the same total volume of fluid and growing exactly uniformly according to the relevant analytical solution Savitski and Detournay (2002). The ratio $A(t; h_1)/ A^*(T)$ represents the relative change in the total fractured area that is achieved by adjusting h_1. We plot $A(T; h_1)/ A^*(T)$ as a function of the dimensionless configuration parameter $h_1(N\text{-}1)/Z$, with various stage lengths Z and injection rates Q. These results are presented in Figures II.9 and 10, where we note that the uniform

spacing $h_1=Z/(N-1)$ is represented as 1, while its limiting values of 0 and 2 correspond to non-uniform limiting cases with $h_1=0$ (touching of fractures 1-2 and 4-5) and $h_1= 2*Z/(N-1)$ (touching of fractures 2-3-4), respectively.

First, we illustrate the impact of stage length, keeping all other quantities such as injection rate and time equal, Figure II.9. We compare results for stage length Z = 25m, 50m and 100m. We observe that the uniformly-spaced configuration, coming with a significant stress shadow especially at Z=50 and 100m, corresponds to a lower normalized area around 0.75. By decreasing h_1 below $Z/(N-1)$, that is, by moving the 2nd and 4th fractures away from the center fracture as suggested by Peirce and Bunger (2015), results in 80% to 120% relative increase in the total fractured area. This increase comes for all stage lengths, despite the existence of some important differences. Most notably, a smaller interval ratio $h_1(N-1)/Z$ is required to maximize the generated area for the largest stage length. This is because such a small interval length is needed to stimulate the squeezing effect, which turns out to have an important impact on maximizing the fracture area. Also note that the sensitivity of the total, final area to the spacing (derivative of the plots in Figure II.7) tends to be greater for the larger interval length and at larger injection times, meaning that such spacing optimization is more important when interval lengths and/or injection times are large.

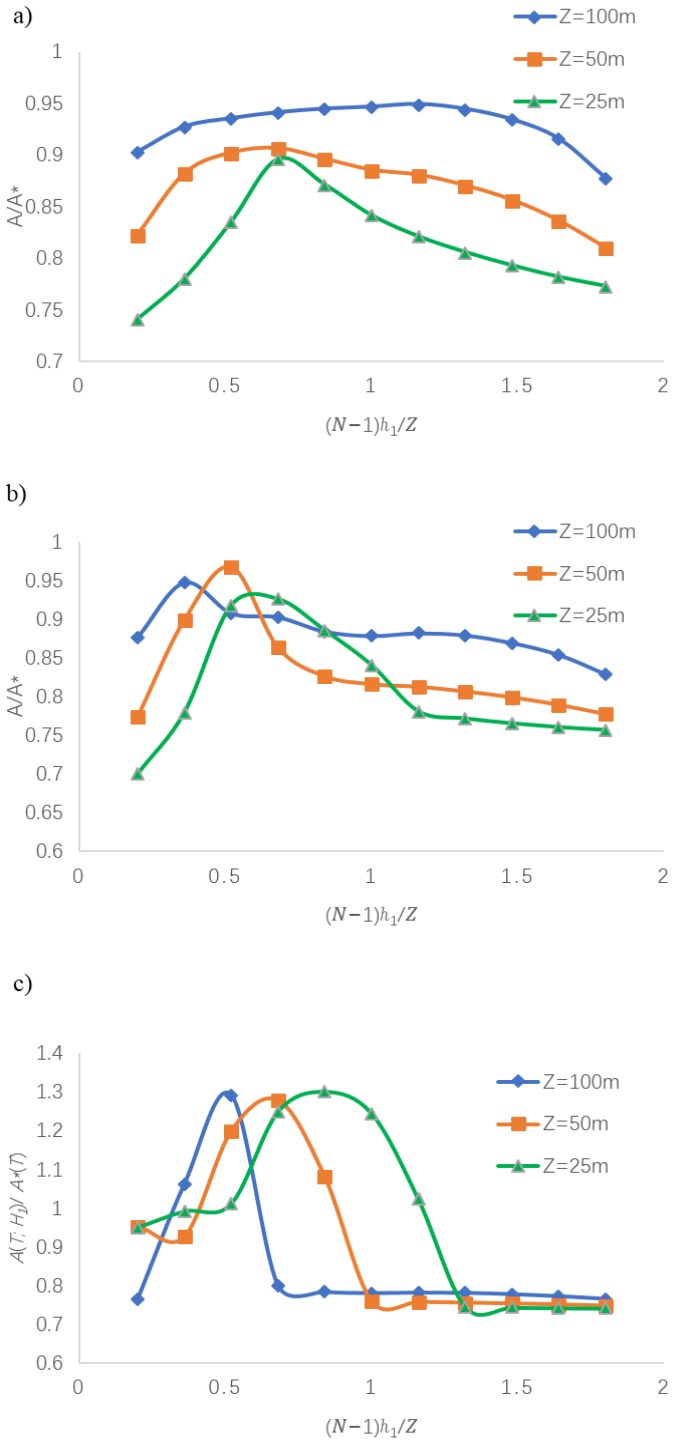

Figure II.9: Normalized dimensionless total fracture area $A(T; h_1)/ A^*(T)$ evolution with various stage length Z in the five-fracture array for different values of the spacing h_1 for Q=0.2 m³/s and t as a) 50 s b) 300 s c)3600 s.

The prior increases in productivity (inferred from the surface area) of uniform spacing stimulations by using smaller stage lengths Figure II.9 come without need for increasing injection rate. To investigate if there is benefit in optimizing in terms of injection rate, we plot the normalized area $A(T;\ h_1)/\ A^*(T)$ versus the configuration perturbation parameter h_1 for a representative selection of values of the injection rate Q_o given by 0.1m^3/s, 0.2m^3/s and 0.3m^3/s, adjusting injected volume to ensure satisfaction of the viscosity regime requirement. The total injection volume is preset as 120 m^3 and 720 m^3 and stage length is 50m.

We observe that the shapes of these curves are very similar, but a little shifted over the range of values of the configuration parameter considered. This is due to fluid flow that follows Poiseuille law, Eq. (4). For the sake of argument, assume we can ignore differences in the pressure gradient between fracture entry points. Then the crack opening near the inlet $w_i(R_w, t)$ is proportional to the inlet flow rate $q_i(t)^{1/3}$. When the injection rate is set to be 0.2 m^3/s, the crack width is 1.26 times larger than in the case where Q_o=0.1 m^3/s. Hence, for the same injected volume, the cases with larger average width (opening) give a smaller fracture area. This relationship is the cause of the observed differences in Figure II.10, where Q_o =0.1 m^3/s leads to about 30% more fractured area than Q_o =0.2 m^3/s. Otherwise, for a given injection rate, the total crack opening is maximized for the spacing that also achieves the maximum area, as illustrated by Figure II.10(a) and Figure II.10(b). The reason is that flow rate becomes the most uniform in its distribution at that spacing. This observation holds for a while, until the fractures become very long relative to their spacing. In this super-near-field region, the fracture opening profile indicates that the opening in the vicinity of the tip increases at the cost of decreasing the opening of the central portion Figure II.5. Thus, the maximum width eventually does not correspond to the spacing that generates the maximum area.

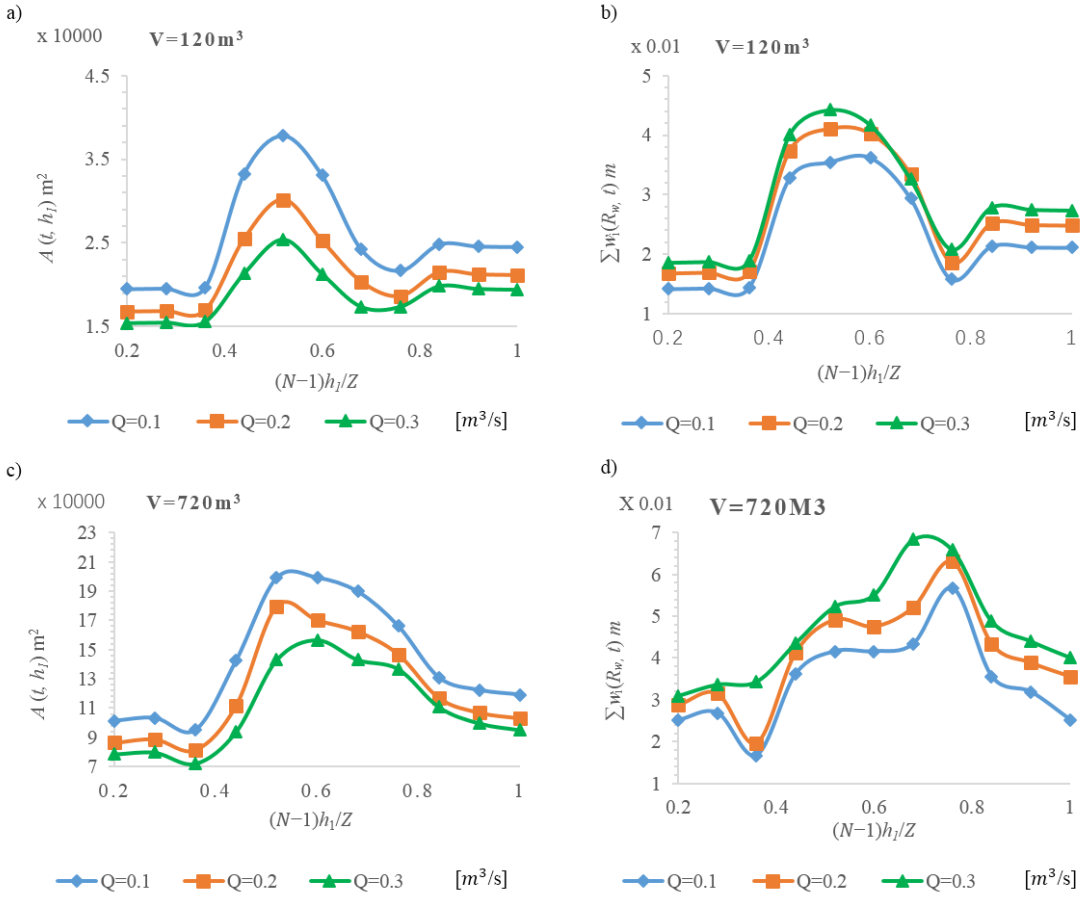

Figure II.10: Illustrative examples of injection rate effect for total fractured area $A(T, h_1)$ and summation of near wellbore width $\sum W(0,T, h_1)$ respectively, in which the HF parameters such as input volume are set as a)120 m^3 b) 120 m^3 c)720 m^3 d) 720 m^3

H. Conclusion

A new approximate ROM simulator, C3Frac, rapidly predicts how mechanical interaction among simultaneously growing radial hydraulic fractures effects their growth. This approximate simulation method is based on preserving global volume and energy balance and the elastically-determined crack opening while approximating the fluid flow via a functional form preserving the pressure gradient near the inlet and tip and approximating the interaction stresses based on the analytical solution for uniformly pressurized cracks with the same length and volume as each hydraulic fracture. Validating through comparison to results from a fully-coupled, large scale planar 3D model (ILSA II) confirm the accuracy of the approximation, especially for prediction of the length of each fracture and the overall created fracture surface area.

The ROM is able to capture complex coupled phenomena. When the spacing between fractures is uniform, the model confirms the phenomenon of stress shadowing in which growth of one or more fractures is suppressed by the stresses generated by their neighbors. However, we have also shown that the model captures a "squeeze out" phenomenon that takes place for certain non-uniform fracture spacing configurations when the fracture radii substantially exceed the spacing. Simulations suggest there is the potential to increase the total fractured area in the array after 3600 seconds of pumping by 100% compared to the uniform array for which the squeeze out effect does not occur and the inner fractures are simply suppressed in their growth.

The ROM simulator computes within a few minutes on a typical personal computer, thereby enabling wide ranging parametric studies and optimization that requires hundreds of model evaluations. As a demonstration of this capability, it is shown that non-uniform spacing is one of several ways to impact the uniformity and total surface area of created fractures. Stage length and

injection rate also provide variable parameters for optimization. From our study, strategic stage length choice is shown to be a complimentary approach. Somewhat counter-intuitively, we show decreasing stage length can actually lead to improvement in the ability to generate fracture surface area with relatively uniform spacing because of the ability of shorter stage lengths to trigger the squeeze out effect. The numerical experiments also indicate that smaller injection rate generates more fracture area for a given injected volume, as expected due to the lower net pressure and resulting fracture opening. As a tradeoff, such a design will decrease the capacity for proppant admittance due to the smaller opening.

In summary, this work provides not only a new method for reduced order modeling of hydraulic fractures, but also, practically, a demonstration that the stress shadow effect can be modified and to some degree mitigated through selectable treating conditions such as fracture spacing, stage length, and injected volume. While beyond the present scope, there is more that can be optimized such as fluid flow rate, fluid viscosity, and so on. Future work will aim at expanding capability for optimizing horizontal well completions. These efforts will firstly be aimed at including the impact of leak off, fracture toughness, and the presence of height growth barriers. Future work will also focus on including proppant transport and developing benchmark laboratory and field experiments.

III. Optimizing Fluid Viscosity For Systems Of Multiple Hydraulic Fractures

A. Preamble

Accounting for fluid leak-off, which is defined as the loss of fluid to the rock formation adjacent to the fractures, is one of the most significant challenges for all hydraulic fracture models. It makes the model history dependent because the leakoff rate depends upon the time at which the fracture reached each location along its path. The challenge is compounded by the need to account for growth of multiple interacting hydraulic fractures. A number of important contributions account for leak off and multiple fracture growth Wong et al. (2013); Kresse et al. (2013); Damjanac and Cundall (2016); Dontsov and Peirce (2017) . However, the time consuming nature of these methods makes them impractical for many simulation runs required by optimization or extensive parametric studies. To avoid inclusion of new variables that could substantial reduce computation speed, a novel concept of "composite viscosity" is introduced to modify the approximate solution to satisfy the volume and energy balance with quantified fluid loss. The simulation results illustrate the effect of leak-off, showing the existence of an optimal viscosity, described in detail in the Part III Cheng (2019b).

B. Abstract

Optimal hydraulic fracturing stimulations of horizontal oil and gas wells maximize created fracture surface area and/or maximize the uniformity of stimulation. Here we use a new, rapidly-computing hydraulic fracture model to investigate how surface area and uniformity are impacted by interplay among multiple growing hydraulic fractures driven through permeable rocks by fluids of various viscosities. The results show the existence of a surface-area-optimizing viscosity that is large enough to control leak-off but not so large that leads to unnecessarily large fracture aperture.

C. Introduction

The problem of hydraulic fracturing is challenging to analyze due to a variety of physical processes that are involved. Hydraulic fracture models include coupling among rock deformation, crack propagation, fluid flow, and fluid leak off Lecampion et al. (2017); Adachi et al. (2007); Mendelsohn (1984). Solving the resulting non-linear, non-local, history-dependent system of equations provides leads to predictions of hydraulic fracture geometry, aperture (width), and fluid pressure Adachi (2001). Predicting these quantities is an important task for accomplishing a variety of engineering objectives including maintaining growth in desired subsurface strata and achieving a desired fracture length Economides and Nolte (2000).

Besides these classical challenges and design goals, development of unconventional oil and gas resources by the creating of many hydraulic fractures along horizontal wells brings additional design goals and accompanying modeling challenges. Here we are motivated by 2 design goals

associated with each so-called fracturing stage, that is, the stimulation of an isolated section of well with the goal of generating hydraulic fractures that grow simultaneously from typically 3-6 perforation clusters that are separated by tens of meters King (2012); Lecampion et al. (2015). These design goals are: 1) Maximizing the fracture surface area created by a given injection volume for each stage; this surface area is often considered to relate directly to eventual production rate Economides and Nolte (2000); Cheng and Bunger (2016), and 2) Maximizing the uniformity of the stimulation in order to prevent unproductive perforation clusters Slocombe et al. (2013); Bunger and Lecampion (2017).

Of the challenges for any hydraulic fracture model, one of the most significant is accounting for leak off, which is defined as the loss of fluid to the rock formation adjacent to the fractures. The challenge is compounded by the need to account for growth of multiple, simultaneously-growing and interacting hydraulic fractures. A number of important contributions account for leak off and multiple fracture growth Wong et al. (2013); Kresse et al. (2013); Damjanac and Cundall (2016); Dontsov and Peirce (2017), however the models remain sufficiently computationally intensive that it is difficult, and often impractical, to carry out extensive parametric studies and/or optimizations that require thousands of model evaluation. In this context, the goal of the present work is to develop a reduced order hydraulic fracture simulator capable of approximating growth of multiple hydraulic fracture in a permeable rock, and to use this simulator to explore treatment parameters, such as fluid viscosity, that optimize fracture surface area and uniformity.

The main difficulty and advance relative to prior work arises from the inclusion of leak-off in the model; previously we developed reduced order hydraulic fracture models valid for impermeable rocks and limited to the so-called “viscosity-dominated” regime wherein far more

energy is dissipated in fluid flow compared with rock fracturing Cheng and Bunger (2016); Cheng et al. (2016); Cheng and Bunger (2019). Here we begin by introducing a modified approximate solution with concept we will call a "composite viscosity" to assist with quantifying the impact of leak-off. We then show how leak-off is incorporated via the global energy balance and, in turn, how the algorithm underlying the C4Frac simulator is built on this global energy balance. The model is then validated through comparison with benchmark solutions for a single Dontsov (2016) and multiple hydraulic fractures Peirce and Bunger (2015). We then illustrate the effect of leak-off, showing the existence of an optimal viscosity.

D. Governing Equations

Hydraulic fractures are considered to grow transversely to a horizontal well, as illustrated by Figure III.1. The model considers an array of N planar fractures distributed within 1 stage of length Z (see Figure III.1). Hence, the spacing h_k, k=1,..N-1 between each of the fractures is such that

$$Z = \sum_{k=1}^{N-1} h_k \tag{III.1}$$

Growth of the array of HFs is driven by injection of an incompressible fluid from a wellbore at the center of each of the radially-growing HFs (Figure III.1). The HFs are taken to propagate quasi-statically (i.e. well below the speed of sound for the rock) in a permeable, linear elastic rock characterized by $E' = E/(1-\nu^2)$ for Young's modulus E, Poisson's ratio ν, and toughness $K' = (32/\pi)^{1/2}K_{IC}$ for fracture toughness K_{IC} (after Savitski and Detournay (2002)). Several additional assumptions are introduced to simplify this problem:

(I) Crack propagation follows linear elastic fracture mechanics (LEFM) Irwin (1957); Kanninen and Popelar (1985).

(II) Lubrication theory is used to describe laminar flow of a Newtonian fluid within the fracture Batchelor (1976).

(III) All HFs grow radially and parallel to one another.

(IV) Gravitational force is neglected both in the elasticity and fluid flow equations.

(V) The fluid front is coincident with the crack front Garagash (2000).

(VI) The far field in situ stress σ_o is uniform and constant.

(VII) Fracture curving is negligible.

(VIII) The leak-off flow is modeled using Carter's leak-off law Carter (1957), which is based on diffusion of fluid into the rock under the assumptions that the HF tip velocity greatly exceeds the velocity of the diffusion front, and the net pressure (difference between total fluid pressure and minimum in situ stress) is much smaller than the difference between the minimum in situ stress and the virgin formation pore pressure.

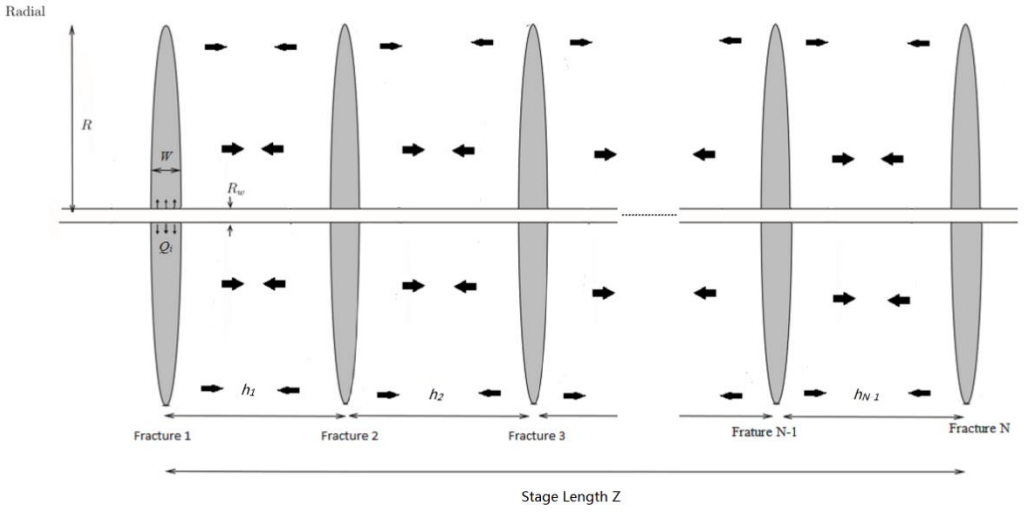

Figure III.1: Geometry of the multiple HF problem for N HFs distributed within a stage of length Z and with fracture spacing h_k. The arrows illustrate the interaction stresses between fractures.

Having established the simplifying assumptions, we turn to the description of the model. For an array of N fractures, there are $6N$ unknowns. They are, for the i^{th} fracture, the opening (also called "aperture" or "width") $w_i(r,t)$, fluid pressure $p_{f(i)}(r,t)$, fluid flux $q_i(r,t)$ fracture radius $R_i(t)$, elastic interaction stress from the other fractures $\sigma_{I(i)}(r,t)$, and inlet flow rate $Q_i(t)$, where $i=1,\ldots,N$ (see Figure III.1). Note that q is the flow velocity integrated across the fracture width. The governing equations are as follows:

1) Continuity equation for each fracture, which takes on a classical form accounting for fluid leak-off Lecampion et al. (2017)

$$\frac{\partial w_i(r,t)}{\partial t} + \frac{1}{r}\frac{\partial r q_i(r,t)}{\partial r} + \frac{2C_L}{\sqrt{t-t_i(r)}} = 0,\ C_L = \sqrt{\frac{kc_r\phi}{\pi\mu}}\Delta p_c,\ \Delta p_c = \sigma_o - p_o \qquad \text{(III.2)}$$

The final term on the left hand side accounts for leak-off according to the approach of Carter (1957), noting that it is a history-dependent function because of $t_i(r)$, which is the time at which the fracture front reaches a point with coordinate r. Additionally, C_L is the Carter's leak-off parameter, k is the rock permeability, $c_r$is the reservoir compressibility, combining the reservoir fluid and pore compressibility, ϕ is the rock porosity, and p_o is the reservoir pressure, noting that the expression for C_L presented in Equation III.2 can also be generalized to account for displacement of reservoir fluid and/or building of a low permeability filter cake Economides and Nolte (2000); Carter (1957).

2) Elasticity equation for each fracture, coupling the fracture opening $w_i(r,t)$ and traction T_i through a nonlocal integral relation Sneddon (1951)

$$w_i(r,t) = \frac{8R_i(t)}{\pi E'}\int_{\rho_i}^{1}\frac{s}{\sqrt{s^2-\rho_i{}^2}}\int_0^1\frac{xT_i(xs,t)}{\sqrt{1-x^2}}dxds \quad \rho_i = r/R_i(t) \qquad \text{(III.3)}$$

where $E' = E/(1-\nu^2)$ for Young's modulus E and the traction is a combination of the internal pressure, interaction stress imposed by the other fractures ($\sigma_{I(i)}$), and far field stress given by

$$T_i(\rho_i, t) = p_{f(i)}(\rho_i R_i, t) - \sigma_{I(i)}(\rho_i R_i, t) - \sigma_o \tag{III.4}$$

3) Poiseuille equation for laminar flow of an incompressible Newtonian fluid Batchelor (1967)

$$q_i(t) = -\frac{w_i(r,t)^3}{12\mu}\frac{\partial p_{f(i)}(r,t)}{\partial r} \tag{III.5}$$

where $\mu' = 12\,\mu$, for dynamic viscosity μ.

4) Propagation condition according to Linear Elastic Fracture Mechanics (LEFM), where K_I denotes the mode I (opening) stress intensity factor and K_{Ic} denotes the model I fracture toughness, and the propagation condition is given by Rice (1968)

$$K_I = K_{Ic}, \qquad K_I = 2\sqrt{\frac{R_i(t)}{\pi}}\int_0^1 \frac{T_i(\rho_i, t)}{\sqrt{1-{\rho_i}^2}}\rho_i d\rho_i \tag{III.6}$$

5) Interaction stress, summing the compressive stress exerted on fracture *i* by all of the hydraulic fractures in the array based on the details of the pressure distribution inside each HF Peirce and Bunger (2015). Let $\sigma_{j,i}$ represent the interaction stress fracture *j* performs on fracture *i*. Quantifying this interaction stress generally requires calculation from a 3D elasticity solver. Later we will describe a method for its approximation; for now we represent the interaction stress in a generic form given by

$$\sigma_{I(i)} = \sum_{j=1}^{N, j\neq i} \sigma_{j,i} \tag{III.7}$$

6) Constraints on the inlet fluid pressures and sum of the fluid fluxes at the fracture inlets. These impose that the inlet pressures are the same (tied together by the wellbore assuming zero pressure

loss due to fluid flow through the wellbore) and the fluid fluxes sum to the total injection rate Q_o, i.e. volume balance is satisfied for the wellbore. Hence,

$$p_{f(1)}(R_w,t) = p_{f(2)}(R_w,t) = \cdots = p_{f(N)}(R_w,t), \qquad \sum_{i=1}^{N} Q_i(t) = Q_o \tag{III.8}$$

R_w is the wellbore radius to represent the inlet. This system of 6N equations is thus comprised of 4N field equations, 1N moving boundary equations (the propagation condition), and 1N conditions governing the transient values of the influxes to each fracture. This system is completed by the initial conditions ($t=0$)

$$R_i=0,\ w_i=0,\ q_i=0 \text{ and } p_{f(i)}=0\ , \tag{III.9}$$

boundary conditions at the crack tip given by Detournay and Peirce (2014); Detournay (2004)

$$w_i(R_i,t)=0,\ q_i(R_i,t)=0\ , \tag{III.10}$$

and the inlet boundary condition

$$2\pi r q_i(r,t) = Q_i \text{ at } r \to 0 \tag{III.11}$$

The problem, then, consists of solving this system of governing equations in order to find the 6N unknown quantities, $w_i(r,t)$, $p_{f(i)}(r,t)$, $\sigma_{I(i)}(r,t)$, $q_i(r,t)$, $R_i(t)$ and $Q_i(t)$ as a function of the given quantities Q_o, C_L, μ', K', E' ,R_w, N, h_k, and t.

E. Approximation

As with the exact system of governing equations, the approximations entails coupling of six basic parts. These are as follows:

1. Approximation of the Pressure Distribution

Approximation of the Pressure Distribution, taking on a functional form consistent with the asymptotic behavior of the pressure expected near both the inlet and leading edge of the hydraulic fracture. Assuming a functional form of the pressure distribution drastically decreases computational intensity by removing the need to carry calculate the distribution at each time step based on, say, a finite difference discretization of the governing equations of fluid flow.[28] However, a suitably accurate estimate cannot be obtained with an arbitrary functional form. Here we select the form of the fluid pressure expressed as

$$p_{f(i)}(r,t) = \left(\frac{\mu_i^c(t)E'^2}{t}\right)^{\frac{1}{3}} \Pi_i(\rho_i) + \sigma_o, \quad \rho_i = r/R_i(t)$$

$$\Pi_i(\rho_i) \cong A\left[\omega - \frac{2}{3(1-\rho_i)^{\frac{1}{3}}}\right] - B\left(ln\frac{\rho_i}{2} + 1\right), \qquad \omega \approx 2.479 \tag{III.12}$$

$A = 0.3581$[19] and $B = 0.09269$[19]

This functional form entails expressing the pressure as a superposition of: 1) a spatially uniform pressure, 2) a pressure that is singular like the distance from the tip to the -1/3 power, and 3) a pressure that is logarithmically singular at the inlet. The tip singularity embodies the asymptotic form simultaneously satisfying Poiseuille flow, continuity, and elasticity Desroches et

al. (1994), while the inlet singularity follows directly from the combination of Poiseuille flow and the inlet flow boundary condition (Equation III.13). If we let $\mu_i^c(t) = \mu$, where μ is the actual fluid viscosity, the assumed functional form gives an accurate semi-analytical solution for a single circular hydraulic fracture driven by a constant injection rate through an impermeable rock in the viscosity dominated regime Savitski and Detournay (2002). Here "viscosity dominated" refers to the regime where the energy dissipation associated with the rock fracture toughness is negligible compared to the energy dissipation associated with viscous fluid flow Detournay (2004). The novelty introduced by this method is to allow $\mu_i^c(t)$ to be a degree of freedom, chosen as a part of satisfying the equations described in the rest of this section. We find that this quantity varies in such a way that it embodies additional energy dissipation associated with leak-off, and hence we call this quantity a "composite viscosity" because it acts like a viscosity but it is a composite dissipation parameter accounting for more than just the fluid viscosity.

Having introduced a functional form of the pressure that appropriately captures the asymptotic form at the inlet, we can substitute the pressure from Equation III.12 into Poiseuille Equation III.5, keeping the leading order term near the inlet arising from the logarithmic singularity of the pressure. By doing this, we obtain a constraint from the inlet boundary condition (Equation III.13), namely

$$w_i(0, \mu_i^c(t)) - \left(\frac{Q_i(t)\mu'}{2\pi B \left(\frac{\mu_i^c(t) E'^2}{t} \right)^{\frac{1}{3}}} \right)^{\frac{1}{3}} = 0 \qquad \text{(III.13)}$$

where $w_i(0, \mu_i^c(t))$ is the width at the inlet obtained from the non-local elasticity relationship described in the third part of the approximation.

2. Global Volume Balance

Global Volume balance provides a weak form approximation to the local volume balance accounted for by the complete model (Equation III.2). By integration of the local volume balance (Equation III.2) subject to the inlet and tip boundary conditions (Equations III.10 and 11), we arrive to the global volume balance equation

$$2\pi \int_0^{R_i(t)} w_i(r, \mu_i^c(t)) r dr + 4\pi C_L t^{1/2} \int_0^{R_i(t)} \sqrt{1-(r/R_i(t))^{\alpha_i}}\, r dr = \int_0^t Q_i(t) dt \qquad \text{(III.14)}$$

Note that for the purpose of enabling rapid calculation of the fluid leakoff, we do not explicitly use the evolving radius but instead approximate its history, $R_i(t) = At^{1/\alpha_i}$. This does not imply the fractures are restricted to follow power law growth – their radii are the result of the coupled solution. Rather, rapid calculation is facilitated by this approximation of the history dependence of the integral associated with the contact time $t_i(r)$ is replaced using

$$\left(\frac{r}{R_i(t)}\right)^{\alpha_i} = \frac{t_i(r)}{t}, \alpha_i = 1/(dlogR_i/d\log t) \qquad \text{(III.15)}$$

Additionally, it is convenient to express the radius R_i as the product of a dimensionless radius $\gamma_i(t)$. This quantity is an unknown found via solution to the system of approximate equation, and a characteristic radius, with a form that follows from the solution of Savitski and Detournay (2002), given by

$$R_i(t) = \gamma_i(t) \left(\left(\frac{E' t}{\mu_i^c(t)} \right)^{1/3} \int_0^t Q_i(t) dt \right)^{1/3} \qquad \text{(III.16)}$$

Using this scaling of the radius aids the solution method because it enables searching for roots of the γ_i, which are around 1, rather than searching for roots of R_i, for which it is more difficult to obtain a suitable initial guess. This improvement of the initial guess using a scaling-type relationship enables more rapid convergence of the solution algorithm and avoids spurious convergence in the event that R_i has multiple non-physical roots.

3. Elasticity

The local crack opening $w_i(\rho_i, \mu_i^c(t))$ appearing in volume balance (Equation III.14), which also includes the inlet opening used in the inlet boundary conditions (Equation III.13), is determined by elasticity through Equation III.3 with $T_i(\rho, \mu_i^c(t), t)$ as the traction acting across the surfaces of the i^{th} crack given by

$$T_i(\rho_i, \mu_i^c(t), t) = \left(\frac{\mu_i^c(t)E'^2}{t}\right)^{\frac{1}{3}} \left\{ A\left[\omega - \frac{2}{3(1-\rho_i)^{\frac{1}{3}}}\right] - B\left(ln\frac{\rho_i}{2} + 1\right)\right\} - \sum_{j=1}^{N, j\neq i} \sigma_{j,i} \quad \text{(III.17)}$$

Again we recall that $\sigma_{j,i}$ denotes the interaction stress performed by the neighboring fractures j loading on fracture i approximated as described in the next point.

4. Interaction Stress Approximation

Interaction stress approximation, using an equal volume, uniformly-pressurized crack. The full elasticity solution accounting for the non-uniform and transient pressure within each growing fracture is a major source of computational expense. To enable rapid computation, an

approximation has been proposed by Dontsov (2016), where the non-uniform pressure is replaced by a uniform pressure, choosing this uniform pressure for each HF at each time step so as to generate a fracture with the same volume as the actual HF being opened by a non-uniform internal pressure, that is

$$P_j = \frac{3}{16}\frac{E' V_j}{{R_j}^3} \quad V_j = 2\pi \int_0^{R_j(t)} w_j\left(r, \mu_j^c(t)\right) r dr \tag{III.18}$$

where P_j is the adjusted uniform internal net pressure for the j^{th} hydraulic fracture resulting from uniformly-pressurized ellipsoidal crack. Then, according to the solution of Sneddon (1946), the normal component of the stress performed by neighboring crack j on crack i is approximated as

$$\sigma_{j.i} = \frac{2P_j}{\pi}\left\{ {\delta_{j,i}}^{-\frac{1}{2}} cos\frac{1}{2}\varphi_{j,i} - tan^{-1}\frac{{\delta_{j,i}}^{\frac{1}{2}} sin\frac{1}{2}\varphi_{j,i} + \tau_{j,i} sin\theta_{j,i}}{{\delta_{j,i}}^{\frac{1}{2}} cos\frac{1}{2}\varphi_{j,i} + \tau_{j,i} cos\theta_{j,i}} \right.$$
$$\left. + \zeta_{j,i}{\delta_{j,i}}^{-\frac{3}{2}} cos\left(\frac{3}{2}\varphi_{j,i} - \theta_{j,i}\right) - \zeta_{j,i}{\delta_{j,i}}^{-\frac{1}{2}} sin\frac{1}{2}\varphi_{j,i} \right\} \tag{III.19}$$

where

$$\tau_{j,i} = \left(1 + \zeta_{j,i}^2\right)^{\frac{1}{2}} \quad \delta_{j,i} = \left\{ \left[\left(\rho_i \frac{R_i}{R_j}\right)^2 + \zeta_{j,i}^2 - 1 \right]^2 + 4\zeta_{j,i}^2 \right\}^{\frac{1}{2}}$$
$$\theta_{j,i} = arctan\left(\frac{1}{\zeta_{j,i}}\right) \quad \varphi_{j,i} = arccot\left\{ \left[\left(\rho_i \frac{R_i}{R_j}\right)^2 + \zeta_{j,i}^2 - 1 \right] / 2\zeta_{j,i} \right\} \tag{III.20}$$

Here $\zeta_{j,i}$ is the ratio of spacing $h_{j,i}$ (between fracture i and j) to the crack radius R_j, and recall that ρ_i is the ratio of radial position r to fracture radius R_i, $\rho_i = \frac{r}{R_i}$. Note that the $\zeta_{j,i}$ value decreases as the fracture grows, that is, as R_i increases for each fracture.

5. Inlet Conditions

Inlet Conditions, given by the equality of the inlet pressures and the summation of the inlet fluxes to the total influx to the wellbore expressed in Equation III.8. Satisfying these conditions requires estimation of the inlet pressures. In a full solution these would be obtained from the computed fluid pressure distribution. In the present case we have approximated the fluid pressure distributions. Because the functional form has a singularity at the inlet (Equation III.12), computing the inlet pressure would require prescribing a finite wellbore radius, thus introducing an often-spurious sensitivity of the solution to the wellbore radius and potential for substantial errors due to the large pressure gradient near the inlet. A more robust approach is to treat these inlet pressures as unknowns, prescribing them so as to be consistent with global energy balance. Such an approach is described in the point to follow.

6. Global Energy Balance

It is difficult to get an accurate estimate of the wellbore pressure due to singularity in the pressure there, so instead the approximation computes the pressure at the wellbore so as to satisfy global energy balance, expanded from the expression proposed by Bunger (2013); Lecampion and Detournay (2007) to consider fluid leak-off and given by

$$p_{f(i)}(R_w, t)Q_i(t) = \dot{U}_\iota - \dot{W}_{o(i)} - \dot{W}_{I(i)} + D_{c(i)} + D_{f(i)} + D_{L(i)} \qquad \text{(III.21)}$$

Here the left-hand side is the rate of energy input (product of the pressure and inflow rate) to the i^{th} fracture. The first five terms on the right hand side are, respectively: 1) rate of change of elastic strain energy, 2) rate of work performed on the fracture by the pre-existing (far-field) stress, 3)

rate of work performed on the fracture by the stress field generated by its neighbors, 4) rate of dissipation due to rock breakage, 5) rate of dissipation due to fluid flow. These are detailed in (Cheng and Bunger (2016); Cheng et al. (2016); Cheng and Bunger (2019); Bunger (2013)) and are summarized in the Appendix A.A. The change comes in the last term on the right-hand side, which represents the energy dissipated into the surrounding rock due to fluid leak-off. Taking a thermodynamics approach, let region S constitute a system that is open with respect to the exchange of fluid mass. Here we introduce S as the surface region of hydraulic fracture, so that the evolution of the energy associated with leak off is the result of two processes, namely, the propagation process of the boundary of S, and the influx or efflux of fluid mass across ∂S. A classical form of the dissipation for such a system is expressed by Lecampion and Detournay (2007)

$$D_L = \oint_{\partial S} p_f \vec{n} \cdot \overrightarrow{v_L} ds \tag{III.22}$$

where p_f, $\vec{n}$ and $\overrightarrow{v_L}$, respectively, denote the fluid pressure, the outward unit normal vector, and the velocity of the flux of the fluid loss. Hence Equation III.22 quantifies the integrated rate of work performed by the traction $p_f \vec{n}$ that has the effect of altering the masses of all the fluid components within region B per unit time. For Carter's leak off model (Equation III.2), the fluid loss velocity has only one non-zero component, v_L, which is directed from the inside to the surrounding formation and which has a magnitude given by Equation III.2. Additionally, following Carter's assumption Carter (1957) that fluid pressure is nearly equal to the far field stress, $p_{f(i)}(\rho_i R_i, t) \approx \sigma_o$, an efficient approximation for the incorporation of leak off is given by

$$D_{L(i)} = 4\pi \frac{\sigma_o C_L R_i (\mu_i^c(t), t)^2}{t^{1/2}} \int_0^1 \frac{\rho_i}{\sqrt{\sqrt{1-{\rho_i}^{\alpha_i}}}} d\rho_i \tag{III.23}$$

Recall that the other terms $\{\dot{U}_\iota, \dot{W}_{o(i)}, \dot{W}_{I(i)}, D_{c(i),} D_{f(i)}\}$ relate to the first term on the right hand side represents the energy required to open the fracture against the in situ confining stress, the increase in elastic strain energy, the work exerted on the hydraulic fracture via the stresses induced by its neighbors, the energy dissipation associated with rock breakage and the energy dissipated in viscous fluid flow. Upon substitution unknowns μ_i^c and γ_i with implicit dependence on Q_i via the pressure, width, and radius expressions (Equations III.12, 13, 16 and 17), the expressions for the energy terms are given by (see details in Appendix A.A)

$$\dot{U}_\iota = \sum_{j=1}^{N, j\neq i} \left(-\frac{2}{9}\right) \pi \gamma_i(t)^2 \left(\frac{\mu_i^c(t) E'^{\,8}}{t}\right)^{\frac{1}{9}} \left(\int_0^t Q_i(t)dt\right)^{\frac{2}{3}} \int_0^1 w_i(\rho_i, \mu_i^c(t)) \Pi_{net(i)}(\rho_i, \mu_i^c(t)) \rho d\rho \tag{III.24}$$

$$\dot{W}_{o(i)} = -\sigma_o[\langle Q_i(t)\rangle - \frac{4\pi C_L \gamma_i^2(t)}{t^{\frac{1}{2}}} \left(\left(\frac{E't}{\mu_i^c(t)}\right)^{\frac{1}{3}} \int_0^t Q_i(t)dt\right)^{\frac{2}{3}} \int_0^1 \frac{\rho_i}{\sqrt{\sqrt{1-\rho_i}^{\alpha_i}}} d\rho_i] \tag{III.25}$$

$$\dot{W}_{I(i)} = -\sum_{j=1}^{N, j\neq i} \begin{Bmatrix} 2\pi min\{R_i, R_j\}^2 \\ \int_0^{min\left\{\frac{R_i}{R_j}, 1\right\}} \sigma_{I(i)}\left(\rho_i \frac{R_i}{R_{j,}} t\right) \frac{dw_j}{dt} \rho_j d\rho_j \\ +2\pi R_i \frac{dR_i}{dt} \sigma_{I(i)}(1,t) w_j\left(\frac{R_i}{R_j}, \mu_i^c(t)\right) \end{Bmatrix} \tag{III.26}$$

$$D_{f,p(i)} =$$

$$\pi\left(\frac{\mu_i^c(t)E'^2}{t}\right)^{\frac{2}{3}}\int_0^1 w_i\left(\rho_i,\mu_i^c(t)\right)^3\left[\left(\frac{\partial\Pi_{f(i)}(\rho_i)}{\partial\rho_i}\right)^2-\left(\frac{B}{\rho_i}\right)^2\right]\rho_i d\rho_i \quad \text{(III.27)}$$

$$D_{f,ln(i)} = \pi\left(\frac{\mu_i^c(t)E'^2}{t}\right)^{\frac{2}{3}}\int_0^1 w_i(0,\mu_i^c(t))^3\left(\frac{B}{\rho_i}\right)^2\rho_i d\rho_i \quad \text{(III.28)}$$

$$D_{L(i)} = 4\pi\frac{\sigma_c C_L\gamma_i^2(t)}{t^{1/2}}\left(\left(\frac{E't}{\mu_i^c(t)}\right)^{1/3}\int_0^t Q_i(t)dt\right)^{2/3}\int_0^1\frac{\rho_i}{\sqrt{\sqrt{1-{\rho_i}^{\alpha_i}}}}d\rho_i \quad \text{(III.29)}$$

F. Algorithm

We have replaced the need to solve for $6N$ unknowns ($w_i, p_{f(i)}, \sigma_{I(i)}, q_i,\ R_i$ and Q_i) with $3N$ unknowns (γ_i, μ_i^c and Q_i) satisfying $3N$ implicitly interaction-dependent equations obtained from global volume balance (Equation III.14), inlet Poiseuille flow (Equation III.13), equality of wellbore pressures (Equation III.8), and summation of inlet fluxes to the total pumping rate (Equation III.8). Hence, the solution method solves

$$\left\{\begin{array}{c} 2\pi\gamma_i(t)^2\left(\frac{E'\,t}{\mu_i^c(t)}\right)^{2/9}\int_0^1 w_i(\rho_i,\mu_i^c(t))\rho_i d\rho_i + \\ 4\pi C_L t^{\frac{13}{18}}\gamma_i(t)^2\left(\frac{E'}{\mu_i^c(t)}\right)^{\frac{2}{9}}\int_0^1\sqrt{1-{\rho_i}^{\alpha_i}}\rho d\rho \\ = \left(\int_0^t Q_i(t)dt\right)^{\frac{1}{3}} \\ \gamma_i(t)\mathcal{F}\{0,T_i(\rho_i,\mu_i^c(t),t)\}\left(\int_0^t Q_i(t)dt\right)^{\frac{1}{3}} \\ = \left(\frac{\pi^2 Q_i(t)\mu' E'^2}{2^7 B}\right)^{\frac{1}{3}} \\ p_{f(1)}(R_w,t) = p_{f(2)}(R_w,t) = \cdots = p_{f(N)}(R_w,t) \\ \sum_{i=1}^{N} Q_i(t) = Q_o \end{array}\right\} \xrightarrow{yields} \begin{Bmatrix}\mu_i^c(t)\\ \gamma_i(t)\\ Q_i(t)\end{Bmatrix} \tag{III.30}$$

Recall that $w_i(\rho_i, \mu_i^c(t))$ is obtained from elasticity (Equation III.3), wherein the pressure distribution is given by Equation III.17. Additionally, as previously mentioned, the $p_{f(i)}(R_w, t)$ are obtained from global energy balance (Equation III.21).

The procedure for obtaining the approximate solution is as follows:

1. Define input parameters ($\sigma_c, C_L, E', \mu', Q_o, h_i$).
2. For the starter solution it is specified such that $Q_i(t_o) = Q_o/N$, where t_o is a specified initial time (well before leak-off and interaction become important). Additionally, based on the zero toughness, zero leak-off, zero interaction solution of Savitski and Detournay (2002), initially $\alpha_i(t_o) = 4/9$.
3. Equations III.13 and 14 are then be solved using Newton's method.
4. After that, the power balance (Equations III.24- 29) is solved.
5. The iteration procedure is performed until the desired level of convergence of $Q_i(t)$ is reached, that is, $Q_i(t)$ no longer change by very much at each iteration. Once $Q_i(t)$ is obtained, the value of $\alpha_i(t)$ is updated according to $\alpha_i = 1/(dlogR_i/d\log t)$, which follows from the presumed power law growth of the radius.
6. Then the time step is advanced by Δt, noting that $Q_i(t)$ and $\alpha_i(t)$ can be used as the pre-guessed value for $Q_i(t + \Delta t)$ and $\alpha_i(t + \Delta t)$.
7. Repeat steps 3-6 until the desired total pumping time is achieved.

G. Validation And Overall Behavior Of The Solution

1. Single Fracture

The accuracy of the approximate solution is verified by comparing to reference solutions. There will be two such comparisons. The first is to test the method for incorporating leak-off by comparison to a closed-form approximate solution for a penny-shaped hydraulic fracture Savitski and Detournay (2002). This reference solution captures the transition behavior of hydraulic fractures between negligible and large leak-off and between large viscosity and large toughness regimes. In the present case we consider just the large viscosity limit and the corresponding transition from storage to leak-off regimes. Figure III.2 shows comparison between the approximate solution (labeled lines) and the reference solution (non-labeled lines) for three examples using $C_L = \{10^{-5}\ \mathrm{m/s^{1/2}},\ 10^{-4}\ \mathrm{m/s^{1/2}},\ 10^{-3}\ \mathrm{m/s^{1/2}}\}$ with the remaining parameters fixed as $E' = 9.5$ GPa, $K' = 1\ \mathrm{Pa \cdot m^{1/2}}$, $\mu = 1\ \mathrm{Pa \cdot s}$, $Q_o = 0.1\ \mathrm{m^3/s}$.

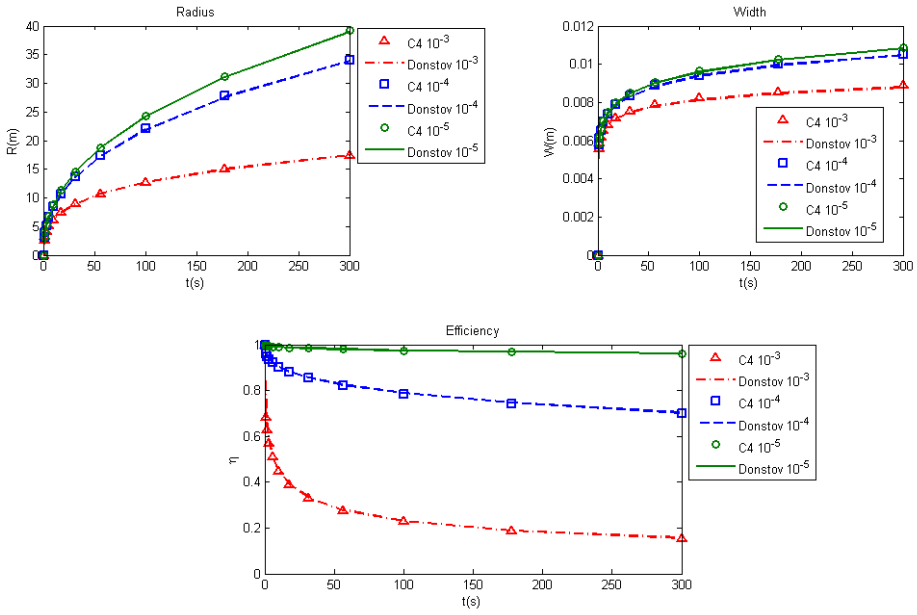

Figure III.2: Comparison between the approximation solution (labeled line) and the reference solution (non-labeled line) in terms of time histories of: (*a*) fracture radius, (*b*) width at the wellbore (ρ =0) and (*c*) efficiency. The three different lines and symbol types indicate the C_L ={10^{-5} m/s$^{1/2}$, 10^{-4} m/s$^{1/2}$, 10^{-3} m/s$^{1/2}$} cases.

This comparison demonstrates accuracy of the simulator for radius, fracture width at the wellbore, and efficiency - within one percent of the benchmark solution. Hence it is shown that the incorporation of leak-off is accurately accounted in the method.

2. Multiple Fractures

The second benchmark comparison is for multiple fractures in the zero leak-off regime. The benchmark solutions are provided by the fully coupled simulator (ILSA II), which is the extension for multiple, parallel planar hydraulic fractures Peirce and Bunger (2015) of the Implicit

Level Set Algorithm ("ILSA", Peirce and Detournay (2008)), including full 3D elastic coupling between the simultaneously propagating fractures. ILSA II solves the same underlying system of equations, albeit generalized compared to those presented in this paper for planar fracture growth geometry that can take on any shape, not just the radial geometry as we restrict here. The elasticity equation is solved using a 3D displacement discontinuity method, fluid flow is solved using the Finite Volume method, and the moving boundary condition of the advancing crack tip is handled through an implicit time stepping method that projects the front location based on the known asymptotics for a propagating hydraulic fracture tip.

We benchmark and illustrate the use of the model considering cases with 4, 5 and 6 HFs. The fractures are placed symmetrically relative to the middle of fracture array. Hence for 4 fractures, the "outer" fractures, 1 and 4, are identical. So also the "inner" fractures, 2 and 3, are identical. Similarly, for 5 fractures, fracture 1 and 5 are the "outer" fractures and 2 and 4 are the "inner" fractures. Fracture 3 always occupies the center of the array and will henceforth be called the "middle" fracture. For 6 fractures, 1 and 6 are the "outer" fractures, 2 and 5 are inner fractures, 3 and 4 is the "middle" fractures. The following parameter set is used for both the C4Frac and ILSA II simulations:

$$C_L=0\ \mathrm{m/s^{1/2}},\ E=9.5\ \mathrm{GPa},\ \nu=0.2,\ K_{IC}=0\ \mathrm{MPa\cdot m^{1/2}},$$

$$\mu=1\ \mathrm{Pa\cdot s},\ Q_o=0.1\ \mathrm{m^3/s},\ Z=20\ \mathrm{m},$$

$$\sigma_o=70\ \mathrm{Mpa},\ R_w=0.2\mathrm{m}.$$

For each case, we present comparisons of the time evolution of fracture radius, fluid influx to each fracture, fracture opening at the center, and total fracture area. We also present three-dimensional projection plots showing the radius of each HF with color scale corresponding to the HF width. Figure III.3 shows result from a 4-fracture case where the HFs are non-uniformly spaced

so that h_1 = 5 m and hence fracture planes have z coordinates (in meters) z_1=0, z_2=5, z_3=15, and z_5=20. Figure III.4 shows results for a non-uniformly spaced 5-fracture array in which fractures 2 and 4 are moved so that h_1=3.6 m, corresponding to fracture planes having z coordinates (in meters) z_1=0, z_2=3.6, z_3=10, z_4=16.4, and z_5=20. Figure III.5 shows results for a non-uniformly spaced 6-fracture array in which fractures 2, 3, 4 and 5 are moved so that h_1=2.75 m, h_2=4.25 m, corresponding to fracture planes having z coordinates (in meters) z_1=0, z_2=2.75, z_3=7, z_4=13, z_5=17.25 and z_5=20. In all cases, the results presented include: a) The radius normalized by the total interval length $R_i(t)/Z$, b) the inflow rate $q_i(R_w, t)$, c) the crack aperture at the inlet $w_i(R_w, t)$ and d) the total fracture area defined as

$$A(t) = \sum_{i=1}^{N-1} {R_i}^2(t)\,\pi \tag{III.31}$$

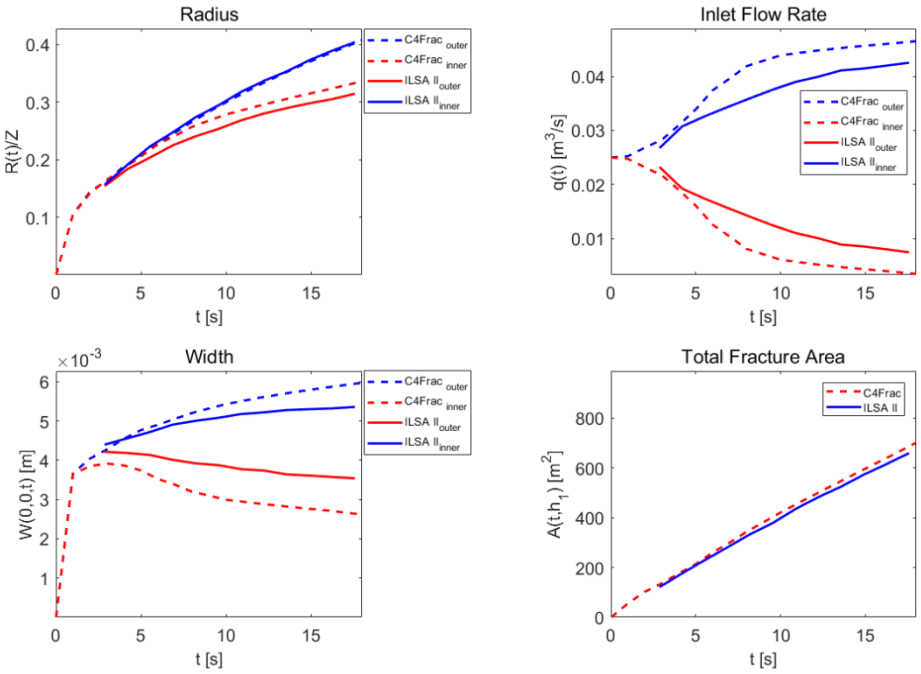

Figure III.3: C4Frac compared with ILSA II for a non-uniform 4-fracture array with $h_1 = h_3 = 5$m, $h_2 = 10$m.

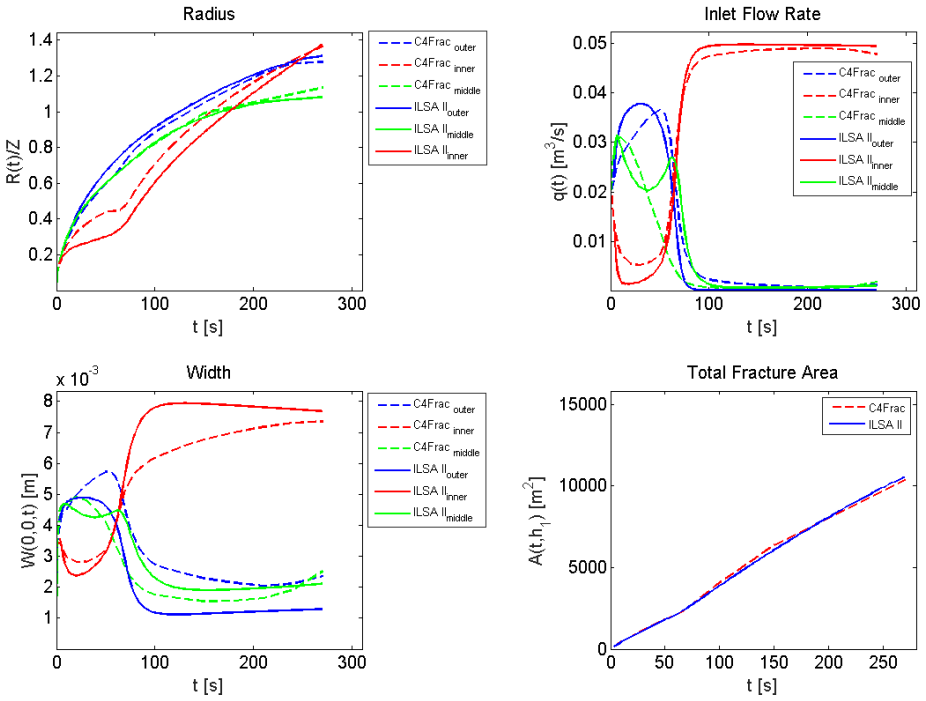

Figure III.4: C4Frac compared with ILSA II for non-uniform 5-fracture array with $h_1 = h_4 = 3.6$m and $h_2 = h_3 = 6.4$m.

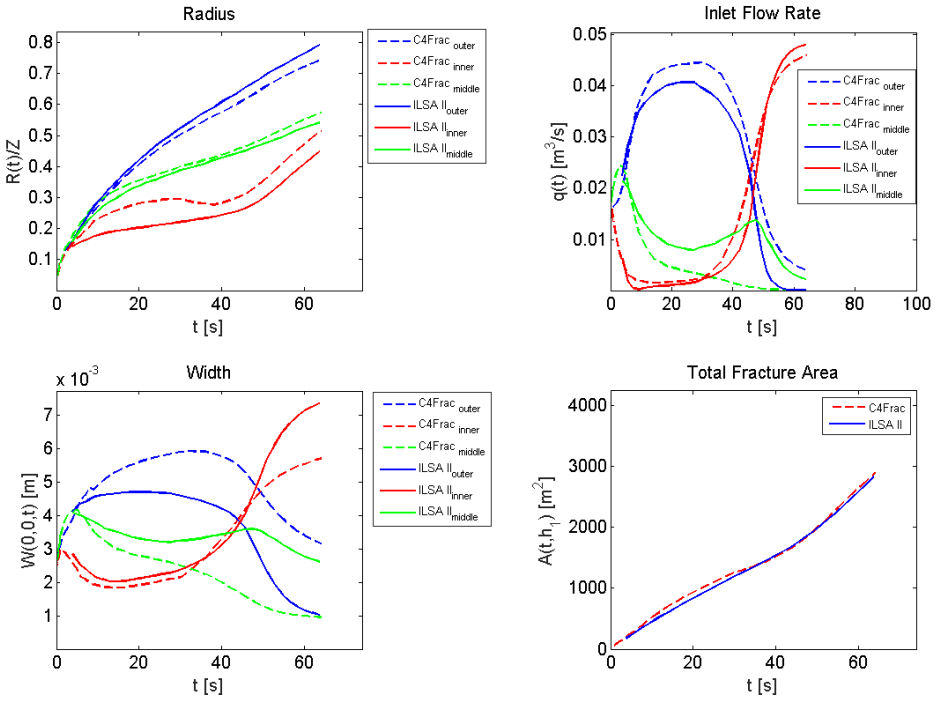

Figure III.5: C4Frac compared with ILSA II for non-uniform 6-fracture array with $h_1 = h_5 = 2.75$m, $h_2 = h_4 = 4.25$m and $h_3 = 6$m.

Overall the approximation is good, especially for the area, which is naturally the most important when optimization is to be carried out on the created fracture area. The fracture radius is also reasonably well-approximated, within about ten percent. This quantity is especially important if optimization is to be carried out on fracture uniformity. Finally, the inlet flow rate and width are approximated sufficiently so as to obtain reasonable estimated of radius and area, but with periods of time with some mismatch. The cases in Figures III.4 and 5 are actually selected because they are the most difficult to match because of the reversal of dominance of some fractures over a certain period of time and then, later, due to a "squeeze-out" effect (first observed by Peirce and Bunger (2015)), dominated by other fractures. For example, in the 5 fracture case presented

in Figure III.4, fluid flow within the inner fractures becomes dominant after 100s. At the same time, the swelling inner fractures induce a compressive force which has the effect of advancing the fracture by the displacing the fluid from the vicinity of the wellbore rather than by influx from the wellbore. The inner fractures dominated growth after this reversal. Such a reversal promotes greater uniformity and larger fracture surface area Peirce and Bunger (2015).

H. Optimization

In this section we will present a proof of concept demonstrating use of the approximate simulator to choose viscosity. But, before continuing it is important to point out that one of the key unresolved issues in the background of the discussion running through this paper is what is meant by “optimized”. The practically-relevant answer relates a measure of productivity of the well to a measure of the inputs such as materials and associated costs. Even this metric is not clearly defined and would vary depending on business objectives associated with a well. But, even if this metric were well-defined, until our model is coupled to a reservoir simulator, production cannot be predicted. As a result, optimization cannot, yet, directly be carried out in terms of production using this simulator. Nonetheless, in order to demonstrate the capacity for optimization and to give a first pass at predicting a production-optimizing configuration, here we will adopt the fracture surface area as our metric of the effectiveness of a treatment. The surface areas will be compared at the same volume of injected fluid. Under these circumstances we propose that maximizing fracture surface area is a reasonable objective because it scales to production both in classical predictions of production from hydraulic fractures Economides and Nolte (2000). and in more recent approaches relating to the Stimulated Reservoir Volume (SRV) Fisher et al. (2002). To the

latter point, here we note that SRV was originally defined based on the geometry of microseismic clouds Warpinski et al. (2005) but, to have a direct connection to forecasted production, it must essentially correspond to the area of hydraulic fractures times the characteristic width of the region of drainage around the hydraulic fractures. Hence, our first metric for a successful treatment is the total surface area of all the fractures in the array until time *T*, which we represent by *A* (Equation III.30).

In addition to maximizing surface area, a uniform array of hydraulic fractures is important for efficient utilization of the entire reservoir that is contacted by a horizontal well. The metric by which we evaluate the performance of a given configuration is taken according to a parameter U, which is determined as the inverse value of dimensionless standard deviation for the radius, viz.

$$U = 1/\sqrt{\frac{1}{N}\sum_{i=1}^{N}\left(\frac{R_i - \tilde{R}}{\tilde{R}}\right)^2} \tag{III.32}$$

Here $\tilde{R}$ is the average radius for *N* fractures. According to this metric, more uniform growth is represented as large values of *U*, i.e. it approaches infinity for perfectly uniform growth.

The problem of a viscosity dominant penny-shaped fracture with fluid loss and no lag has two limiting regimes of propagation Dontsov (2016); Detournay (2004). The first is the storage viscosity regime, which we will denote as simply "*M*" regime, corresponding to the limit of zero leak-off. The second is the leak-off viscosity regime, which we will denote as simply "$\widetilde{M}$", which corresponds to the regime in which the velocity of fluid entering the surrounding formation exceeds the rate of increase in the fracture aperture (width). Hydraulic fractures typically evolve from the storage to the leak-off regime, and correspondingly the $M\widetilde{M}$ means the transition regime between M and $\widetilde{M}$.

The illustration of optimization will consider selection of fluid viscosity. Increasing the viscosity of the fluid leads to larger fracture opening (width) which, in turn, decreases the fracture area generated by a given volume of fluid. This larger width is also accompanied by larger interaction stress which can decrease uniformity for fractures that grow to be long relative to their separation (prior to fracture interaction large viscosity promoted uniformity, see e.g. Bunger (2013). However, decreasing the viscosity increases the rate of fluid loss to the formation (see its inclusion in the leak-off coefficient C_L, Equation III.2), thereby also decreasing the fracture volume and hence area. Hence, it is reasonable to anticipate an area-maximizing viscosity to exist that is large enough to prevent excessive fluid loss but small enough to avoid excessive fracture width. One can obtain a first-pass estimate of this viscosity by looking for the intersection between the single fracture solutions corresponding to zero and large leak-off (see details in the Appendix A.B). From such considerations, an estimate of the optimal viscosity is proposed as

$$\mu_{op} = 4.036\left(\frac{2^6 E^4 t^7}{Q_o^6}\right)^{1/13} {C_{L0}}^{18/13} \tag{III.33}$$

Here t is taken as the total pumping time and C_{L0} is a reference leak-off coefficient given by C_{L0} = $C_L(\mu$=1Pa.s), i.e. it is the leak-off coefficient when the fluid viscosity is 1Pa.s. Hence, for a given fluid viscosity, the leak-off coefficient is given by $C_L = \sqrt{\frac{1\ Pa\ s}{\mu}}\, C_{L0}$. Figure III.6 illustrates the optimal viscosity predicted by Equation III.33 at $C_{L0} = 2.89 \times 10^{-6}\ m/s^{\frac{1}{2}}$. For context, this prediction is shown along with the fracture surface area computed using zero leak-off solutions for 2 and 5 uniformly-growing fractures as well as the large leak-off solution for 5 uniformly growing fractures. The estimated optimum corresponds nearly to the intersection between the 2-fracture zero leak-off solution and the 5-fracture large leak-off solution.

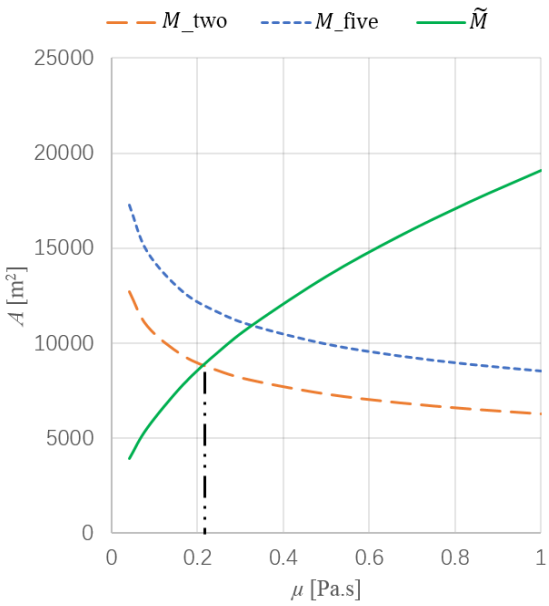

Figure III.6: Total fractured area A varies with viscosity calculated analytically and obtained from the limiting vertex solution for M vertex at 2 fractures (solid orange line) and 5 fractures (solid blue line) and 5 fracture $\widetilde{M}$ vertex. The intersection crossed black vertical line indicates μ_{op}.

Next we use C4Frac to illustrate the variation of the total fracture surface area for cases with 5 fractures. The results are shown in Figure III.7, contrasting low permeability ($C_{L0} = 2.89 \times 10^{-7}\ m/s^{\frac{1}{2}}$), intermediate permeability ($C_{L0} = 2.89 \times 10^{-6}\ m/s^{\frac{1}{2}}$), and high permeability ($C_{L0} = 2.89 \times 10^{-5}\ m/s^{\frac{1}{2}}$) formations. For reference we also compare the numerical result from C4Frac with the $M\widetilde{M}$ viscosity-storage-leak edge solutions at 2 and 5 fractures. It is interesting to note that the area predicted by the 5-fracture numerical solution tracks closer to the solution for 2 uniform fractures for the case of low permeability, to the case of 5 uniform fractures for intermediate permeability, and it exceeds the uniform fracture solution for the high permeability case. We also note that, although the area-optimizing viscosity differs somewhat from the

prediction of Equation III.33, the analytical solution does predict the order of magnitude of the optimal viscosity which, in this case, is valuable for narrowing the search space, i.e. by providing a suitable “initial guess” for the optimization. Otherwise the search for the optimal viscosity, which ranges from 0.003 Pa s for the low permeability case to 50 Pa s for the high permeability case, can fail to converge due to a poor initial guess or inappropriate search bounds.

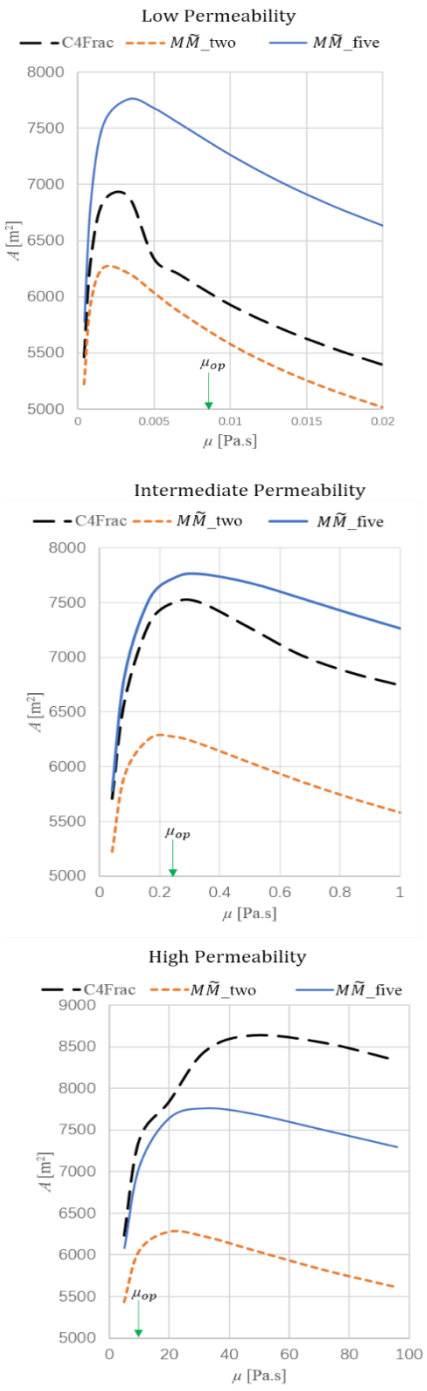

Figure III.7: Comparison between the C4Frac (dashed black line) and the limiting solution (solid arrows) in terms of total fractured area A at t =300s. Results are shown for different C_{L0} represented as low, intermediate, and high permeability. The green arrow indicates the optimal viscosity predicted by Equation III.33.

This observed behavior is controlled primarily by interplay between two mechanisms. Firstly, as viscosity increases, increased efficiency will promote larger fracture area. Counteracting this trend, increasing width with larger viscosity will decrease the radius extension. Thus a turning point will occur as more fluid contributes to the crack opening instead of length. This is the same premise as used for the derivation of Equation III.33, and hence it is not surprising that Equation III.33 can roughly predict as the optimal solution, as detailed in Appendix A.B.

Secondly, let us revisit the observation that upon changing the C_{L0} so as to transition from low to intermediate permeability cases, a transition between $M\widetilde{M}$ (2 fractures) to $M\widetilde{M}$ (5 fractures) is obtained. This is understood to be the consequence of the interplay between leak-off and stress shadow. For less fluid loss, the induced stresses from the outer fractures on the inner and middle fractures increase due to the increasing crack aperture. Under this situation, the inlet flow rate to the outer fractures consumes most of the total influx to the wellbore – hence convergence to the 2 fracture approximation for the low permeability case. In turn, driven by the lowered interaction caused by higher leak-off, a more uniform and correspondingly higher total area of growth is achieved – hence convergence to the 5 uniform fracture approximation for the intermediate permeability case. Finally, in the high permeability case, the multiple fracture numerical solution exceeds the area predicted by either the 2 or 5 fracture limit because the interaction among the fractures leads to decreased fracture width and hence larger fracture area.

Recall that $\eta_i(t)$ is the efficiency, defined as the ratio between the current fracture volume and the total amount of injected fluid into fracture i. We plot efficiency η and uniformity U (Equation III.32) as a function of the viscosity μ, with constant stage lengths $Z=20m$ and injection rates $Q=0.1m^3/s$ for intermediate permeability ($C_{L0} = 2.89 \times 10^{-6}\ m/s^{\frac{1}{2}}$). These results are presented in Figure III.8.

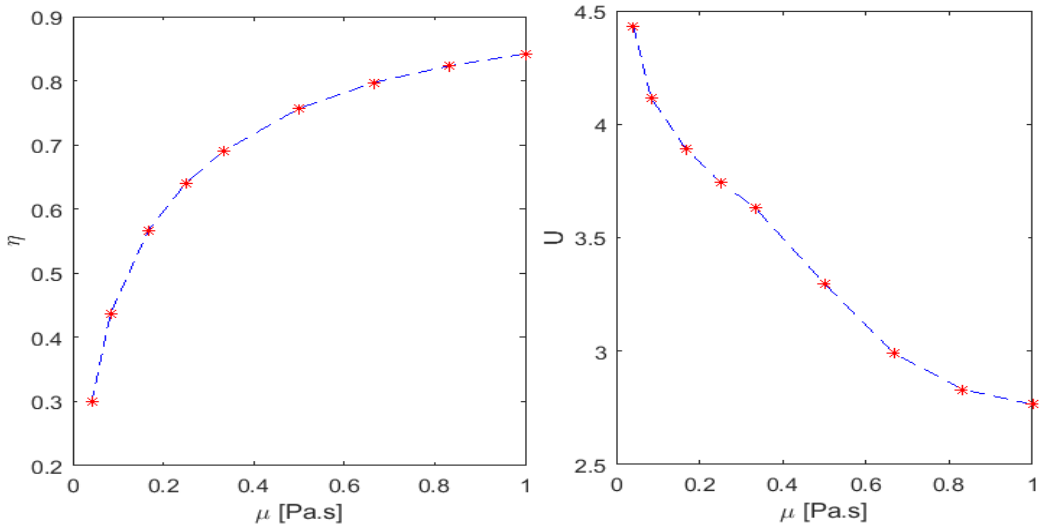

Figure III.8: Illustrative examples of the competition between global efficiency η and uniformity U.

Firstly, we observe that, as expected, the higher viscosity leads to higher efficiency. It is understandable because viscosity is inversely related to the leak-off parameter C_L. While this relationship is not surprising, somewhat less intuitively and more notably the results show that a lower viscosity is required to maximize the uniformity. This is because both lower viscosity and its accompanying larger fluid loss reduce the hydraulic fracture width and thereby minimize the stress shadow. The consequence is reflected as lower relative difference between fractures in Figure III.8. By choosing μ between 0.2 $Pa \cdot s$ and 0.4 $Pa \cdot s$, that is, by balancing the efficiency and uniformity, results in 10% to 40% relative increase in the total fractured area at 300 seconds. Note that this increase is illustrated in the particular configuration of uniform spacing; full exploration that includes non-uniform spacing is a separate topic and better to do when the model

is further updated to include the impact of fracture toughness rather than the present limit to the zero-toughness (viscosity-dominated) regime.

To better understand the competition between efficiency and uniformity, 3D projections are employed to illustrate the extent of the leakoff. In Figure III.9, the color scale in storage zone (left) represents the width of the infiltrated zone (right), calculated using the leak-off volume accommodated by complete displacement of pre-existing reservoir fluid into a rock with 10% porosity. Three choices for viscosity are compared: 0.04 Pa s, 0.25 Pa s and 1 Pa.s. It is thereby shown again that higher viscosity leads to lower fluid loss but higher non-uniformity. Also, again there is an optimal viscosity due to the competition between efficiency and uniformity. Then it is understandable that much higher viscosity is required to obtain a balance between the leak-off and uniformity as C_{L0} increases, i.e. in a higher permeability formation.

$\mu = 0.04\ Pa.s$

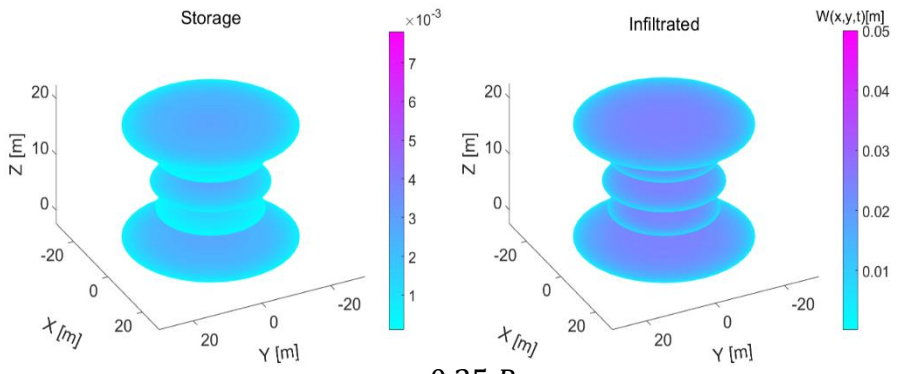

$\mu = 0.25\ Pa.s$

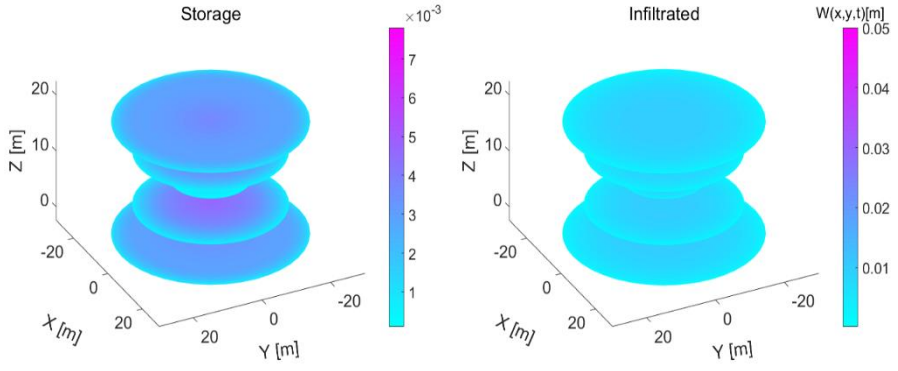

$\mu = 1\ Pa.s$

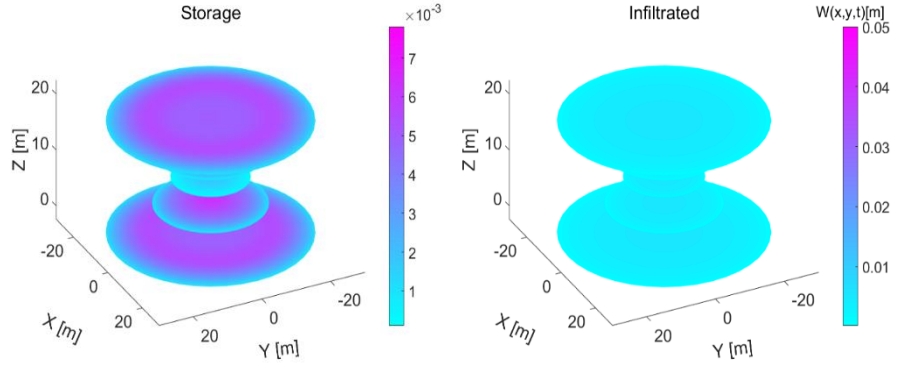

Figure III.9: Crack Propagation and infiltrated zone width for uniform spacing at $\mu =$ 0.04 Pa. s, 0.25 Pa. s and 1 Pa. s.

I. Conclusion

This paper presents a novel approach to obtaining an approximate solution for a system of simultaneously growing radial hydraulic fractures, including the impact of the leak-off. The leak-off is incorporated by introducing a so-called “composite viscosity”, which allows a rapid and convenient method for accounting for the energy dissipation accompanying the interplay among interacting fractures, viscous fluid flow, and fluid leak-off. The approximate solution is validated through benchmarking with a fully-couple, planar 3D hydraulic fracture simulator. The utility of such a rapidly-computing solution is then demonstrated by introducing a method for determining fluid viscosity maximize fracture surface area and/or fracture uniformity.

The results show that there is a tradeoff between uniformity and efficiency that is somewhat an art of balance. High viscosity leads to high fracture efficiency which, on one hand drives higher fracture area. But, high efficiency and the larger fracture widths that accompany high viscosity fluids leads to greater suppression of some fractures due to stress shadow, thereby diminishing both generated fracture surface area and fracture uniformity.

Overall, the novelty is driven by the rapidly computing of C4Frac. The simulator takes only minutes to compute (often close to 5 minutes) on a typical personal computer. Via hundreds of simulations, optimization and parametric analysis becomes practically-achievable – in contrast to the prohibitive computational times associated with hundreds of simulations for simulators that take hours to days to compute a single case.

IV. Model-Based Evaluation Of Methods For Maximizing Efficiency And Effectiveness Of Hydraulic Fracture Stimulation Of Horizontal Wells

A. Preamble

Noticed that C4Frac and its' protype models is valid to the so-called "viscosity-dominated" regime wherein far more energy is dissipated in fluid flow compared with rock fracturing Cheng and Bunger (2016); Cheng et al. (2016); Cheng and Bunger (2019a); Cheng and Bunger (2019b). Hydraulic fracturing is governed by at least three physical processes that are associated with fluid viscosity, fracture toughness, and leak-off. To this point, consideration has been limited to a viscosity dominated regime, where most energy is dissipated in fluid flow and the rock fracture toughness has negligible impact on the solution. However, regime transition to cases where rock fracture toughness is important will occur when viscosity becomes very small, injection rate is decreased (including via diversion of fluid to more favorable fractures within a given stage), and/or stiffness of the rock is decreased. Capturing the transition behavior between growth regimes is therefore essential to understand the combined impact of fluid flow, rock breakage, and leak-ff on the growth of simultaneously-growing hydraulic fractures. Extending the concept of "composite viscosity", through the inclusion of a newly defined toughness coefficient, the energy balance is coupled with the rock breakage energy thereby including dissipation associated with rock fracture in an efficient manner. C5Frac therefore approximates the growth of multiple hydraulic fractures with energy dissipated due to both rock breakage or fluid flow. The accuracy is verified by the comparison to semi-analytical solutions Dontsov (2016) and high fidelity simulations using ILSA II (cite). The model is the first to give such an efficient and accurate solution to multiple fractures

transitioning between viscosity and toughness dominated regimes and with leak-off varying from negligible to large enough that most fluid is lost to the formation. Enabled by such rapid and accurate solutions, a parametric study is carried out to explore optimization of treatment parameters. Finally, the impact of in-situ stress variability on optimization reveals that the best optimization approach is dependent on the stress variation dominant by in-situ stress or interaction stress. These results are presented in Cheng (2019c) and included in Part VI of this thesis.

B. Key Points

- Evaluating options for promoting uniform hydraulic fracture growth and maximizing fracture area.
- High pressure "large limited entry" can be effective when most stress variation is from in-situ stress instead of fracture interaction.
- A lower pressure option with non-uniform fracture spacing is most effective when stress variation is mainly due to fracture interaction.

C. Abstract

Hydraulic fracturing enables oil and gas extraction from low-permeability reservoirs, but there remains a need to reduce the environmental footprint. Resource use, contaminant-bearing flowback water, and potential for induced seismicity are all scaled by the volume of injected fluid. Furthermore, the greenhouse gas emissions associated with each extracted unit of energy can be

decreased by improving resource recovery. To minimize fluid use while maximizing recovery, a rapidly-computing model is developed and validated to enable the thousands of simulations needed to identify opportunities for optimization. Lower pumping pressure approaches that minimize pressure loss through the wellbore perforations combined with non-uniform spacing are shown to be capable of substantially reducing fluid consumption and/or increasing created fracture surface area when the stress variation is mainly from fracture interaction instead of in-situ stress. When in-situ stress variation is dominant, "limited entry" methods promote more uniform growth but with higher pumping pressures and energy consumption.

D. Plain Language Summary

This paper identifies opportunities to drastically reduce (predicted on some cases to be up to 65%) water use associated with hydraulic fracture stimulation of low permeability (i.e. shale) oil/gas reservoirs with minimal impact on recovery rates. It also identifies opportunities to increase (up to 120%) the recovery rates of oil/gas for the same injected volume (i.e. keeping the injected volume the same). The key lies in leveraging the mechanics of fracture interaction to produce arrays of hydraulic fractures that are as uniform as possible while balancing an intrinsic trade-off between fracture aperture and surface area. To achieve optimal outcomes, there are different strategies that include promoting uniform fracture growth by designing treatments with large pressure loss as fluid flow through the perforations in the casing and into the fracture (so-called "limited entry" method) and selecting non-uniform fracture spacing that balances the stresses induced by fracture growth. Through thousands of simulations enabled by a validated, rapidly-computing simulator, we find different strategies are advantageous depending upon the reservoir

conditions and most notably on the variability and/or uncertainty in the in-situ stress. This work therefore points to an area of ongoing research capable of having an enormous, global impact on the environmental footprint of shale gas/oil production.

E. Introduction

Hydraulic fracturing (HF) is a well-stimulation technique used in oil and gas wells for nearly 70 years. One modern manifestation of this method, multistage fracturing of horizontal wells, uses 8-40 million liters (2-10 million gallons) of water to fracture a single well Kargbo et al. (2010). Concern has been raised over the increasing quantities of water for hydraulic fracturing in areas that experience water stress, particularly in arid or semi-arid regions, such as China's Ordos Basin Smakhtin et al. (2004); EIA, (2011) and the United States' Eagle Ford formation and the Permian Basin Scanlon et al. (2014); Kondash et al. (2018). In some areas, for example the Marcellus shale play in the Appalachian Basin, water is relatively plentiful but transportation is difficult and disposal options for flowback water are limited Brantley et al. (2018); Mitchell et al. (2013). The particularities of water-related problems can therefore be specific to a region. However, the overall commonality is that water management presents one of the greatest challenges to both the present and future development of onshore oil and gas development throughout the world. Water-related challenges and impacts can include resource scarcity (e.g., Smakhtin et al. (2004); Scanlon et al. (2014); Kondash et al. (2018)), flowback of contaminated water (e.g., Shrestha et al. (2017); He et al. (2017); Sun et al. (2013); Xiong et al. (2016)), pollution associated resource transportation (e.g., Brantley et al. (2018); Mitchell et al. (2013); Vengosh et al. (2014); Entrekin et al. (2018)), and injection-induced seismicity (e.g., Ellsworth (2013); Fischer

(2011); Guglielmi et al. (2015)). These, and indeed most water-related challenges, risks, and impacts essentially scale in magnitude with the volume of fluid used for hydraulic fracturing Vengosh et al. (2014); Entrekin et al. (2018); Ellsworth (2013). Thus motivated, here we focus on two ways the process of extracting oil and/or gas from shale can move towards lower intensity of resource use per resource recovered. The first is reducing resource consumption associated with hydraulic fracturing processes. Additionally, because there is not only a monetary, but also an environmental and societal cost to every well, it is arguably of equal importance to maximize return on the investment by ensuring the best-possible recovery rates. Indeed, among other things, the greenhouse gas (GHG) emissions per unit of energy produced (i.e. kg CO_2eq/MWh) associated with drilling and completion of wells is inversely proportional to the so-called "estimated ultimate recovery" (EUR) Laurenzi and Jersey (2013); Vafi and Brandt (2016). Hence, high resource usage efficiency will reduce GHG emissions, and so this paper will also address a second objective, which is to explore opportunities to increase resource recovery rates.

An important opportunity for reduction of injected volume and/or increasing of recovery rates lies in the widespread observation that 20 to 40 percent of perforation clusters do not contribute significantly to production Miller et al. (2011). Horizontal wells are stimulated by injection through clusters of holes ("perforations") in the casing that connect the well to the surrounding formation. Typically, stimulation takes places in stages, with the intention for 3-6 of these perforation clusters to be stimulated simultaneously as a part of a single stage. One driving factor for the non-uniformity of production from these perforation clusters is the non-uniformity of in-situ stresses, along the well (e.g., Baihly et al. (2010); Cipolla et al. (2011)). "Stress shadowing" is another factor, referring to the suppression of some HFs as a result of the compressive stresses exerted on them by nearby HFs (e.g., Sesetty and Ghassemi (2013); Abass et

al. (2009); Fisher et al. (2004); Meyer and Bazan (2011)), illustrated by the sketch in Figure IV.1b. Such uneven growth will drive a non-uniform fluid distribution, which inefficiently utilizes the injection fluid (and indeed the wellbore that has been drilled), thus decreasing the efficiency of resource usage.

Here we compare and contrast two approaches to mitigating non-uniform fracture growth. The first has become common practice and entails designing the well perforations so that the pressure drop associated with flow through these holes in the casing is similar to or greater than the pressure associated with hydraulic fracture growth Howard and Fast (1970); Weng et al. (1993); Lecampion and Desroches (2015). This so-called "limited entry" (or "extreme limited entry" when the perforation pressure drop is several times greater than the fracturing pressure) promotes uniform fluid distribution by using the perforation holes like hydraulic chokes. However, as with any mechanism that increases near wellbore friction loss, it comes with a cost of raising overall pumping pressure and hence the pumping power requirements, costs, and CO_2 emissions are increased. Another approach that is predicted by models Peirce and Bunger (2015), but remains relatively untested in the field is to manipulate other variables in order to mitigate the tendency of stresses generated by growing fractures to lead to suppression of some fractures and dominance of other fractures (so-called "stress shadow"). By using a rapidly-computing simulator that gives sufficiently accurate approximation to high fidelity models (C5Frac), it is practical to run the thousands of evaluations needed to reveal the conditions under which each strategy is expected to be advantageous.

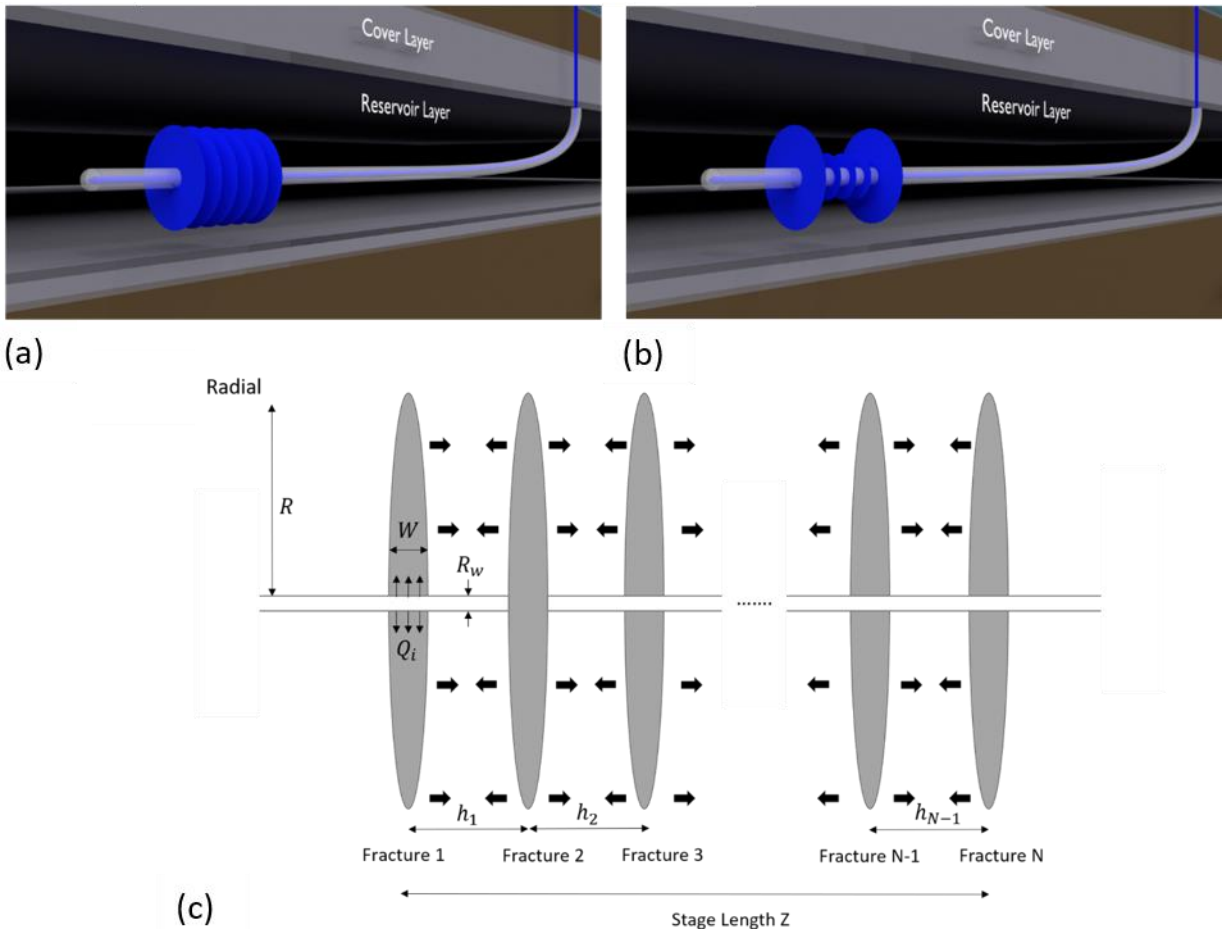

Figure IV.1: Illustration of multiple, simultaneous HFs in one stage. (a) Ideal, uniform result, and (b) Result in which central fractures are suppressed. (c) Geometry of the multiple HF problem for N HFs distributed within a stage of length Z and with fracture spacing h_k. The arrows illustrate the interaction stresses between fractures. Figure adapted from Cheng and Bunger (2016).

F. Methods

To leverage the opportunity for optimization provided by non-uniform stimulation of perforation clusters, a model is required. But optimizing is challenging due to a variety of well-documented difficulties Abass et al. (2009) that combine to make high-fidelity simulation time-consuming. Optimization that requires hundreds to thousands of model evaluations is impractical with high-fidelity models.

For this reason, a first step enabling optimizing the resource use and resource recovery is to address the need for rapid, even if approximate, simulation including capturing the transition behavior between multiple fracture growth regimes. We previously demonstrated the feasibility and basic concept of a new HF simulator, C4Frac, which very rapidly simulates the growth of an array of HFs Cheng and Bunger (2019b). In this prototype reduced order model (ROM), the fractures created from all perforation clusters were restricted to radial, planar growth under the limitation that fractures propagate without toughness (i.e. energy dissipated in fluid flow greatly exceeds energy dissipated due to rock breakage). In the present work, we introduce a modified method to incorporate the toughness into the model so that it is possible to simulate the impact of fluid flow, rock breakage, and fluid loss to the formation ("leak-off") on the growth of multiple, simultaneously-growing hydraulic fractures. In addition to the time-saving provided by the new method, the accuracy is also verified through comparison to benchmark solutions. The model, and its validation, are described in detail in the Supplementary Materials, with a brief overview provided here.

The model considers an array of N simultaneously-growing hydraulic fractures, shown in Figure IV.1c. For this system, there are 6N unknowns which comprise the solution desired from a mechanical model. They are, for each (i^{th}) fracture: 1) the opening (also called "aperture" or "width") $w_i(r,t)$, 2) fluid pressure $p_{f(i)}(r,t)$, 3) fluid flux $q_i(r,t)$, 4) fracture radius $R_i(t)$, 5) elastic interaction stress from the other fractures $\sigma_{I(i)}(r,t)$, and 6) inlet flow rate $Q_i(t)$, where i=1,…,N. The problem consists of solving a system of governing equations in order to find the 6N unknown quantities as a function of the given quantities, namely: i) total injection rate Q_O, ii) Carter's leak-off coefficient C_L, iii) viscosity μ, iv) toughness K_{Ic}, v) plane strain elastic modulus E', vi) wellbore radius R_w, vii) spacing $(\text{between fracture } i \text{ and } j)$ $h_{j,i}$, viii) number of fractures N, and ix) injection time .

1. Overall Solution

The solution method and associated assumptions and simplifications follow from our prior work Cheng and Bunger (2016); Cheng and Bunger (2019), but with an important extension that allows for consideration of finite fracture toughness. The prior models were limited to consider cases where energy dissipation associated with rock fracture was negligibly small compared to viscous dissipation associated with fluid flow. The details of the model and its extension are in the Supplementary Materials (Appendix B.B). To summarize, the model requires simultaneous solution of 6N equations corresponding to the following physical laws:

1)Volume balance, where in our ROM we adopt a weak form wherein volume balance is assured globally but not at every location. Additionally, volume balance must account for fluid loss to the formation, and here we follow the widely-used Carter's method to describe the history-

dependent leak-off under the assumptions that the hydraulic fracture velocity greatly exceeds the characteristic fluid diffusion velocity in the rock and that the transient fluid net pressure (difference between fluid pressure and in-situ stress in the rock) is much smaller than the difference between the in-situ stress and the undisturbed pore pressure in the reservoir rock Carter (1957); Lecampion et al. (2017).

2)Laminar fluid flow describing a Newtonian fluid flowing within the fracture according to the classical Poiseuille law. In our ROM we avoid discretization by assuming a functional form that is consistent with known inlet and tip asymptotic behavior, which are the two locations where energy is predominantly dissipated.

3)Crack propagation imposing a condition for crack extension according to linear elastic fracture mechanics. In our ROM, we use an approximation whereby the energy dissipated in rock fracture is lumped into a so-called "composite viscosity" such that tip stresses need not be explicitly computed but energetic equivalence can be maintained via a modification to the resistance to fluid flow.

4)Elastic crack compliance providing a relationship between fluid pressure and crack opening satisfying linear momentum balance, strain compatibility, and a linear elastic stress-strain relationship for the rock. In our ROM, the elasticity equation is simplified by restricting growth to the radial geometry, enabling efficient solution for the opening associated with each fluid pressure distribution via a Displacement Discontinuity method (Crouch and Starfield 1983). Recall that the fluid pressure is taken to follow an assumed functional form that pressure decreases as the fracture volume increase, noting that this behavior contrasts with increasing pressure with volume in the blade-shaped Perkins-Kern-Nordgren (PKN) model. Here we consider just the radial geometry,

which captures the most interesting part of the interaction before they reach a high growth barrier provided that the fracture spacing is small enough relative to the barrier height)

5)Interaction stress produced in the interior of an elastic solid by the opening of an internal crack, thereby quantifying the stress interaction among the fractures. In our ROM, the interaction stress is computed for each fracture from the analytical solution for a uniformly pressurized crack Sneddon (1946) with an equivalent volume.

6)Inlet pressure continuity and inlet volume balance enforcing that the pressures at the inlets of each fracture are equal, that is, tied to the same wellbore and assuming negligible fluid pressure loss along the wellbore and considering friction loss using the Crump and Conway JPT (1988) model. Additionally, the inlet condition requires the sum of fluid influx to all fractures equals the total injection rate to the wellbore. Imposing this condition requires accurate calculation of the inlet pressure. We use an approach that updates the wellbore pressure so as to ensure its consistency with the overall energy balance of the system, thereby describing the inlet pressure via more robust integral quantities.

The corresponding governing equations and the details of the solution algorithm used to rapidly computing simultaneous solution to these coupled equations is described in the Supplementary Materials (Appendix B.A and B.B).

2. Validation

To check the accuracy of the developed approximate solution, it is necessary to compare predictions of the approximation to reference solutions. In this study, the validation entails two parts. One is benchmarking with a solution for a single hydraulic fracture, using a solution developed by Dontsov (2016). The model compares within a fraction of a percent for most cases, with an error of at most 7% for a certain domain of the solution where leak-off is small and fracture toughness and fluid viscosity have similar magnitudes of energy dissipation. This favorable benchmark, detailed in SI (Section S4.1), validates the solution method for the hydraulic fracture model. Furthermore, validation for cases with multiple fractures entails comparing to high-fidelity model results ("ILSA II" Peirce and Bunger (2015) developed from "ILSA" Peirce and Detournay (2008)). This validation is also achieved, and is detailed in the SI (Section S4.2). Strong agreement with the high-fidelity model, especially for the fracture area generated by each configuration, demonstrates that the approach to coupling the interacting fractures leads to an ROM that is useful for the purposes of the optimization considered in the subsequent sections.

G. Results

Before presenting a proof of concept demonstrating use of the approximate simulator for treatment design to pursue higher resource usage efficiency, it is important to adopt a more formal definition of "efficiency of resource usage". The practically-relevant answer relates a measure of estimated ultimate recoveries (EUR) of the well to a measure of the inputs such as materials and associated environmental effect. Because surface area scales to recovery both in classical

predictions of production from hydraulic fractures Economides and Nolte (2000) and in more recent approaches relating to the Stimulated Reservoir Volume (SRV) Fisher et al. (2002) (corresponding to the area of hydraulic fractures times the characteristic width of the region of drainage around the hydraulic fractures), here we will adopt the total fracture surface area ($\boldsymbol{A}$) of all the fractures in the array until time t as a proxy for the EUR of well as impacted by an HF treatment. Generating such an output requires inputs, and one of the most direct and measurable inputs is the injection volume. As previously pointed out, a number of environmental impacts and risks scale with the fluid volume, taken as $Q_O t_{TOT}$, where Q_O is the injection rate and t_{TOT} is the total injection time. Hence, an optimally efficient treatment can be considered alternately as one using the least volume of fluid to generate a given fracture area or as one generating the most fracture area for a given volume. Both of these forms of optimality will be examined in the demonstration that follows.

A smaller injection volume is important to reduce a variety of volume-dependent environmental impacts. Here we will examine the ability to minimize injection volume via optimization that utilizes appropriate viscosity and non-uniform spacing in a complimentary way to produce a desired fracture surface area.

1. Overall Behavior

Previously we developed reduced order models (ROMs) for estimating growth characteristics of multiple, simultaneously growing hydraulic fractures. These models were limited to the so-called "viscosity dominated" regime, in which the pressure required to overcome energy dissipated by viscous fluid flow within the fracture greatly exceeds the energy associated with rock breakage. While these prior efforts established a basic approach for ROM development for

multiple hydraulic fractures, it is useful to extend consideration to all regimes for the purpose of showing the potential for optimization over a larger number of design parameters. In order to demonstrate the dependence of the results upon nominal propagation regime, we adopt the dimensionless quantities after Dontsov (2016).

$$\Phi = \frac{\mu'^3 E'^{11} C_L'^4 Q_o}{K'^{14}}, E' = \frac{E}{(1-\nu 2)}, K' = (\frac{32}{\pi})^{1/2} K_{IC}, \mu' = 12\,\mu \tag{IV.1}$$

$$\tau = \left(\frac{K'^{18} t^2}{E'^{13} \mu'^5 Q_o^3}\right)^{1/2} \tag{IV.2}$$

where E is Young's modulus, ν is Poisson's ratio, K_{IC} is fracture toughness, and μ is dynamic viscosity. With this definition, transition from small to large τ corresponds to a transition from a regime in which viscous dissipation far exceeds rock fracturing to a regime where viscous fluid flow is negligible compare to the fracture propagation. Small Φ corresponds to negligible leak-off, while large Φ corresponds to large leak-off. Hence the lower left corner of Figure IV.2 corresponds to small leak-off and large viscosity, while the upper right corner corresponds to large leak-off and small viscosity. Note that the cases presented in Figure IV.2 are in a transition range between the limiting regimes. A more detailed discussion of the limiting and transition regimes is not directly needed in the present illustration of results, but for completeness is included in the SI Section S4.1.

Additionally, it is important to note that the leak-off coefficient C_L is coupled with the fluid viscosity, i.e. higher viscosity leads to lower leak-off. Neglecting any accumulation of particulate/polymer on the fracture comprising a low permeability "filter cake", and further assuming that the fluid injected to the fracture is not too dissimilar in viscosity to the native fluid in the reservoir, the viscosity and leak-off rate are coupled via Carter's leak-off parameter Carter (1957); Lecampion et al. (2017).

$$C_L = \sqrt{\frac{kc_r\phi}{\pi\mu}}p_\Delta,\ p_\Delta = \sigma_o - p_o \tag{IV.3}$$

where k is the rock permeability, c_r is the reservoir compressibility, combining the reservoir fluid and pore compressibility, ϕ is the rock porosity, σ_o is the in-situ stress and p_o is the reservoir pressure. Accordingly, in the parametric studies to follow, Equation IV.3 is rewritten using $C_{L0} = C_L(\mu = 1\text{Pa.s})$ as the reference leak-off coefficient. Hence for a given fluid viscosity, $C_L = \sqrt{\frac{1\ Pa\ s}{\mu}}C_{L0}$.

As an illustrative example, we show that injection volume can vary significantly depending upon both the nominal regime (location in the plots in Figure IV.2 as defined by Φ and τ Equations IV.1 and 2) and the fracture spacing. Specifically we contrast uniformly-spaced and a particular non-uniform spacing, which is inspired from prior work Cheng and Bunger (2016); Lecampion et al. (2017); Cheng and Bunger (2019) demonstrating that some non-uniform spacing configurations can balance the impact of stress shadow acting on the fractures, thereby leading to more uniform fracture growth. This parametric study entails varying viscosity and characteristic leak-off parameter C_{L0}, keeping all other quantities unchanged with practically-relevant values given by

$$R_W = 0.2\text{ m}, K_{IC} = 1\text{ MPa}\cdot\text{m}^{\frac{1}{2}}, E = 10\text{ GPa}$$
$$\nu = 0.2\ , \sigma_o = 70\text{ Mpa}, Q_o = 0.2\text{ m}^3/s, \tag{IV.4}$$

until a fracture surface area of 100,000 m^2 is achieved. Note that the value of area limit is set so as to avoid the total injection time deviating so far from the pumping time required for an average (practical) case, which is usually in the order of tens of minutes (up to, say, 100 minutes at the most). Additionally, we selected non-uniform design with $h_1 = h_4 = 9\text{m}, h_2 = h_3 = 16\text{m}$ and uniform spacing $h_1 = h_2 = h_3 = h_4 = 12.5\text{m}$ as a comparison case with the same injected volume for a total stage length $Z = 50\text{m}$ (recalling definitions in Figure IV.1). For all cases, the injected volume is computed (Figures IV.2a and b), and a comparison is then made between

uniform and non-uniform cases via the ratio of volume, V_{non}/V_{uni}. To see the effect of varying viscosity, with all other parameters held constant (except the impact of viscosity on C_L accounted for via Equation IV.3), reference lines for the viscosity and the resulting leak-off coefficient are given in Figure IV.2.

We can see an advantage is provided by the non-uniform case. We firstly observe that, except for some unpractically high leak-off regions (upper right corner, where the ratio of fracture volume to injected volume is below 5%), the non-uniform spacing always generates more fracture area than uniform spacing. This is especially true when viscosity is near 10^{-1} Pa.s and leak-off is around 10^{-6} $m \cdot s^{1/2}$; there is a more than 60% decrease in fluid volume in this practically-relevant region. In addition, a decreased volume is achieved in both uniform and non-uniform cases by choosing viscosity in an optimal range.

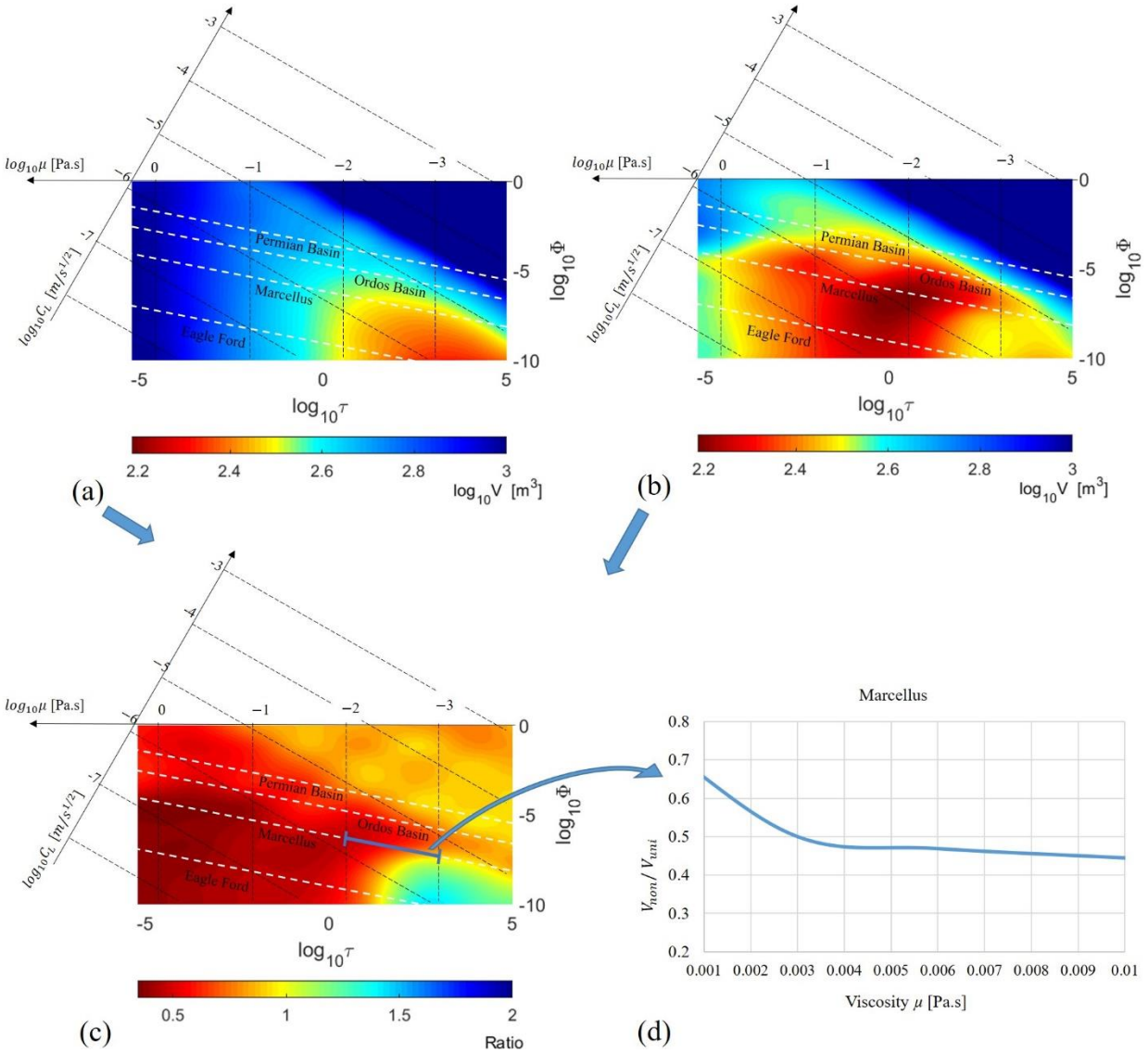

Figure IV.2: Injection volume in all practical regimes. The injected volume plotted as a function of log (τ) and log (Φ) for non-uniform and uniform space respectively: (a) uniform (b) non-uniform (c) ratio between non-uniform and uniform design. Here contours are shown of varying C_L and μ, with all other parameters according to Equation IV.4. (d) an example showing a profile of volume versus viscosity along a portion of the dashed line for the Marcellus example.

2. Interplay between Limited Entry and Variable In-Situ Stress.

The previous results show that non-uniformity of induced stresses around growing hydraulic fracture arrays leads to suppression of some fractures and favoring of others. In reality, there is also naturally-occurring stress variability due to variation of rock properties along the horizontal wellbore. Hence one can expect that the relative importance of stress shadow versus random stress variation will govern a change in overall behavior of the system and determine the best strategies for promoting uniform fracture growth. As an example, simulations are carried out using rock properties from the Marcellus formation (Table S2). The details of the basin and corresponding parameters are in the Supplementary Materials (Appendix B.F). The spacings used here are the same as in Section 3.1.1. Since the most commonly-used fluids are: slick water (0.003Pa.s), linear gel (0.05Pa.s) and crosslinked gel (0.5Pa.s), the graphs are zoomed in on the most instructive range of viscosity 0.003-1Pa.s. To account for the limited entry, the pressure loss though perforation tunnels is embedded into the simulator via the global energy balance using the power expression Bunger et al. (2014)

$$P_{perf} = aQ_i(t)^3 \left(\frac{\rho}{n^2 D_p^4 C^2} \right) \tag{IV.5}$$

The numerical factor, a, is usually taken from Crump and Conway (1988) as 0.8106. The density of injected fluid is ρ. Each cluster has n perforations, D_p represents the perforation diameter, and C is a shape factor for the perforation tunnels. Instead of a specific value for each parameter, here we give a value for the bracketed quantities in Equation IV.5 to achieve a roughly predicted pressure loss which usually range between 10^4 to 10^7 Pa. As a reference, a common limited entry design in practice involves uniform fracture spacing with $3 * 10^6 - 10^7$ Pa perforation loss. Furthermore, the in-situ stress variation is incorporated into the simulator via its contribution $\dot{W}_{o(i)}$ to the global energy balance

$$\dot{W}_{o(i)} = -\sigma_o(1 \pm S_i)\left(Q_i - 4\pi \frac{C_L R_i^2}{t^{1/2}} \int_0^1 \frac{\rho_i}{\sqrt{\sqrt{1-{\rho_i}^{\alpha_i}}}} d\rho_i \right) \tag{IV.6}$$

where S_i is the variability of the in-situ stress for each stage relative to the average stress σ_o. Details of the derivation are provided in SI Section S2.7. For the simulations, σ_o is set as 30 MPa and the S_i is taken for each case as an array of random values from the range [-v/2,v/2], where v is set at various levels and referred to as the "In-Situ Stress Variation". Latin Hypercube sampling is chosen to ensure that the broadest range of results can be found with the fewest evaluations. Here the number of random S_i between bounds is set as 18, that is, 18 realizations are computed wherein each realization entails randomly drawing S_i, $i=1,\ldots,N$ for each of the N fractures within the stage (N=5 in this example). The maximum and minimum values of all realizations are indicated by the dash dot lines in Figures IV.3a and b for 2% in-situ stress variation, with the symbols and line giving the average value from all realization. These computed ranges and average values are also portrayed in Figures IV.3c - f for differing levels of in-situ stress variation, wherein the perforation loss used in optimization is fixed at around 10^5Pa to compare with the extreme limited entry value of 10^7Pa. The viscosity corresponding to crosslinked gel is selected in Figures IV.3c and d for

comparison with viscosity of slick water in Figures IV.3e and f. Results are presented as injected volume required for a given fracture area (namely 100,000 m^2, Figure IV.3a), fracture area generated by a given injected volume (namely 460 m^3, Figure IV.3b), and the relative change of these quantities compared to a very large limited entry case which results in essentially uniform fluid distribution among the fractures (Figures IV.3c-f).

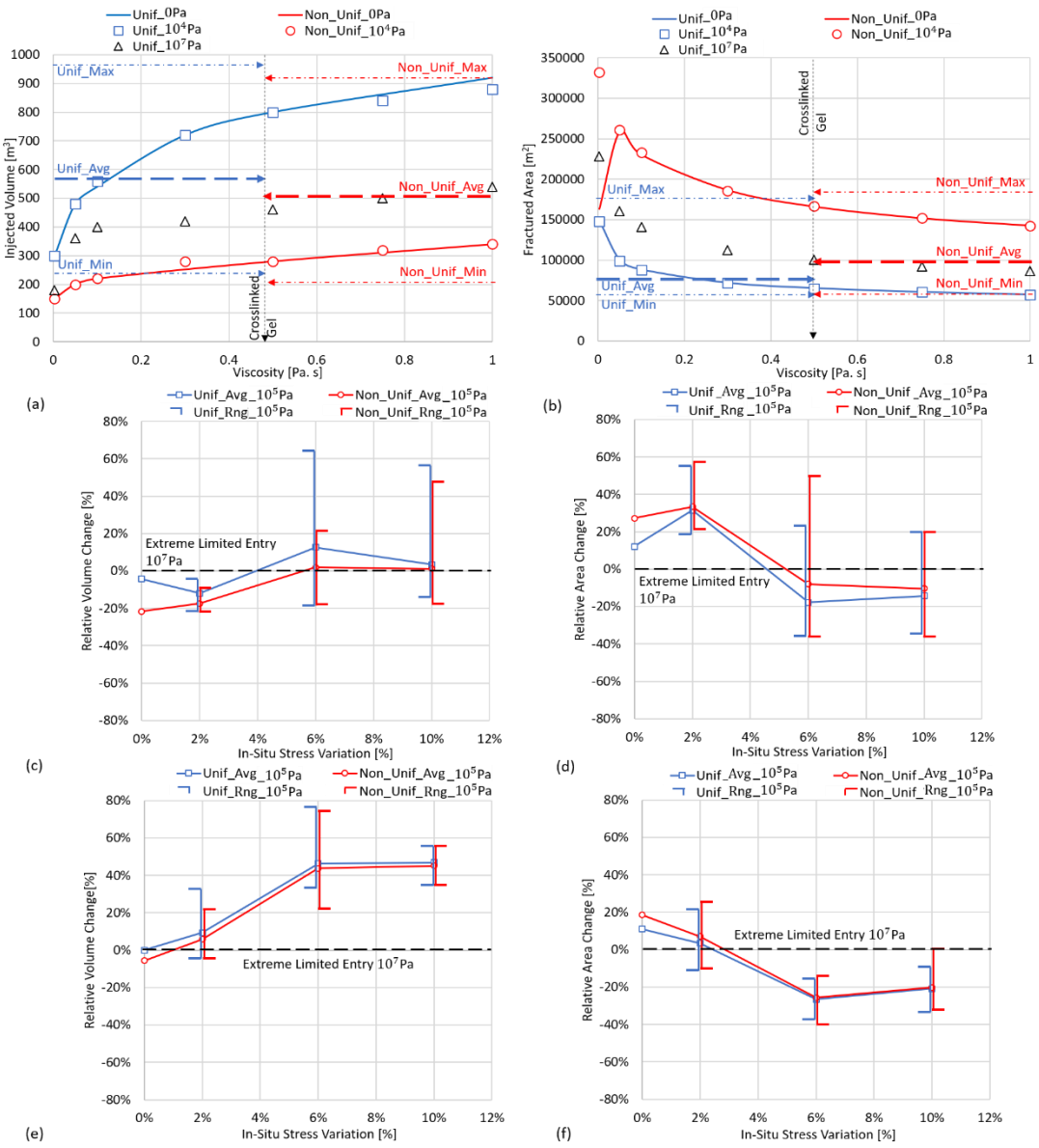

Figure IV.3: Effect of in-situ stress variation with different fluid viscosities and levels of limited entry. Note that Unif and Non_Unif means uniform and non-uniform spacing, respectively. The last digits indicate the pressure of entry loss. (a) Total injected volume comparison for generating 100,000 m2 of fracture area. (b) Total fractured area comparison for injection of 460 m3 of fluid. (c) For crosslinked gel, the relative volume change of 10^5 Pa compared to 10^7 Pa limited entry at different values of in-situ stress variation. (d) is for relative fractured area change. (e) and (f) Relative change in injection volume and fracture area, respectively, for slick water.

The results show that uniform spacing with small limited entry is never the best approach; these cases require more fluid to achieve a given fracture area and produce less fracture area for a given injected volume compared to the other cases. The conclusion is the same for all viscosities and in-situ stress variabilities and can be drawn by viewing average values and/or minimum/maximum values of the ranges.

The results also show that the advantageous choice between large limited entry and non-uniform spacing depends upon the in-situ stress variability. Specifically, if the variability of in-situ stress is below a certain value, in this example about 5%, small limited entry with non-uniform fracture spacing promotes better outcomes than large limited entry. This is to be expected because the advantage of non-uniform spacing requires that the stress shadow generated by the net fluid pressure inside the fractures has to sufficiently exceed the magnitude of the variability of in-situ stress, thereby acting as the dominant stress variability in the system. As Figure IV.3b shows, 15% less volume consumption and 20% more fractured area is enabled by small limited entry, and the net pressure is around 10^7Pa, several times greater than the corresponding in-situ stress variability 10^6Pa (at 3%). When the in-situ stress variability is above 6% (2×10^6Pa), which is close to the net pressure (10^7Pa), extreme limited entry performs better. The improved performance is because the pressure increase due to the friction loss dominates the stress variability. This leads to greater uniformity among the simultaneously growing fractures. The shift of advantageous design between small and large limited entry appears as a crossover of average possible outcomes in Figure IV.3b and c. Note that it is readily confirmed by simulations that large limited entry gives nearly identical results for uniform and non-uniform fractures spacing.

H. Discussion And Conclusions

Resource use efficiency is an issue at the heart of the environmental footprint of hydraulic fracturing. Increasing the resource usage efficiency will lead to less injection per unit recovery and/or more recovery per well leading to relatively lower GHG emissions per unit energy produced. A major challenge to optimization is that many simulation runs are required, thereby motivating development of fast, approximate models. Building on previous versions Cheng and Bunger (2019b), the new model C5Frac is developed to extend consideration to include the impact of the fracture toughness of the rock and fluid leak-off.

Based on thousands of simulations that are practically enabled by the short computation times required by C5Frac, we first observe that if in-situ stress variation is substantially less than the net pressure associated with driving fracture growth, both large limited entry and non-uniform fracture spacing are effective at promoting uniform distribution of fracture growth. The large limited entry approach leads to higher fluid pressures (hence higher cost and CO_2 emissions from pumping equipment), but gives similar and in some cases lower generated fracture areas compared to small limited entry cases. The main advantage of large limited entry is that the uncertainty in the outcome of the stimulation is much smaller, that is, the range of outcomes collapses to a point. When in-situ stress variability is low, this benefit is less pronounced and arguably not worth the "price". However, if variation of in-situ stress is high, then large limited entry can provide a significant benefit. This benefit is due to the fact that friction loss caused by the perforations provides enough pressure to overwhelm such randomness. Furthermore, in cases with large in-situ stress variation, the balancing of the stress shadow effects provided by non-uniform fracture spacing has a small impact compared to the random stress. Simulation results secondly lead to an

overall observation that non-uniform spacing will always equal or improve on uniform spacing counterparts in every sense including error bounds. Specifically, for small limited entry the non-uniform spacing clearly outperforms uniform spacing. This work demonstrates resource use efficiency is optimizable and with optimization depending upon not only deterministic values of reservoir conditions, but also on the variability of those conditions. Hence, these simulations provide impetus for systematic, ongoing, and focused efforts to identify optimizing strategies that account for uncertainty and variability of in situ stress and other rock properties.

V. Conclusions

The complete work is comprised by three parts, essentially with each part introducing one physical process to the model and exploring its impact. The processes are: 1) near field interaction stress, 2) fluid leak-off, and 3) toughness. Instead of adding coefficients for each process, a novel concept "composite viscosity" is first time presented, which integrates the near field interaction stress, leak-off and toughness in one term. Assisted by it, C5Frac can predict the performance of individual design in seconds to minutes with accuracy demonstrated by validating with the high fidelity models ILSA II and the accurate uniform approximation of Dontsov (2016). Enabled by the accuracy and speed, thousands simulations required by optimization on multiple design options are enabled.

When multiple fractures are propagating in a viscosity dominated regime, where toughness and leak-off is small enough to be negligible, modifying the spacing between clusters will stimulate a complex behavior called "reversal". The fractures that are subjected to less interaction stress are in favored by the inflow rate in beginning. However when the ratio between spacing and crack length reach a certain value, the interaction work performed by suppressed fractures will decrease due to the near tip tensile stress. To satisfy the power balance, the former inhibited fractures change behavior in order to require more fluid inflow resulting in more propagation and hence the "reversal" phenomenon. Optimized spacing is shown capable of utilizing this behavior to amplify the advantage over uniform spacing, showing doubled cracked area. Because of this prospect of optimization, it is important to be able to approximate this behavior rapidly so that optimizers can carry out many iterations. Prior to this work, it was only possible to capture this behavior with high fidelity models (i.e. ILSA, cite) or to ignore it by using far-field approximation

of the interaction stress in rapidly computing models Cheng and Bunger (2016). Hence, the first main contribution of this work is the devising of a rapidly-computing model that captures near-field stress interaction effects including the reversal phenomenon Cheng and Bunger (2019a).

During HF, fracking fluid is injected into rock formation to create sufficient permeability, allowing significant fluid flow out as the return. Due to the pores existing in the surrounding rock, the injection fluid will partially penetrate the fracture surface into formation. In some cases, most of fluid will be lost into the formation, leaving less fluid to drive fracturing. In such a case, the work presented here found, for the first time, that the value of spacing fractures non-uniformly is weakened due to less interaction to trigger reversal occur Cheng and Bunger (2019b). In fact, low fluid viscosity is shown, interestingly, to lead to more uniform growth (a benefit) but with a decreased overall fracture area. Furthermore, this work finds that large viscosity can mitigate reduced fracture area due to leak off. However, if viscosity is too high, the fracture area (i.e. the radius of circular fractures) will decrease due to the enlarged fracture width. Meanwhile the interaction stress determined by net pressure is positively correlated to viscosity, driving more non-uniform fracturing due to the increased interaction stresses. As these phenomena interplay, an optimal viscosity appears, which balances the fluid loss and storage volume, promoting more area. Identifying and quantifying this optimizing behavior comprises a second main contribution of this dissertation research.

The last, and in many ways most challenging, part is the incorporation of toughness. While there are a variety of approaches in the context of high fidelity models, accounting for both fluid flow and crack propagation without substantially increasing computation time is challenging. Up to this point, the rapidly-computing model assumed that nearly all energy dissipation was associated with fluid flow, so, if there was sufficient pressure (and, equivalently, sufficient input

power) to overcome viscous resistance to flow, it was assumed there was enough to perform the comparatively "easy" task of breaking the rock. However, while often the practically relevant case, fracturing with low viscosity fluids and/or under conditions where one or more fractures are growing very slowly, rock fracture must be considered. The contribution of this dissertation research was to devise an efficient way of accounting for rock fracture by way of an energetically-equivalent approach where the dissipation is lumped in with fluid flow via a modified value of the viscosity (cite your paper). Using this "composite viscosity", the simulator captures the transition behavior between four growth regimes that individually dominated by viscosity, viscosity-leakoff, toughness and toughness-leakoff. Furthermore, parametric study shows for the first time that the advantage of non-uniform spacing over uniform spacing is dependent on the rock properties belonging to different basins Cheng and Bunger (2019c).

In reality, the rock properties are varied, especially for the in-situ stress. High-pressure injection "extreme limited entry" is the mostly used solution, but it is costly because it required large pumping pressures. To pursue less costly alternatives, non-uniform spacing is chosen as a possible method. For varied in-situ stress, the mean value of injection volume is defined as the parameter to evaluate the resource usage. In this way, this research shows a novel path to increasing HF efficiency, namely, if the stress variability is lower than 5%, saving 20% injection fluid at same fractured area could be received though non-uniform spacing compare with extreme limited entry (cite your paper). On the other hand, for higher stress variation, extra limited entry is suggested rather than using non-uniform spacing, because it could provide big enough fluid pressure to dominate the stress distribution. According to the energy balance, the fluid will distribute more uniformly and stimulates more fracture propagation.

In summary, the dissertation research has made the following contributions to the field of hydraulic fracture simulation:

1)Development of a fast simulation method based on the novel concept of “composite viscosity”, thereby allowing inclusion of coupled effects of fluid flow, rock breakage, and fluid loss to the formation with what appears to be unprecedented combination of speed and accuracy.

2)Deployment of the validation with high fidelity models. Combined with orders’ faster calculation speed. The simulator is first time presented as a uniform solution for all propagation regimes, expanding the search scope for possible optimization on multiple design options through thousands parametric studies.

3)Revealing new insights into the consequences of so-called “stress shadow” interaction between fractures, notably indicating there exists optimal spacing with higher fractured area that partially contributed by the “reversal” growth. Most importantly, for lower in-situ stress variability, the results show that non-uniform spacing could lower the resource cost compare to “extreme limited entry” with same output.

4)Identifying the conditions under which the current state of the art “extreme limited entry” method should be considered effective and when it is unjustified due to its high pressure pumping requirements.

5)Describing an optimal viscosity for multiple interference fractures with leakoff considered. To pursue best tradeoff between fluid loss and storage that interaction induced from, a balanced crack length and width is obtained by optimal viscosity that rock properties dependent.

Looking to the future, rapid, even if approximate simulation is poised to remain essential for hydraulic fracture design, optimization, and uncertainty quantification. As the draw of previously un-economical basics drives industry to stimulation of reservoirs with all-new

combinations of rock properties, the ability to explore candidate designs to obtain optimal combinations of inputs is continuing to grow; reliance on experience is becoming increasing inadequate. Furthermore, variability of reservoir properties within many of these emerging basins leads to variability of stimulation outcomes. Quantifying this uncertainty is becoming ever more central to the role of hydraulic fracture modeling. In all of these scenarios, running many scenarios on a rapidly computing simulator is a critical technical step. Hence, the innovations put forward in this dissertation comprise steps forward in the direction of rapid simulation that is likely to grow in importance to both industrial application and academic understanding over the years and decades to come.

Appendix A Appendices For "Optimizing Fluid Viscosity For Systems Of Multiple Hydraulic Fractures"

A. Input Power

The terms on the right hand of Equation III.21 side represents the terms associated with various energy storage, work, dissipation terms and leak-off, that is (after Peirce and Detournay (2008); Bunger (2013))

U is a portion that goes into increasing the strain energy by deforming the rock strain energy – this is the recoverable elastic energy.

$$\dot{U}_\iota = \pi \int_{R_w}^{R_i} \left(T_i \frac{\partial w_i}{\partial t} + w_i \frac{\partial T_i}{\partial t} \right) r dr \tag{A.1}$$

W_o is the work on the crack by the in-situ stress – the hydraulic input power must be sufficient to overcome this negative work. To account for the fluid loss, the work by in-situ stress W_o is modified as

$$\dot{W_{o(\iota)}} = -\sigma_o \left(Q_i - 4\pi \frac{C_L R_i^2}{t^{1/2}} \int_0^1 \frac{\rho_i}{\sqrt{\sqrt{1-{\rho_i}^{\alpha_i}}}} d\rho_i \right) \tag{A.2}$$

W_I is the work done on each HF by the compressive stresses induced by its neighbors – again the hydraulic input power must be sufficient to overcome this negative work. Hence

$$\dot{W_{I(\iota)}} = -2\pi \left(\int_{R_w}^{\min(R_i R_j)} \sigma_{I(i)} \frac{\partial w_j}{\partial t} r dr + \sigma_{I(i)} \frac{dR_i}{dt} R_i w_j \left(\frac{R_i}{R_j}\right) \right) \tag{A.3}$$

D_c is the dissipation rate associated with rock breakage, taken here as the limiting case of zero toughness, i.e.

$$D_{c(i)} = 0 \tag{A.4}$$

D_f is the dissipation rate associated with viscous fluid flow given by

$$D_{f(i)} = \frac{\pi}{\mu'} \int_{R_w}^{R_i} {w_i}^3 \left(\frac{\partial p_{f(i)}}{\partial r} \right)^2 r dr \tag{A.5}$$

D_L is the fluid loss rate associated with leak-off given by

$$D_{L(i)} = 4\pi \frac{\sigma_o C_L R_i^2}{t^{1/2}} \int_0^1 \frac{\rho_i}{\sqrt{\sqrt{1-{\rho_i}^{\alpha_i}}}} d\rho_i \tag{A.6}$$

Note that, consistent with the present limitation to the viscosity regime, without further loss of generality we can assume $D_c \ll D_f$, and hence D_c is neglected.

Upon substitution of the unknowns μ_i^c and γ_i (see Section 3) with their implicit dependence on Q_i via the solutions pressure, width, and radius expressions, we obtain Equations III.24-29. For simplification, the strain energy (Equation III.24) is calculated by using an approximation inspired by the solution for a single, viscosity dominated hydraulic fracture in the absence of fluid leak-off Savitski and Detournay (2002)

$$\frac{\partial w_i}{\partial t} = \frac{\partial (W_i \Omega_i(\rho_i, t))}{\partial t} \tag{A.7}$$

$$\frac{\partial T_i}{\partial t} = \frac{\partial (p_{f(i)} - \sigma_o - \sum_{j=1}^{N, j \neq i} \sigma_{j,i})}{\partial t} \approx \frac{\partial \left(P_{f(i)} \Pi_i(\rho_i) \right)}{\partial t} \tag{A.8}$$

Where the W_i and $P_{f(i)}$ is given by Equation A.11 and A.12, respectfully, as:

$$P_{f(i)}(t) = \left(\frac{\mu_i^c(t) {E'}^2}{t} \right)^{\frac{1}{3}} \tag{A.9}$$

Additionally, $\Omega_i(\rho_i, \mu_i^c(t))$ is the dimensionless crack opening given by elasticity as $\Omega = w_i(\rho_i, \mu_i^c(t))/\, w_i(0, \mu_i^c(t))$ and $\Pi_i(\rho_i)$ is given as Equation III.17. Then after ignoring the time partial deferential in $\mu_i^c(t)$ and $\Omega_i(\rho_i, \mu_i^c(t))$ (discussed below), the terms in Equation. A.1 can be expressed as:

$$W_i(t) = \left(\frac{Q_i(t)\mu'}{2\pi B \left(\frac{\mu_i^c(t) E'^2}{t} \right)^{1/3}} \right)^{1/3} \tag{A.10}$$

$$\frac{\partial w_i}{\partial t} \approx \frac{\partial (W_i)}{\partial t} \frac{t}{W_i} \frac{W_i}{t} \Omega_i(\rho_i, \mu_i^c(t)) \approx \frac{1}{9} \frac{W_i}{t} \Omega_i(\rho_i, \mu_i^c(t)) \tag{A.11}$$

Here, to avoid additional time-cost and keep reasonable accuracy, the non-self-similar crack

$$\frac{\partial T_i}{\partial t} \approx \frac{\partial \left(P_{f(i)} \right)}{\partial t} \frac{t}{P_{f(i)}} \frac{P_{f(i)}}{t} \Pi_i(\rho_i) \approx -\frac{1}{3} \frac{P_{f(i)}}{t} \Pi_i(\rho_i) \tag{A.12}$$

propagation is assumed to be nearly self-similar in strain energy calculation, which means that the shape of crack Ω_i and dimensionless pressure distribution Π_i is simplified as stable during next time prediction of strain energy. This assumption is strengthened during storage to leak-off regime transition. As fluid loss increases, the interaction stress will decrease due to less crack volume as Equation III.18. Thus, more uniform inlet flow rate provide the condition where self-similar is more valid. After ignoring the time evolution in Π_i and Ω_i, the Equation. A.1 is expressed as Equation III.24.

B. Optimization About Viscosity

This appendix provides expressions for the radius in M and $\widetilde{M}$ vertex that are used in the paper to predict the optimal viscosity. Here M vertex refers to the viscosity-storage regime and $\widetilde{M}$ vertex refers to the viscosity-leak-off regime Dontsov (2016); Detournay (2004). The expressions for the hydraulic fracture radius are given by

$$R_M = 0.6944\left(\frac{Q_i^3 E' t^4}{\mu}\right)^{1/9} \quad R_{\widetilde{M}} = 0.4502\left(\frac{Q_i^2 t}{4C_L^2}\right)^{1/4} \tag{A.13}$$

Note that, in the limiting case of uniform fracture growth, $Q_i = Q_o/N$. So the total area for N clusters are given respectively as:

$$A_M = 0.482\pi N^{1/3}\left(\frac{Q_o^3 E' t^4}{\mu}\right)^{2/9} \quad A_{\widetilde{M}} = 0.203\pi\left(\frac{Q_o^2 t}{4C_L^2}\right)^{1/2} \tag{A.14}$$

Noted that for $\widetilde{M}$ vertex solution, the area is independent on the number of fractures, N, and increases with the viscosity due to the corresponding decrease in leak-off. For the M vertex solution, the area decreases with the viscosity because of the larger crack opening generated with higher viscosity fluids (see Equation III.13), also presented as different curve at different numbers of hydraulic fractures (2 and 5, to be exact) as Figure A1.

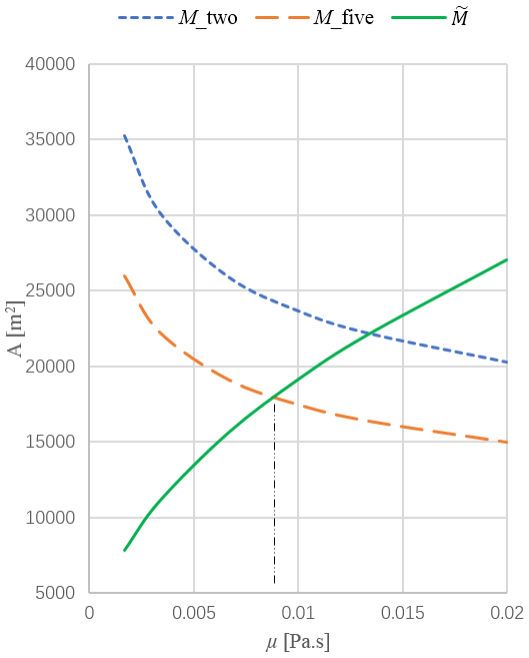

Figure A1: Total fractured area A varies with viscosity calculated analytically and obtained from the limiting vertex solution for M vertex at 2 fractures (solid orange line) and 5 fractures (solid blue line) and 5 fracture $\tilde{M}$ vertex. The intersection crossed black vertical line indicates μ_{op}.

In the example for relatively low leakoff ($C_{L0} = 2.89 \times 10^{-7}\ m/s^{\frac{1}{2}}$), we observe there is one intersection point between $\tilde{M}$ and M vertex solutions (Figure A1). We use this intersection point to provide an initial estimate of the optimal viscosity μ_{op}, by setting $A_M = A_{\tilde{M}}$, and substitute the leak-off coefficient, we find the intersection point solution as

$$\mu_{op} = 4.036 \left(\frac{N^6 E^4 t^7}{Q_o^6} \right)^{1/13} {C_{L0}}^{18/13} \tag{A.15}$$

Appendix B Appendices For "Model-Based Evaluation Of Methods For Maximizing Efficiency And Effectiveness Of Hydraulic Fracture Stimulation Of Horizontal Wells"

The main challenge relative to prior work is how to include toughness into the model; previously we developed reduced order hydraulic fracture models limited to the so-called "viscosity-dominated" regime wherein far more energy is dissipated in fluid flow compared with rock fracturing Cheng and Bunger (2019b). Here, we present a novel approach to incorporating the additional energy dissipation associated with fracture propagation via a modified "composite viscosity", i.e. by lumping dissipative mechanisms into the viscous dissipation. After describing the parts of the model and the relevant approximations, an algorithm for solving an N fracture system is detailed. The model is then validated through comparison with benchmark solutions for a single Dontsov (2016) and multiple hydraulic fractures Peirce and Bunger (2015); Peirce & Detournay (2008).

A. Governing Equations

The model description, up to the description of the inclusion of fracture toughness in the composite viscosity, follows our past contribution, most notably Cheng and Bunger (2019a). In this model, circular, planar hydraulic fractures are considered to grow transversely to a horizontal well, as illustrated by Figure IV.1. The model considers an array of N fractures distributed within 1 stage of length Z (see Figure IV.1). Hence, the spacing h_k, k=1,..N-1 between each of the fractures is such that

$$Z = \sum_{k=1}^{N-1} h_k \tag{B.1}$$

Growth of the array of HFs is driven by injection of an incompressible fluid from a wellbore at the center of each of the radially-growing HFs (Figure IV.1). The HFs are taken to propagate quasi-statically (i.e. well below the speed of sound for the rock) in a permeable, linear elastic rock characterized by $E' = E/(1-\nu^2)$ for Young's modulus E, Poisson's ratio ν, and toughness $K' = (32/\pi)^{1/2}K_{IC}$ for fracture toughness K_{IC} (after Savitski and Detournay (2002)). Several additional assumptions are introduced to simplify this problem:

(IX)Crack propagation follows linear elastic fracture mechanics (LEFM) (Irwin (1957); Kanninen and Popelar (1985)).

(X)Lubrication theory is used to describe laminar flow of a Newtonian fluid within the fracture (Batchelor (1976)).

(XI)All HFs grow radially and parallel to one another.

(XII)Gravitational force is neglected both in the elasticity and fluid flow equations.

(XIII)The fluid front is coincident with the crack front (Garagash (2000)).

(XIV)The far field in-situ stress σ_o is spatially uniform and temporally constant.

(XV)Fracture curving is negligible.

(XVI)The leak-off flow is modeled using Carter's leak-off law (Carter (1957)), which is based on diffusion of fluid into the rock under the assumptions that the HF tip velocity greatly exceeds the velocity of the diffusion front, and the net pressure (difference between total fluid pressure and minimum in-situ stress) is much smaller than the difference between the minimum in-situ stress and the virgin formation pore pressure.

Having established the simplifying assumptions, we turn to the description of the model. For an array of N fractures, there are $6N$ unknowns. They are, for the i^{th} fracture, the opening (also called "aperture" or "width") $w_i(r,t)$, fluid pressure $p_{f(i)}(r,t)$, fluid flux $q_i(r,t)$ fracture radius $R_i(t)$, elastic interaction stress from the other fractures $\sigma_{I(i)}(r,t)$, and inlet flow rate $Q_i(t)$, where $i=1,\ldots,N$ (see Figure IV.1). Note that q is the flow velocity integrated across the fracture width. The governing equations are as follows:

1) Continuity equation for each fracture, which takes on a classical form accounting for fluid leak-off [1]

$$\frac{\partial w_i(r,t)}{\partial t}+\frac{1}{r}\frac{\partial r q_i(r,t)}{\partial r}+\frac{2C_L}{\sqrt{t-t_i(r)}}=0,\ C_L=\sqrt{\frac{kc_r\phi}{\pi\mu}}\Delta p_c,\ \Delta p_c=\sigma_o-p_o \tag{B.2}$$

The final term on the left hand side accounts for leak-off according to the approach of Carter (1957), noting that it is a history-dependent function because of $t_i(r)$, which is the time at which the fracture front reaches a point with coordinate r. Additionally, C_L is the Carter's leak-off parameter, k is the rock permeability, c_r is the reservoir compressibility, combining the reservoir fluid and pore compressibility, ϕ is the rock porosity, and p_o is the reservoir pressure, noting that the expression for C_L presented in **Equation B.2** can also be generalized to account for displacement of reservoir fluid and/or building of a low permeability filter cake Carter (1957); Economides and Nolte (2000).

2) Elasticity equation for each fracture, coupling the fracture opening $w_i(r,t)$ and traction T_i through a nonlocal integral relation Sneddon (1951)

$$w_i(r,t)=\frac{8R_i(t)}{\pi E'}\int_{\rho_i}^{1}\frac{s}{\sqrt{s^2-\rho_i{}^2}}\int_0^1\frac{xT_i(xs,t)}{\sqrt{1-x^2}}dxds\quad \rho_i=r/R_i(t) \tag{B.3}$$

where $E' = E/(1-\nu^2)$ for Young's modulus E and the traction is a combination of the internal pressure, interaction stress imposed by the other fractures ($\sigma_{I(i)}$), and far field stress (σ_o) given by

$$T_i(\rho_i, t) = p_{f(i)}(\rho_i R_i, t) - \sigma_{I(i)}(\rho_i R_i, t) - \sigma_o \tag{B.4}$$

3) Poiseuille equation for laminar flow of an incompressible Newtonian fluid Batchelor (1967)

$$q_i(t) = -\frac{w_i(r,t)^3}{12\mu}\frac{\partial p_{f(i)}(r,t)}{\partial r} \tag{B.5}$$

where $\mu' = 12\,\mu$, for dynamic viscosity μ.

4) Propagation condition according to Linear Elastic Fracture Mechanics (LEFM), where K_I denotes the mode I (opening) stress intensity factor and K_{Ic} denotes the model I fracture toughness, and the propagation condition is given by Rice (1968)

$$K_I = K_{Ic}, \qquad K_I = 2\sqrt{\frac{R_i(t)}{\pi}}\int_0^1 \frac{T_i(\rho_i, t)}{\sqrt{1-{\rho_i}^2}}\rho_i d\rho_i \tag{B.6}$$

5) Interaction stress, summing the compressive stress exerted on fracture *i* by all of the hydraulic fractures in the array based on the details of the pressure distribution inside each HF Peirce and Detournay (2008). Let $\sigma_{j,i}$ represent the interaction stress fracture j performs on fracture i. Quantifying this interaction stress generally requires calculation from a 3D elasticity solver. Later we will describe a method for its approximation; for now we represent the interaction stress in a generic form given by

$$\sigma_{I(i)} = \sum_{j=1}^{N, j\neq i} \sigma_{j,i} \tag{B.7}$$

6) Constraints on the inlet fluid pressures and sum of the fluid fluxes at the fracture inlets. These impose that the inlet pressures are the same (tied together by the wellbore assuming zero pressure loss due to fluid flow through the wellbore) and the fluid fluxes sum to the total injection rate Q_o, i.e. volume balance is satisfied for the wellbore. Hence,

$$p_{f(1)}(R_w,t) = p_{f(2)}(R_w,t) = \cdots = p_{f(N)}(R_w,t), \qquad \sum_{i=1}^{N} Q_i(t) = Q_o \tag{B.8}$$

R_w is the wellbore radius to represent the inlet.

This system of 6N equations is thus comprised of 4*N* field equations, 1*N* moving boundary equations (the propagation condition), and 1*N* conditions governing the transient values of the influxes to each fracture. This system is completed by the initial conditions (*t=0*)

$$R_i=0,\ w_i=0,\ q_i=0 \text{ and } p_{f(i)}=0\ , \tag{B.9}$$

boundary conditions at the crack tip given by Detournay and Peirce (2014); Detournay (2004)

$$w_i(R_i,t)=0,\ q_i(R_i,t)=0\ , \tag{B.10}$$

and the inlet boundary condition

$$2\pi r q_i(r,t) = Q_i \text{ at } r \to 0 \tag{B.11}$$

The problem, then, consists of solving this system of governing equations in order to find the 6*N* unknown quantities, $w_i(r,t)$, $p_{f(i)}(r,t)$, $\sigma_{I(i)}(r,t)$, $q_i(r,t)$, $R_i(t)$ and $Q_i(t)$ as a function of the given quantities Q_o, C_L, μ', K', E' ,R_w, N, h_k, and t.

B. Approximation

As with the exact system of governing equations, the approximations entails coupling of six basic parts. Additionally, a seventh part is introduced in order to update a pressure estimate in order to be less prone to error. These seven parts are as follows:

1. Pressure Distribution Approximation

Taking on a functional form consistent with the asymptotic behavior of the pressure expected near both the inlet and leading edge of the hydraulic fracture. Assuming a functional form of the pressure distribution drastically decreases computational intensity by removing the need to carry calculate the distribution at each time step based on, say, a finite difference discretization of the governing equations of fluid flow Peirce and Detournay (2008). However, a suitably accurate estimate cannot be obtained with an arbitrary functional form. Here we select the form of the fluid pressure expressed as

$$p_{f(i)}(\rho_i, t) = \left(\frac{\mu_i^c(t) E'^2}{t}\right)^{\frac{1}{3}} \Pi_i(\rho_i, t) + \sigma_o, \quad \rho_i = r/R_i(t) \tag{B.12}$$

where the dimensionless pressure distribution $\Pi_i(\rho_i, t)$ is given as:

$$\Pi_i(\rho_i, t) \cong A\left[\omega - \frac{2}{3(1-\rho_i)^{\frac{1}{3}}}\right] - B\left(ln\frac{\rho_i}{2} + 1\right) + \psi_i(t), \qquad \omega \approx 2.479 \tag{B.13}$$

$$A = 0.3581 \text{ and } B = 0.09269$$

This functional form entails expressing the pressure as a superposition of: 1) a pressure that is singular like the distance from the tip to the -1/3 power Spence and Sharp (1985), 2) a pressure that is logarithmically singular at the inlet, and 3) one part of the pressure is spatially uniform. The tip singularity embodies the asymptotic form simultaneously satisfying Poiseuille flow, continuity, and elasticity Desroches et al. (1994), while the inlet singularity follows directly from the combination of Poiseuille flow and the inlet flow boundary condition (**Equation B.11**). The spatially-uniform part $\psi_i(t)$ is inspired by the zero-order solution given in large-toughness Savitski and Detournay (2002) in order to account for the toughness, expressed in **Section S2.2**.

The novelty introduced by this method is to allow $\mu_i^c(t)$ to be a degree of freedom, chosen as a part of satisfying the equations described in the rest of this section. We find that this quantity varies in such a way that it embodies additional energy dissipation associated with leak-off and toughness, and hence we call this quantity a "composite viscosity" because it acts like a viscosity, but it is a composite dissipation parameter accounting for more than just the fluid viscosity.

2. Toughness

The propagation condition is given by $K_I = K_{IC}$ where K_I is computed by the traction $T_i(\rho_i, t)$ **Equation B.4** is substituted into the **Equation B.6,** we get:

$$K_I = 2\sqrt{\frac{R_i(t)}{\pi}} \int_0^1 \frac{1}{\sqrt{1-{\rho_i}^2}} \left\{ \left(\frac{E'^2 \mu_i^c(t)}{t} \right)^{\frac{1}{3}} \Pi_i(\rho_i, t) - \sum_{j=1}^{N, j\neq i} \sigma_{j,i} \right\} \rho_i d\rho_i \tag{B.14}$$

It is readily shown Savitski and Detournay (2002) that the first two terms on the RHS in **Equation B.13** are associated with zero contribution to K_I, i.e. they integrate to zero when substituated into **Equation B.14**. Thus it remains only the spatially uniform pressure $\psi_i(t)$, which must then be chosen so as to ensure satisfaction of $K_I = K_{IC}$ at all times. By substitution, $\psi_i(t)$ is solved as:

$$\psi_i(t) = \left(\frac{K_I}{2\sqrt{\frac{R_i(t)}{\pi}}} + \int_0^1 \frac{\sum_{j=1}^{N, j\neq i} \sigma_{j,i}\, \rho_i}{\sqrt{1-{\rho_i}^2}} d\rho_i \right) \Big/ \left(\frac{E'^2 \mu_i^c(t)}{t} \right)^{\frac{1}{3}} \tag{B.15}$$

Hence, using this expression in **Equation B.13** provides a pressure distribution that implicitly satisfies propagation at all times. This allows the composite viscosity to be a degree of freedom to be solved for at each time step, as later described. The novelty is also highlighted here as: although a new governing equation given by fracture propagation is added, the quantity of the variables which need to participate in the iteration is unchanged by forcing the $\mu_i^c(t)$ to be toughness

responsible through the explicitly solved $\psi_i(t)$. Again we recall that $\sigma_{j,i}$ in **Equation B.15** denotes the interaction stress performed by the neighboring fractures *j* loading on fracture *i* approximated as described in the next point.

3. Interaction Stress Approximation

Using an equal volume, uniformly-pressurized crack. The full elasticity solution accounting for the non-uniform and transient pressure within each growing fracture is a major source of computational expense. To enable rapid computation, an approximation has been proposed by Cheng and Bunger (2019a), where the non-uniform pressure is replaced by a uniform pressure, choosing this uniform pressure for each HF at each time step so as to generate a fracture with the same volume as the actual HF being opened by a non-uniform internal pressure, that is:

$$P_j = \frac{3}{16}\frac{E'V_j}{{R_j}^3} \quad V_j = 2\pi\int_0^{R_j(t)} w_j(r,t)rdr \tag{B.16}$$

where P_j is the adjusted uniform internal net pressure for the j^{th} hydraulic fracture resulting from uniformly-pressurized ellipsoidal crack. Then, according to the solution of Sneddon (1946), the normal component of the stress performed by neighboring crack *j* on crack *i* is approximated as

$$\sigma_{j.i} = \frac{2P_j}{\pi}\left\{\delta_{j,i}{}^{-\frac{1}{2}}cos\frac{1}{2}\varphi_{j,i} - tan^{-1}\frac{\delta_{j,i}{}^{\frac{1}{2}}sin\frac{1}{2}\varphi_{j,i} + \tau_{j,i}sin\theta_{j,i}}{\delta_{j,i}{}^{\frac{1}{2}}cos\frac{1}{2}\varphi_{j,i} + \tau_{j,i}cos\theta_{j,i}}\right.$$
$$\left. + \zeta_{j,i}\delta_{j,i}{}^{-\frac{3}{2}}cos\left(\frac{3}{2}\varphi_{j,i} - \theta_{j,i}\right) - \zeta_{j,i}\delta_{j,i}{}^{-\frac{1}{2}}sin\frac{1}{2}\varphi_{j,i}\right\} \tag{B.17}$$

where

$$\tau_{j,i} = \left(1 + \zeta_{j,i}^2\right)^{\frac{1}{2}} \quad \delta_{j,i} = \left\{\left[\left(\rho_i \frac{R_i}{R_j}\right)^2 + \zeta_{j,i}^2 - 1\right]^2 + 4\zeta_{j,i}^2\right\}^{\frac{1}{2}}$$
$$\theta_{j,i} = arctan\left(\frac{1}{\zeta_{j,i}}\right) \quad \varphi_{j,i} = arccot\left\{\left[\left(\rho_i \frac{R_i}{R_j}\right)^2 + \zeta_{j,i}^2 - 1\right]/2\zeta_{j,i}\right\} \tag{B.18}$$

Here $\zeta_{j,i}$ is the ratio of spacing $h_{j,i}$ (between fracture *i* and *j*) to the crack radius R_j, and recall that ρ_i is the ratio of radial position *r* to fracture radius R_i, $\rho_i = \frac{r}{R_i}$. Note that the $\zeta_{j,i}$ value decreases as the fracture grows, that is, as R_i increases for each fracture.

4. Elasticity

The local crack opening $w_i(\rho_i, t)$ appearing in volume balance (**Equation B.22**), which also includes the inlet opening used in the inlet boundary conditions (**Equation B.21**), is determined by elasticity through **Equation B.3** with $T_i(\rho, t)$ as the traction acting across the surfaces of the i^{th} crack given by

$$T_i(\rho_i, \mu_i^c(t), \psi_i(t)) =$$
$$\left(\frac{E'^2 \mu_i^c(t)}{t}\right)^{\frac{1}{3}} \left\{A\left[\omega - \frac{2}{3(1-\rho_i)^{\frac{1}{3}}}\right] - B\left(ln\frac{\rho_i}{2} + 1\right) + \psi_i(t)\right\} \tag{B.19}$$

According to the elasticity, the $w_i(\rho_i, t)$ is simultaneously determined by the radius R_i. It is convenient to express the radius as the product of a dimensionless radius $\gamma_i(t)$. This quantity is an unknown found via solution to the system of approximate equation, and a characteristic radius, with a form that follows from the solution of Savitski and Detournay (2002), given by

$$R_i(t) = \gamma_i(t)\left(\left(\frac{E't}{\mu_i^c(t)}\right)^{1/3}\int_0^t Q_i(t)dt\right)^{1/3} \tag{B.20}$$

Using this scaling of the radius aids the solution method because it enables searching for roots of the γ_i, which are around one, rather than searching for roots of R_i, for which it is more difficult to obtain a suitable initial guess. This improvement of the initial guess using a scaling-type relationship enables more rapid convergence of the solution algorithm and avoids spurious convergence in the event that R_i has multiple non-physical roots.

Having introduced all the required variable to calculate the $w_i(\rho_i, t)$ though non-local elasticity relationship, the width at inlet $w_i(0, t)$ is therefore solved. Furthermore, the functional form of the pressure that appropriately captures the asymptotic form at the inlet has been already expressed in **Equation B.12**. We substitute the pressure into the Poiseuille **Equation B.5**, keeping the leading order term near the inlet arising from the logarithmic singularity of the pressure. By doing this, we obtain another crack opening derived from Poiseuille Law. In turn, a constraint is obtained from the inlet boundary condition (**Equation B.11**), namely

$$w_i(0,t) - \left(\frac{Q_i(t)\mu'}{2\pi B\left(\frac{\mu_i^c(t)E'^2}{t}\right)^{\frac{1}{3}}}\right)^{\frac{1}{3}} = 0 \tag{B.21}$$

5. Global Volume Balance

Providing a weak form approximation to the local volume balance accounted for by the complete model (**Equation B.2**). By integration of the local volume balance (**Equation B.2**) subject to the inlet and tip boundary conditions (**Equations B.9** and **B.10**), we arrive to the global volume balance equation

$$2\pi \int_0^{R_i(t)} w_i(r, \mu_i^c(t), \psi_i(t)) r dr + 4\pi C_L' t^{1/2} \int_0^{R_i(t)} \sqrt{1-(r/R_i(t))^{\alpha_i}}\, r dr = \int_0^t Q_i(t) dt \tag{B.22}$$

where C_L'=$2C_L$. Note that for the purpose of enabling rapid calculation of the fluid leakoff, we do not explicitly use the evolving radius but instead approximate its history, $R_i(t) = At^{1/\alpha_i}$. This does not imply the fractures are restricted to follow power law growth – their radii are the result of the coupled solution. Rather, rapid calculation is facilitated by this approximation of the history dependence of the integral associated with the contact time $t_i(r)$ is replaced using

$$\left(\frac{r}{R_i(t)}\right)^{\alpha_i} = \frac{t_i(r)}{t}, \alpha_i = 1/(dlogR_i/d\log t) \tag{B.23}$$

6. Inlet Conditions

Given by the equality of the inlet pressures and the summation of the inlet fluxes to the total influx to the wellbore expressed in **Equation B.8**. Satisfying these conditions requires estimation of the inlet pressures. In a full solution these would be obtained from the computed fluid pressure distribution. In the present case we have approximated the fluid pressure distributions. Because the functional form has a singularity at the inlet (**Equation B.13**),

computing the inlet pressure would require prescribing a finite wellbore radius, thus introducing an often-spurious sensitivity of the solution to the wellbore radius and potential for substantial errors due to the large pressure gradient near the inlet. A more robust approach is to treat these inlet pressures as unknowns, prescribing them so as to be consistent with global energy balance. Such an approach is described in the point to follow.

7. Global Energy Balance

It is difficult to get an accurate estimate of the wellbore pressure due to a singularity in the pressure there. So, instead, the approximation computes the pressure at the wellbore so as to satisfy global energy balance, extended from the previous work by Bunger (2013); Lecampion and Detournay (2007) but adding the energy related to toughness into the energy balance. This modification is made in order to enable the new model C5Frac to be valid for all regimes including the so-called "toughness-dominated" regime. Note that detailed explanations of propagation regimes are available in a variety of past works and so will not be repeated here. Interested readers are referred to Detournay (2016). The updated power balance is given by:

$$p_{f(i)}(R_w, t)Q_i(t) = D_{c(i)} + D_{f(i)} + D_{L(i)} + \dot{U}_\iota - \dot{W}_{I(i)} - \dot{W}_{o(i)} + P_{perf(i)} \tag{B.24}$$

Here the left-hand side is the rate of energy input (product of the pressure and inflow rate) to the i^{th} fracture. The six terms on the right-hand side are, respectively:

D_c is the dissipation rate associated with rock breakage, taken here as the limiting case of zero toughness, i.e.

$$D_{c(i)} = \frac{\pi^2}{16}\frac{K'^2 R}{E'}\frac{dR}{dt} \tag{B.25}$$

D_f is the dissipation rate associated with viscous fluid flow given by

$$D_{f,p(i)} = \frac{\pi}{\mu'} \int_{R_w}^{R_i} {w_i}^3 \left(\frac{\partial p_{f(i)}}{\partial r} \right)^2 r dr \tag{B.26}$$

D_L is the fluid loss rate associated with leak-off given by

$$D_{L(i)} = 4\pi \frac{\sigma_o C_L R_i^2}{t^{1/2}} \int_0^1 \frac{\rho_i}{\sqrt{\sqrt{1-{\rho_i}^{\alpha_i}}}} d\rho_i \tag{B.27}$$

U is a portion that goes into increasing the strain energy by deforming the rock strain energy – this is the recoverable elastic energy.

$$\dot{U}_i = \pi \int_{R_w}^{R_i} \left(T_i \frac{\partial w_i}{\partial t} + w_i \frac{\partial T_i}{\partial t} \right) r dr \tag{B.28}$$

W_I is the work done on each HF by the compressive stresses induced by its neighbors – again the hydraulic input power must be sufficient to overcome this negative work. Hence

$$\dot{W}_{I(i)} = -2\pi \left(\int_{R_w}^{\min(R_i R_j)} \sigma_{I(i)} \frac{\partial w_j}{\partial t} r dr + \sigma_{I(i)} \frac{dR_i}{dt} R_i w_j \left(\frac{R_i}{R_j} \right) \right) \tag{B.29}$$

W_o is the work on the crack by the in-situ stress – the hydraulic input power must be sufficient to overcome this negative work. To account for the fluid loss, the work by in-situ stress W_o is modified as

$$\dot{W}_{o(i)} = -\sigma_o (1 \pm S_i) \left(Q_i - 4\pi \frac{C_L R_i^2}{t^{1/2}} \int_0^1 \frac{\rho_i}{\sqrt{\sqrt{1-{\rho_i}^{\alpha_i}}}} d\rho_i \right) \tag{B.30}$$

The variable S_i is designed to quantify the non-uniform in-situ stress.

P_{perf} is the power loss through the entry point Bunger et al. (2014). Accounting for perforation loss makes use of the analysis of the pressure drop as fluid flows through a cluster of n perforation holes Crump and Conway (1988); Economides and Nolte (2000).

$$P_{perf(i)} = \left(\frac{a\rho}{n_i^2 D_{p(i)}^4 C^2}\right) Q_i(t)^3 \tag{B.31}$$

The i^{th} cluster has n_i perforations; usually this value is within the range of 5 to 20, and it ideally should be the number of holes that actually accommodate the fluid flow into the hydraulic fracture, not just the total number placed (some of which may be plugged or otherwise ineffective). Here

$$D_{c(i)}$$

$$= \frac{\pi^2}{16}\gamma_i(t)\frac{K'^2}{E'^{\frac{8}{9}}}\left(\left(\frac{t}{\mu_i^c(t)}\right)^{\frac{1}{3}}\int_0^t Q_i(t)dt\right)^{\frac{1}{3}}\frac{d}{dt}\left(\gamma_i(t)\left(\left(\frac{E't}{\mu_i^c(t)}\right)^{1/3}\int_0^t Q_i(t)dt\right)^{1/3}\right) \tag{B.32}$$

$$D_{f,p(i)}$$

$$= \pi\left(\frac{\mu_i^c(t)E'^2}{t}\right)^{\frac{2}{3}}\int_0^1 w_i\left(\rho_i, Q_i(t), \gamma_i(t), \mu_i^c(t)\right)^3\left[\left(\frac{\partial \Pi_{f(i)}(\rho_i,t)}{\partial \rho_i}\right)^2 - \left(\frac{B}{\rho_i}\right)^2\right]\rho_i d\rho_i \tag{B.33}$$

$$+ \pi\left(\frac{\mu_i^c(t)E'^2}{t}\right)^{\frac{2}{3}}\int_{R_w/R}^1 w_i(0,t)^3\left(\frac{B}{\rho_i}\right)^2\rho_i d\rho_i$$

$$D_{L(i)} = 4\pi\frac{\sigma_c C_L \gamma_i^2(t)}{t^{1/2}}\left(\left(\frac{E't}{\mu_i^c(t)}\right)^{1/3}\int_0^t Q_i(t)dt\right)^{2/3}\int_0^1 \frac{\rho_i}{\sqrt{\sqrt{1-{\rho_i}^{\alpha_i}}}}d\rho_i \tag{B.34}$$

$$\dot{U}_\iota$$

$$= \sum_{j=1}^{N, j\neq i}\left(-\frac{2}{9}\right)\pi\gamma_i(t)^2\left(\frac{\mu_i^c(t)E'^8}{t}\right)^{\frac{1}{9}}\left(\int_0^t Q_i(t)dt\right)^{\frac{2}{3}}\int_0^1 w_i(\rho_i,t)\Pi_{net(i)}(\rho_i,t)\rho d\rho \tag{B.35}$$

$$\dot{W}_{I(i)} = -\sum_{j=1}^{N,j\neq i}\left\{\begin{array}{c} 2\pi min\{R_i,R_j\}^2 \\ \int_0^{min\left\{\frac{R_i}{R_j},1\right\}} \sigma_{I(i)}\left(\rho_i \frac{R_i}{R_{j,}}\, t\right)\frac{dw_j}{dt}\rho_j d\rho_j \\ +2\pi R_i \frac{dR_i}{dt}\sigma_{I(i)}(1,t)w_j\left(\frac{R_i}{R_j},t\right) \end{array}\right\} \quad \text{(B.36)}$$

$$\dot{W}_{o(i)} = -\sigma_o(1\pm S_i)[\langle Q_i(t)\rangle - \frac{4\pi C_L \gamma_i^2(t)}{t^{\frac{1}{2}}}\left(\left(\frac{E't}{\mu_i^c(t)}\right)^{\frac{1}{3}}\int_0^t Q_i(t)dt\right)^{\frac{2}{3}}\int_0^1 \frac{\rho_i}{\sqrt{\sqrt{1-{\rho_i}^{\alpha_i}}}}d\rho_i] \quad \text{(B.37)}$$

also $D_{p(i)}$ represents the perforation diameter of i^{th} cluster, which is usually within a range from 6 to 15 mm (about ¼ to 5/8 inches). As before, $Q_i(t)$ represents the injection rate to the i^{th} fracture, which will vary with the pumping time *t*. There is also a shape factor for the perforation tunnels themselves, given here by *C* which is typically taken as 0.56 before erosion (sharp perforation) and 0.89 after erosion based on the experimental results of Crump and Conway (1988). In C5Frac, perforation erosion is neglected so *C* is taken as a constant equal to 0.56. The numerical factor, *a*, is usually taken from Crump and Conway (1988) as 0.8106. The fluid injected into the reservoir has a fluid density of ρ. Taken together, the bracketed quantities in **Equation B.31** comprise a coefficient of proportionality between the power loss associated with flow through the perforations and the cube of the flow rate.

Upon substitution of the unknowns μ_i^c and γ_i with their implicit dependence on $Q_i$via the solutions pressure, width, and radius expressions, we obtain **Equation B.32-S37**.

C. Algorithm

By introducing function forms ensuring implicit satisfaction of some governing equations, we have replaced the need to solve for $6N$ unknowns ($w_i, p_{f(i)}, \sigma_{I(i)}, q_i,\ R_i$ and Q_i) with $3N$ unknowns (γ_i, μ_i^c and Q_i) satisfying $3N$ implicitly interaction-dependent equations obtained from global volume balance (**Equation B.22**), wellbore width equality (**Equation B.21**), equality of wellbore pressures (**Equation B.24**), and summation of inlet fluxes to the total pumping rate (**Equation B.8**). Hence, the solution method satisfies

$$\left\{\begin{array}{c} 2\pi\gamma_i(t)^2\left(\dfrac{E't}{\mu_i^c(t)}\right)^{2/9}\displaystyle\int_0^1 w_i(\rho_i,\mu_i^c(t))\rho_i d\rho_i + \\ 4\pi C_L t^{\frac{13}{18}}\gamma_i(t)^2\left(\dfrac{E'}{\mu_i^c(t)}\right)^{\frac{2}{9}}\displaystyle\int_0^1\sqrt{1-\rho_i{}^{\alpha_i}}\rho d\rho \\ = \left(\displaystyle\int_0^t Q_i(t)dt\right)^{\frac{1}{3}} \\ \gamma_i(t)\mathcal{F}\{0,T_i(\rho_i,\mu_i^c(t),t)\}\left(\displaystyle\int_0^t Q_i(t)dt\right)^{\frac{1}{3}} \\ = \left(\dfrac{\pi^2 Q_i(t)\mu' E'^2}{2^7 B}\right)^{\frac{1}{3}} \\ p_{f(1)}(R_w,t) = p_{f(2)}(R_w,t) = \cdots = p_{f(N)}(R_w,t) \\ \displaystyle\sum_{i=1}^{N} Q_i(t) = Q_o \end{array}\right\} \xrightarrow{yields} \begin{Bmatrix}\mu_i^c(t)\\ \gamma_i(t)\\ Q_i(t)\end{Bmatrix} \tag{B.38}$$

Recall that $w_i(\rho_i,\mu_i^c(t))$ is obtained from elasticity (**Equation B.3**), wherein the pressure distribution is given by **Equation B.19**. Additionally, as previously mentioned, the $p_{f(i)}(R_w,t)$ are obtained from global energy balance (**Equation B.24**). The procedure for obtaining the approximate solution is as follows:

1.Define input parameters ($\sigma_c, C_L, E', \mu', K_I, Q_o, h_i$).

2.For the starter solution it is specified such that $Q_i(t_o) = Q_o/N$, where t_o is a specified initial time (well before leak-off and interaction become important). Additionally, based on the zero toughness, zero leak-off, zero interaction solution of Savitski and Detournay (2002), initially $\alpha_i(t_o) = 4/9$.

3.**Equations B.21** and **B.22** are then be solved using Newton's method.

4.After that, the power balance (**Equations B.32-S37**) is solved.

5.The iteration procedure is performed until the desired level of convergence of $Q_i(t)$ is reached, that is, $Q_i(t)$ no longer change by very much at each iteration. Once $Q_i(t)$ is obtained, the value of $\alpha_i(t)$ is updated according to $\alpha_i = 1/(dlogR_i/d\log t)$, which follows from the presumed power law growth of the radius.

6.Then the time step is advanced by Δt, noting that $Q_i(t)$ and $\alpha_i(t)$ can be used as the pre-guessed value for $Q_i(t + \Delta t)$ and $\alpha_i(t + \Delta t)$.

7.Repeat steps 3-6 until the desired total pumping time is achieved.

D. Validation

The accuracy of the new model will be examined through the validation to reference solution. In term of the restricted applicability owned by different reference solution. Single fracture cases will be validated at first, then multiple fractures with another reference solution obtained from a high-fidelity model.

1. Single Fracture

The reference solution is calculated by Dontsov (2016) by developing a numerical approximation for a penny-shaped hydraulic fracture. This solution captures the transition behavior of hydraulic fractures between negligible and large leak-off and between large viscosity and large toughness regimes. It is also accurate in capturing limiting behavior for toughness or viscosity dominated and leakoff or storage dominated hydraulic fractures. To better visualize the approximation, the validation is separated as two parts. First part is time variation for given parameters E'=9.5 GPa, K_{IC}=10^7 Pa·$m^{1/2}$, μ=0.001 Pa·s, Q_o=0.01 m^3/s. Additionally, the choice of the leak-off parameter is C_L ={10^{-5} m/$s^{1/2}$, 10^{-4} m/$s^{1/2}$, 10^{-3} m/$s^{1/2}$}. As can be seen from **Figure B1**, all quantities match the reference solution within one percent. The only exception is oscillatory behavior in the efficiency for large values of C_L; but here the oscillatory behavior is in the reference solution, not our approximate solution. This comparison uses relatively large toughness and can be shown to correspond to the toughness dominated and near-toughness dominated transition regimes

.

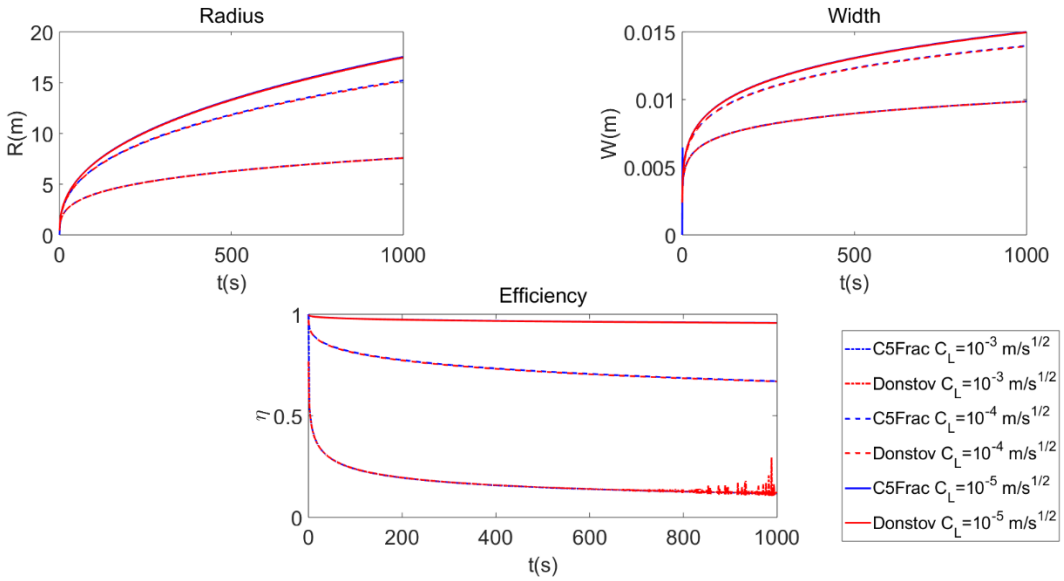

Figure B1: Single fracture validation at large toughness. Comparison between the approximation solution (blue line) and the reference solution (red line) in terms of time histories of: fracture radius, width at the wellbore (ρ =0) and efficiency. Dotted, dashed and solid lines indicate the CL ={10-3 m/s1/2, 10-4 m/s1/2, 10-5 m/s1/2} respectively. See online version of the article for full color.

To further check the accuracy of the approximate solution, smaller toughness is also used and parameters are set as E'=9.5 GPa, K_{IC}=1000 Pa·m$^{1/2}$, μ=1 Pa·s, Q_o=0.1 m^3/s. Additionally, the choice of the leak-off parameter is C_L ={10^{-5} m/s$^{1/2}$, 10^{-4} m/s$^{1/2}$, 10^{-3} m/s$^{1/2}$}. Similar to the large toughness cases shown in **Figure B1**, the accuracy of all quantities is under a 1%. as can be seen from **Figure B2**.

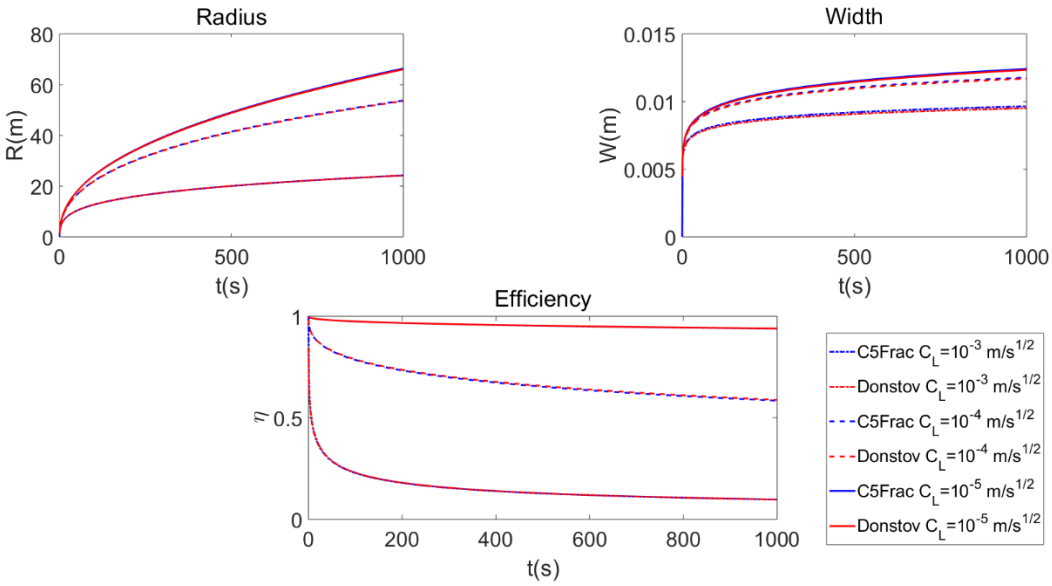

Figure B2: Single fracture validation at small toughness. Comparison between the approximation solution (blue line) and the reference solution (red line) in terms of time histories of: fracture radius, width at the wellbore (ρ =0) and efficiency. Dotted, dashed and solid lines indicate the CL ={10-3 m/s1/2, 10-4 m/s1/2, 10-5 m/s1/2} respectively. See online version of the article for full color.

To further quantify the level of accuracy of the approximation, a relative error is defined as

$$\text{Err} = \sqrt{\left[\frac{x_{ref} - x_{apr}}{x_{ref}}\right]^2} \tag{B.39}$$

where subscripts ‘ref’ and ‘apr’ correspond to the reference and approximation solution respectively. Here the variable x can be radius R, efficiency η, or wellbore width W.

To demonstrate the accuracy, which is affected by several parameters, it is important to note that the error is demonstrated verses the dimensionless time $log_{10}(\tau)$ and leak-off parameter $log_{10}(\Phi)$, given as (after Donstov (2016))

$$\Phi = \frac{\mu'^3 E'^{11} C_L'^4 Q_o}{K'^{14}} \tag{B.40}$$

$$\tau = \left(\frac{K'^{18} t^2}{E'^{13} \mu'^5 Q_o^3} \right)^{1/2} \tag{B.41}$$

These dimensionless quantities can be used to characterize a globally-defined propagation regime for each fracture, as detailed by Dontsov (2016). The regimes validity zones are denoted in **Figures B3-B5** as:

- *M (Viscosity-Storage)* regime, corresponding to viscous dissipation far exceeding dissipation associated with the fracture toughness, and negligible fluid leakoff rate compared to the rate of change of the fracture opening (width).
- *K (Toughness-Storage)* regime, corresponding to negligible dissipation associated with fluid flow as well as negligible leakoff rate.
- $\widetilde{M}$ *(Viscosity-Leakoff)* regime, corresponding to dominant viscous dissipation and large fluid leakoff velocity compared to the rate of change of the fracture width.
- $\widetilde{K}$ *(Toughness-Leakoff)* regime, corresponding to negligible fluid viscosity and large fluid leakoff rate.

To visualize the propagation regimes, **Figures B3-B4** plot the validity zones corresponding to the limiting asymptotic solutions corresponding to each of these limiting regimes. The transitions between the regimes are where numerical solutions are needed, in general, or some other suitable approximations (as provided e.g. by Dontsov (2016)).

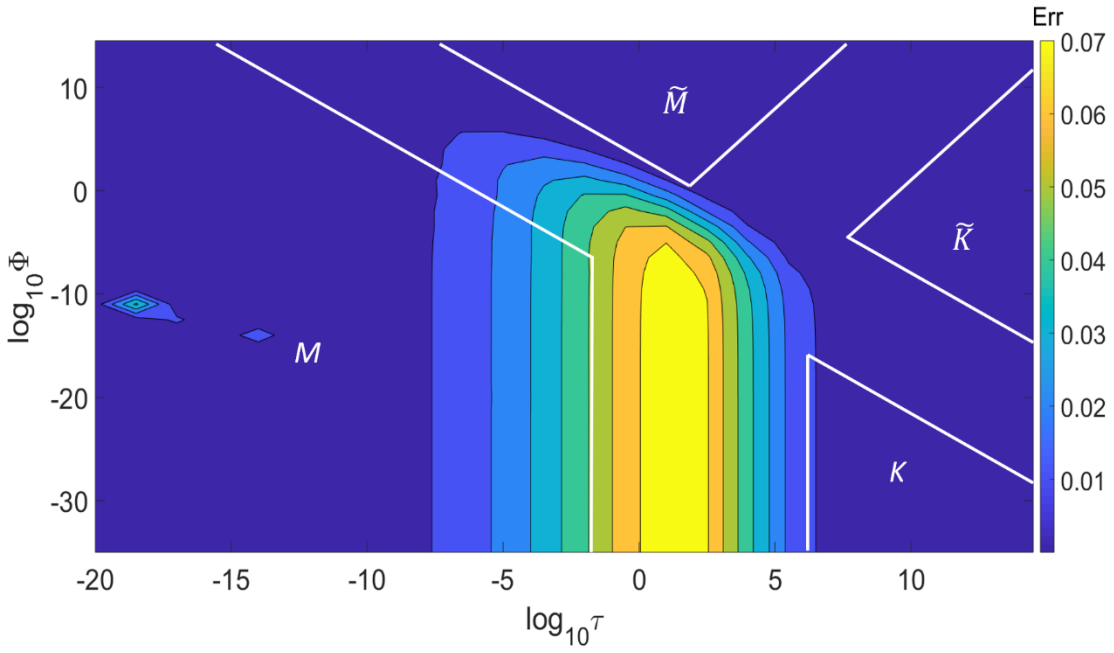

Figure B3: Test accuracy for radius. Relative error associated with the approximate fracture length (radius) solution R versus dimensionless time τ and leak-off parameter Φ. M, K, $\widetilde{M}$ and $\widetilde{K}$ regions indicate, respectively, validity zones of the M vertex solution, K vertex solution, $\widetilde{M}$ vertex solution and $\widetilde{K}$ vertex solution Dontsov (2016), according to Dontsov (2016). White lines indicate boundaries of applicability of the vertex solutions.

As **Figure B3** shows, the relative error in the radius prediction compared to the reference solution is less than 1% in most regions, but it rises to a maximum of around 7% in the small leakoff transition between the viscosity and toughness dominated regimes. Similarly, **Figure B4** shows that the relative error on fracture width (i.e. crack opening) in most regions is below 1%, but with more significant mismatch (up to 20%) in the large leakoff transition between the viscosity and toughness dominated regimes. Note that this particular region will often be of little relevance; for the combination of parameters used here, this range was obtained for leakoff

coefficient C_L is bigger than 10^4 m/s$^{1/2}$, which can be compared to a practical range from 10^{-4} to 10^{-5} m/s$^{1/2}$. Such a large value of C_L leads to a 10^{-5}m crack opening and 10^{-11} efficiency, which means that a tiny absolute difference between the approximation and reference solution will result in a large relative difference. That is why there is a 20% difference shown in **Figure B4** and **B5**. Otherwise, the match is very good and the approximation is shown to suitably replicate the correct radius, width, and efficiency across all relevant ranges of parameter values.

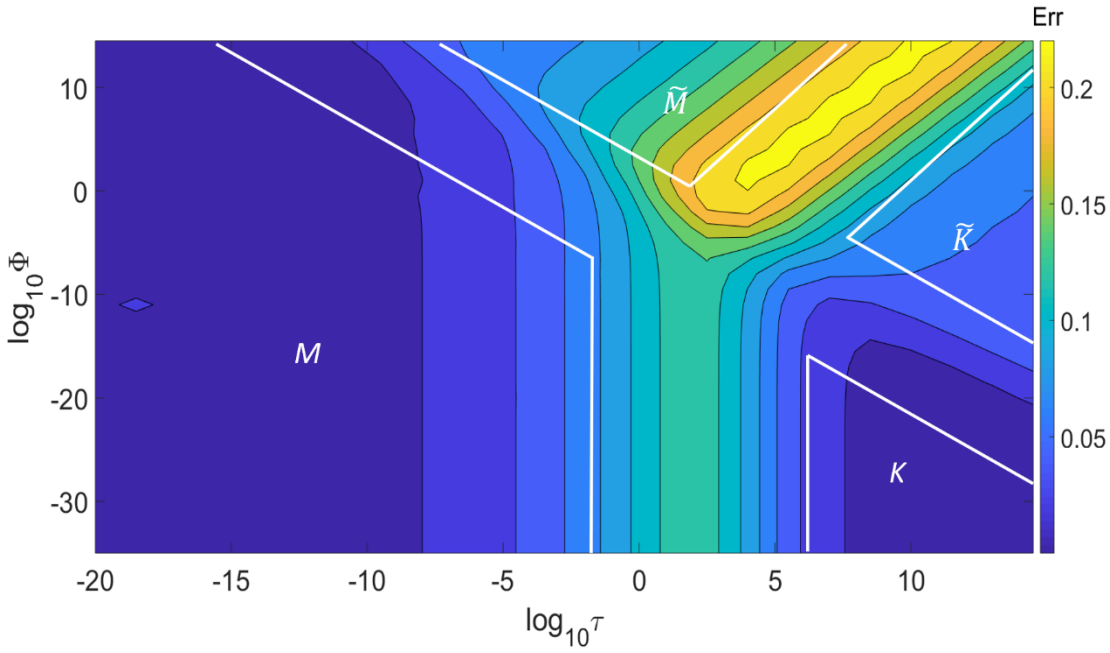

Figure B4: Test accuracy for width. Relative error between approximate and reference solutions for crack opening at inlet W. These are shown as they vary with dimensionless time τ and leak-off parameter Φ. M, K, $\widetilde{M}$ and $\widetilde{K}$ regions indicate, respectively, validity zones of the M vertex solution, K vertex solution, $\widetilde{M}$ vertex solution and $\widetilde{K}$ vertex solution Dontsov (2016), according to Dontsov (2016). White lines indicate boundaries of applicability of the vertex solutions.

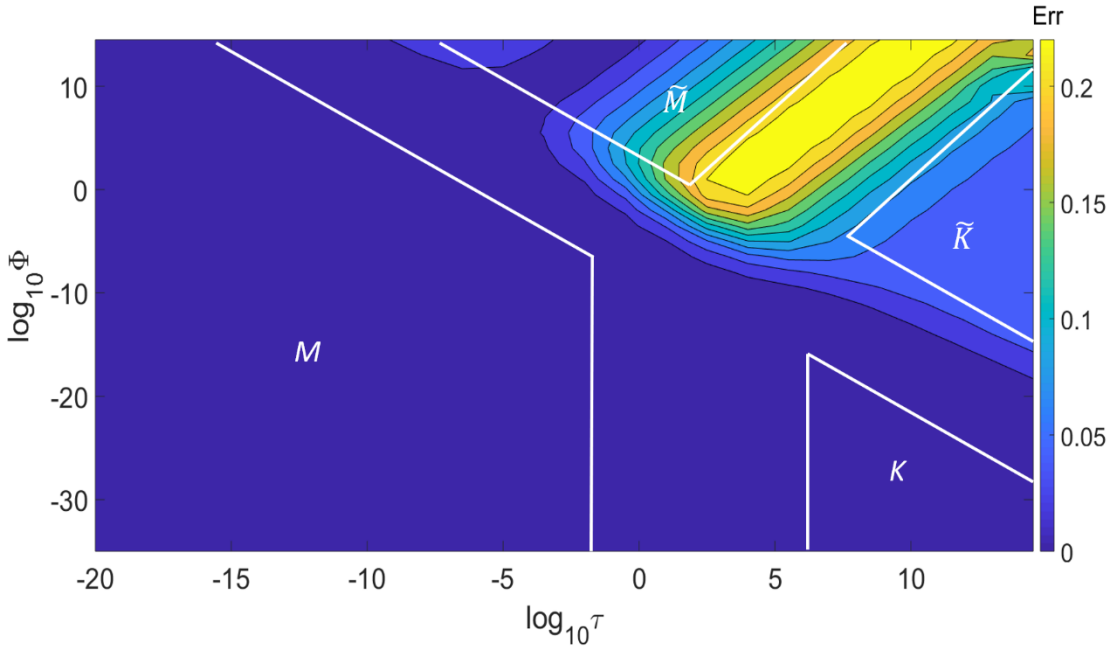

Figure B5: Test accuracy for efficiency. Relative error between approximate and reference solutions for efficiency η. These are shown as they vary with dimensionless time τ and leak-off parameter Φ. M, K, $\widetilde{M}$ and $\widetilde{K}$ regions indicate, respectively, validity zones of the M vertex solution, K vertex solution, $\widetilde{M}$ vertex solution and $\widetilde{K}$ vertex solution Dontsov (2016), according to Dontsov (2016). White lines indicate boundaries of applicability of the vertex solutions.

2. Multiple Fractures

Having demonstrated accuracy for single fracture growth relative to a single fracture reference solution, the level of accuracy of the developed approximation for multiple fractures will be quantified relative to reference solutions from a high-fidelity hydraulic fracture simulator. The high fidelity model used here is a fully coupled simulator called ILSA II Peirce and Bunger (2015),

which is extended for multiple, parallel planar hydraulic fractures based on the Implicit Level Set Algorithm, or "ILSA" Peirce and Detournay (2008). The key novelty of ILSA that makes it suitable as a benchmark simulator for our purposes is its enabling accurate solutions on very coarse meshes by embedding appropriate tip asymptotic behavior and then tracking moving boundary using a level set method that projects the front location based on these known asymptotics. This allows it to overcome common challenges in hydraulic fracture simulation of mesh sensitivity and time step limiting stability criteria, both of which can lead to either inaccurate solutions or large computational times. In ILSA, the elasticity equation is solved using a 3D displacement discontinuity method Crouch and Starfield (1983) and fluid flow is solved locally using the Finite Volume method. We benchmark and illustrate the use of the model considering cases with 5 HFs. The fractures are placed symmetrically relative to the middle fracture. Hence the "outer" fractures, 1 and 5, are identical. So also the "inner" fractures, 2 and 4, are identical. Fracture 3 always occupies the center of the array and will henceforth be called the "middle" fracture. The following parameter set is used for both the C5Frac and ILSA II simulations:

$$C_L = 0 \text{ m/s}^{1/2}, E = 9.5 \text{ GPa}, \nu = 0.2$$

$$\sigma_o = 70 \text{ Mpa}, R_W = 0.2 \text{ m}$$

To better understand the effect of toughness, two benchmarking cases considering uniform and non-uniform spacing between the fractures are chosen. One case is μ=1 Pa·s, K_{IC}=0 MPa·m$^{1/2}$, Qo=0.1 m^3/s, Z=20 m. Another case is μ=0.001 Pa·s, K_{IC}=1.5 MPa·m$^{1/2}$ Qo=0.0265 m^3/s, Z=120 m. For each case, we present comparisons of the time evolution of fracture radius, fluid influx to each fracture, fracture opening at the center, and total fracture area. Specifically, **Figure B6** is the case where the fractures are uniformly spaced so that h_1 = 30 m, the stage length z is 120m, so the fracture planes have z coordinates z_1=0, z_2=30, z_3=60, z_4=90, and z_5=120. In **Figure B7,** we

introduce a modification to the uniform array in which fractures 2 and 4 are moved, and also stage length is changed to be z=20m, so that h_1=3.6, corresponding to fracture planes having z coordinates z_1=0, z_2=3.6, z_3=10, z_4=16.4, and z_5=20. The results presented include: a) The dimensionless radius $R_i(t)/Z$, b) the inflow rate $q_i(R_w, t)$, c) the crack aperture at inlet $w_i(R_w, t)$, and d) total fracture area defined as

$$A(t) = \sum_{i=1}^{N-1} {R_i}^2(t)\,\pi \tag{B.42}$$

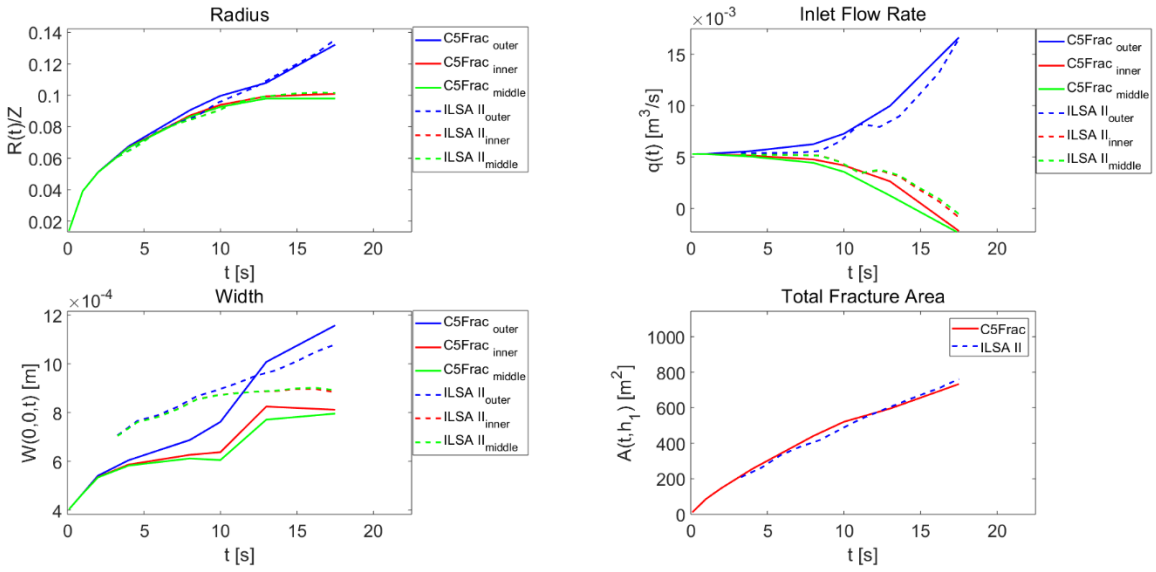

Figure B6: Multiple fractures validation at large toughness. C5Frac compared with ILSA II for a uniform array with $h_1 = h_2 = h_3 = h_4 = 30$m.

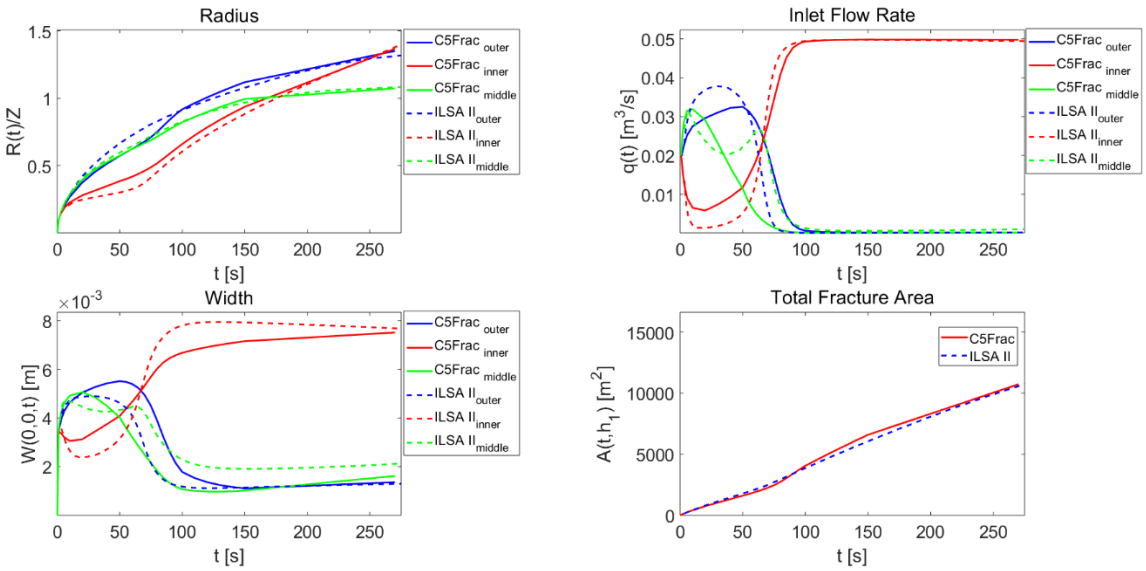

Figure B7: Multiple fractures validation at small toughness. C5Frac compared with ILSA II for non-uniform array with $h_1 = h_4 = 3.6\text{m}$ and $h_2 = h_3 = 6.4\text{m}$.

Overall, the ability of C5Frac to approximate ILSA II is good, most notably for our purposes because typically fracture area computed by C5Frac remains within 5% relative to the ILSA II. This quantity is naturally the most important when optimization is to be carried out on the created fracture area. The inlet flux and radius also approximated reasonably, with several observation that can be made. Firstly, we observe the stress-shadowing phenomenon, in which outer fractures grow preferentially while growth of the inner fractures is stunted instead of uniform growth. This is strongly evidenced in the uniform spacing case (**Figure B6**), where the inflow to the outer fracture increases sharply to $0.013\text{m}^3/\text{s}$ and consumes nearly all the total injection rate after 15 seconds. The localization of growth in the outer fractures is understandable because they have no constraint like the previous stage effect on their growth from outside the array. At the same time, flow rate to the other fractures decreases to approach zero. This is understood because

the interior fractures have to compete with one another in an induced compressive stress field that is established by the outer fractures and enhanced by any additional growth by the interior fractures. The localization to the outer fractures becomes more pronounced with time while growth of the inner fractures is minimal for uniform $h_1=30m$ case (see **Figure B6**).

In comparison to the uniform spacing cases, approximation is more difficult to obtain for the non-uniform spacing cases. The main reason is a complicated behavior associated with coupling among the fractures that has previously been called "squeeze out effect" Cheng and Bunger (2019a); Peirce and Bunger (2015); Cheng and Bunger (2019b). When this phenomenon occurs, the non-uniform growth plays a crucial role to promote a decreasing interaction work of initially suppressed fractures. Thus, fluid flow within the inner fractures becomes dominant, in this example, after 100s (**Figure B7**). At the same time, the swelling inner fractures induce a compressive force which has the effect of advancing the fracture by the displacing the fluid from the vicinity of the wellbore rather than by influx from the wellbore. The outer and middle fractures get a chance to grow after this reversal. In addition, more fractured area is achieved compared with the uniform spacing cases. This occurs, because the fracture growth becomes more uniform.

The accuracy has been demonstrated by suitable agreement between C5Frac and ILSA II in both uniform and non-uniform spacing cases. Furthermore, identifying the opportunities to reduce environmental footprint, which requires hundreds to thousands of model evaluations, is enabled by the calculation speed. To this point, an illustration of computation time for C2Frac Cheng and Bunger (2016), C3Frac Cheng and Bunger (2019a), and ILSA II Peirce and Bunger (2015) is presented in **Table B1**.

Table B1: Timing Comparison

Uniform Five	C2Frac	C3Frac	C5Frac	ILSA II
Computation Time	1.06 s	255 s	686 s	220612 s
Simulation Time & Steps	t=203 s 128 steps	t=203 s 128 steps	t=203 s 128 steps	t=203 s 128 steps
Processer & RAM	INTEL-i7 4770k 4.00 GHz. 32 GB RAM	INTEL-i7 4770k 4.00 GHz. 32 GB RAM	INTEL-i7 4770k 4.00 GHz. 32 GB RAM	INTEL-XEON E5649 2.53 GHz 96 GB RAM

C5Frac takes only minutes to compute a single multi-fracture result at typical reservoir length and time scales on a personal computer. Although this is much slower than C2Frac, which computes in a few seconds, and also twice slower than C3Frac, the benefit is the ability to simulate the leak-off and toughness (available only in C5Frac) effects. And most strikingly, the simulations are much faster than fully coupled simulations, which can take tens of hours and up to a week to compute on a similar computer. Note that the computation time of ILSA II for each time step continuously increases because the advancing front leads to an ever-increasing number of elements in the simulation, there is no such increase in computation time per model time step in C5Frac. So, in conclusion, because of the reasonable accuracy at high calculation speed, this new approximate simulator opens new possibilities to explore large parametric spaces, identifying combinations of parameters associated with high resource use efficiency (i.e. minimizing volume cost per recovery).

E. Results

1. Maximizing Area by High Resource Use Efficiency

In addition to minimizing injection volume, a larger recovery is also important to reduce the GHG emission per power produced. Here we will examine the ability to maximize fractured surface area via optimization that utilizes appropriate viscosity and non-uniform spacing in a complimentary way at same injection volume. In other words, we change the optimization from output constrained (fixed fracture area) to input constrained (fixed volume). For all cases, the generated fracture surface area is computed (**Figure B8**), and a comparison is then made between uniform and nonuniform cases via the ratio of areas, A_{non}/A_{uni}.

Note that here, same as the **Figures B3-B5**, we also borrow the Φ and τ to illustrate the regimes of multiple interacting fractures (**Figure IV.2** in main body, and **Figure B8**). Note that the flow rate used in Dontsov (2016) is for a single fracture. For multiple fractures, the injection rate to each fracture is different and time-dependent. Hence, we use the constant total injection rate Q_O to calculate the nominal global value of Φ and τ, also accounting for that the area plotted is a summation value from all fractures. As a result, although the Φ and τ are not exactly as same as defined in Dontsov (2016), it is still useful to use **Figure B8** as a guide to regimes in which leak-off, rock fracture, and/or viscous flow are dominant, negligible, or contributing at a similar order to one another. Thus the overall behavior for multiple fractures could be estimated in one figure.

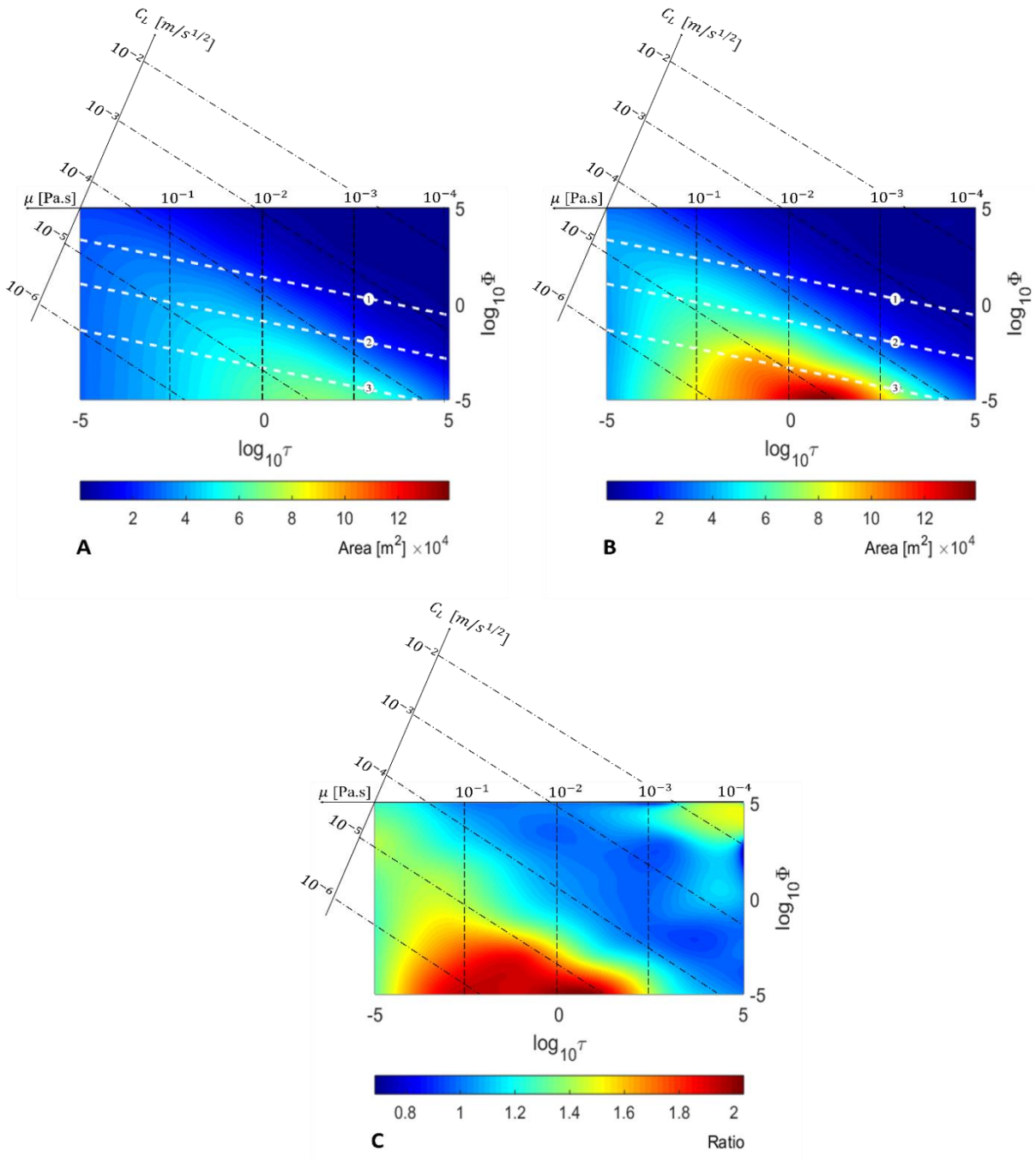

Figure B8: Total fracture area in all practical regimes. The total fracture area plotted as a function of log (τ) and log (Φ) for non-uniform and uniform space respectively: (A) uniform (B) non-uniform (C) ratio between non-uniform and uniform design. Here contours are shown of varying C_L and μ, with all other parameters according to Equation IV.4.

A great advantage is achieved in the non-uniform case, similar with the observation made in volume saving (**Figure IV.2** of main body). In detail, when viscosity is near 10^{-2} Pa.s and leak-off is around 10^{-5} $m \cdot s^{1/2}$; there is a more than 100% increase in fracture area. Modifying viscosity corresponds to moving through **Figure B8** along the white dashed lines numbered 1-3. **Figure B9** shows the fracture area obtained along each of these lines, $C_{L0} = 1 * 10^{-6}$, $2 * 10^{-6}$ and $1.5 * 10^{-5} m \cdot s^{\frac{1}{2}}$, which represents low (line 3 in **Figure B8**), intermediate (line 2 in **Figure B8**) and high (line 1 in **Figure B8**) permeability, respectively.

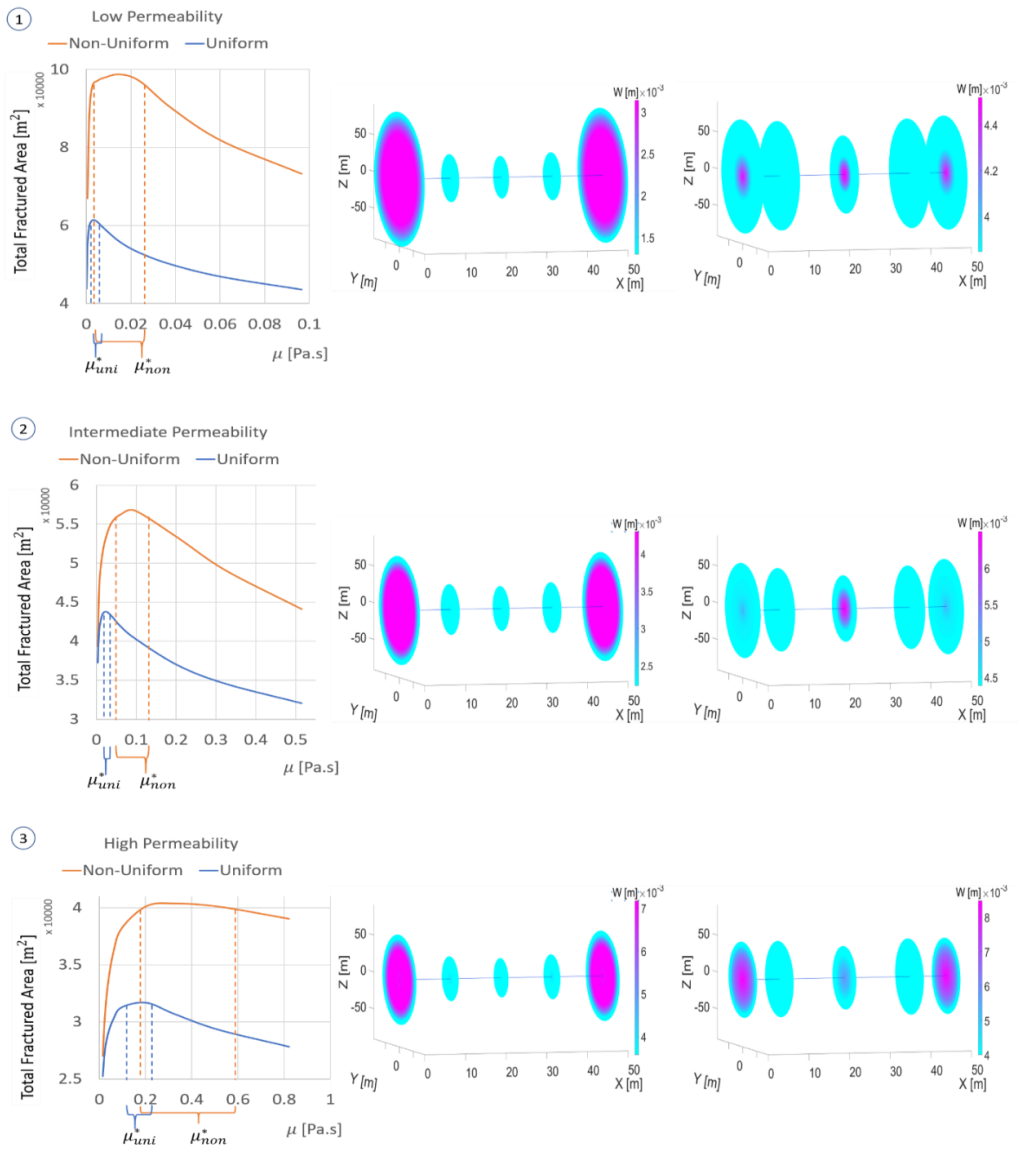

Figure B9: Comparison between the non-uniform and the uniform spacing. Total fractured area A of non-uniform (orange line) and uniform spacing (blue line) is compared at t =1000s. Results are shown for different C_{L0} represented as low, intermediate, and high permeability. The dashed arrow indicates the optimal range μ^*_{uni} and μ^*_{non} by 1% tolerance of the optimal viscosity μ_{op} which appear as a summit point of respective curve. The fracture geometry corresponding to the optimal viscosity case μ_{op} is illustrated by the 3D figures.

Overall, **Figure B8** demonstrates potential magnitude of improvement provided by optimization of treatment design. Firstly, we observe that fractured area is, as expected, generally higher for lower permeability. Additionally, it is demonstrated that there is one optimal viscosity existing for each combination of reservoir parameters, with higher optimum viscosity for higher permeability reservoirs. This optimal value results from a competition. On the one hand, there is a need for viscosity to be increased to reduce the leak-off, according to the inverse relationship between viscosity and C_L (**Equation B.2**). On the other hand, the increasing viscosity will promote more width, and hence smaller fracture area for a given injected volume. Additionally, because more width corresponds to more stress interaction among the fractures, there is a competition between efficiency and uniformity Cheng and Bunger (2019). Hence lower viscosity lead to higher fluid loss but more uniformity, while higher viscosity leads to lower fluid loss but higher non-uniformity. Optimal viscosity can therefore be understood to result from interplay of these competing trends, with an intuitively anticipated shifting toward higher viscosity for higher permeability rocks.

Besides the existence of an optimal viscosity that depends on reservoir properties, comparing the uniform and non-uniform spacing cases, non-uniform spacing is shown to give 30%-60% more fracture area at the optimal viscosity. This advantage arises from greater uniformity, as demonstrated in the 3D figures, where non-uniform spacing can be seen to promote more uniform growth. Details of the complex interplay among the growing fractures leading to this improved uniformity are discussed in a number of prior contributions Cheng and Bunger (2019a); Peirce and Bunger (2015); Cheng and Bunger (2019b).

It is important to realize that the potential benefit of non-uniform spacing goes beyond just higher fracture area at the optimum viscosity. Looking at each graph in **Figure B8**, it is apparent that the curvature is smaller in the vicinity of the optimum for non-uniform spacing. Indeed, this reduced sensitivity to variations in the viscosity in the neighborhood of the optimal viscosity is the most surprising, and possibly the most important, benefit observed in the comparison. To illustrate this, we define ratio A/A_{op} as a measure of closeness of a case to optimality (i.e. this ratio equals one at precisely the optimal combination of parameters). Based on such a criterion, we observe that no-matter what the reservoir permeability is, in non-uniform spacing, there exists a much wider range of viscosity that is nearly generating optimal fracture area. For example, choosing μ between 0.002 to 0.025 $Pa \cdot s$, that is between water and linear gel, results in 50% to 60% relative increase in the total fractured area at 1000 seconds with non-uniform spacing. In contrast, a narrow range of near optimality, from 0.001 to 0.003 Pa s, is given by uniform spacing. As will be discussed later, this wider optimal range could be very important in practice, where a variety of issues can lead to viscosity varying from its designed value.

F. Selected Basins

1. Information of Selected Basins

Four well-known basins are chosen as the objects of the illustrative case studies presented in the main body of the paper. Firstly, the Marcellus Formation is found in eastern North America, representing the closest natural gas to several high-population areas of East Coast. By early 2015, the Marcellus Shale was yielding about 14.4 billion cubic feet of natural gas per day, was the

source for over 36% of the shale gas produced in the United States and 18% of the total dry gas production of the United States EIA (2012). Secondly, the Ordos Basin, a 250,000 square kilometre area in northern China, the largest onshore gas producing basin in China, one of the world's five largest reserves of tight gas EIA (2011). Thirdly, the Permian Basin is considered, which gives its name to a large oil and natural gas producing area located in western Texas and southeastern New Mexico. It has been reported by the EIA that the oil production rate for that region up to 4 million barrels per day (MMb/d) EIA (2012) at January 2019. Finally, Texas' Eagle Ford formation has been one of the most actively drilled targets for unconventional oil in the world with over 17,000 wells EIA (2012). Input parameters for each basin are listed in the **Table B2**. Owing to the heterogeneous character, the values provided in Table B1 are representative averages for each basin. Note that leak-off coefficient C_L is computed using these values via **Equation 3**.

Table B2: Coefficients for Each Basin (EIA (2018); EIA (2014); EIA (2017); Yang et al. (2015); Ruppel (2019)).

Parameter (SI)	Permian Basin	Ordos Basin	Marcellus	Eagle Ford
k (permeability)	$1.23 * 10^{-16}\ m^2$	$2.47 * 10^{-17}\ \mathrm{m}^2$	$4.85 * 10^{-18}\ \mathrm{m}^2$	$9.88 * 10^{-20}\ \mathrm{m}^2$
ϕ (porosity)	6.0%	7.8%	9.3%	8.5%
p_Δ (differential pressure)	14 Mpa	13 Mpa	11 MPa	17 MPa
C_{L0} = C_L(μ= 1Pa.s)	$8.30 * 10^{-7}\ m/s^{\frac{1}{2}}$	$3.94 * 10^{-7}\ m/s^{\frac{1}{2}}$	$1.62 * 10^{-7}\ m/s^{\frac{1}{2}}$	$3.48 * 10^{-8}\ m/s^{\frac{1}{2}}$
C_L(μ=0.003 Pa.s, Water)	$1.52 * 10^{-5}\ m/s^{\frac{1}{2}}$	$7.15 * 10^{-6}\ m/s^{\frac{1}{2}}$	$2.95 * 10^{-6}\ m/s^{\frac{1}{2}}$	$6.35 * 10^{-7}\ m/s^{\frac{1}{2}}$

2. Basin Specific Study

In order to demonstrate the efficiency benefit of optimization for practical purposes, we consider simulations using the parameters from four well-known basins **(Table S2)**. The details of the basins and corresponding parameters are in the **Section S6.1**. Modifying viscosity corresponds to moving through **Figure IV.2** along the white dashed lines. **Figure B10(a)** shows the volume injected along each of these lines, which represents Permian Basin, Ordos Basin, Marcellus and Eagle ford, respectively.

To illustrate the potential for benefit associated with optimization, a non-uniformly spaced array ($h_1 = h_4 = 9\text{m}, h_2 = h_3 = 16\text{m}$) is again employed for comparison with uniformly spaced arrays (at 12.5m spacing). Fluid viscosity can span several orders of magnitude. For reference, **Figure B10(a)** shows labels corresponding approximately to several commonly used fluids, but of course varying formulation within these fluid families can lead to a continuum of possibilities. However, for reference, slick water is denoted with a viscosity around 0.003 Pa.s. Linear gel fracturing fluids are more viscous, for reference around 0.05 Pa.s. Note that a similar range can be obtained with large concentration of friction reducer. Crosslinked guar gel is denoted by viscosity around 0.5 Pa.s. Thus, the graphs are zoomed in on the must instructive range of viscosity 0.003-1 Pa.s.

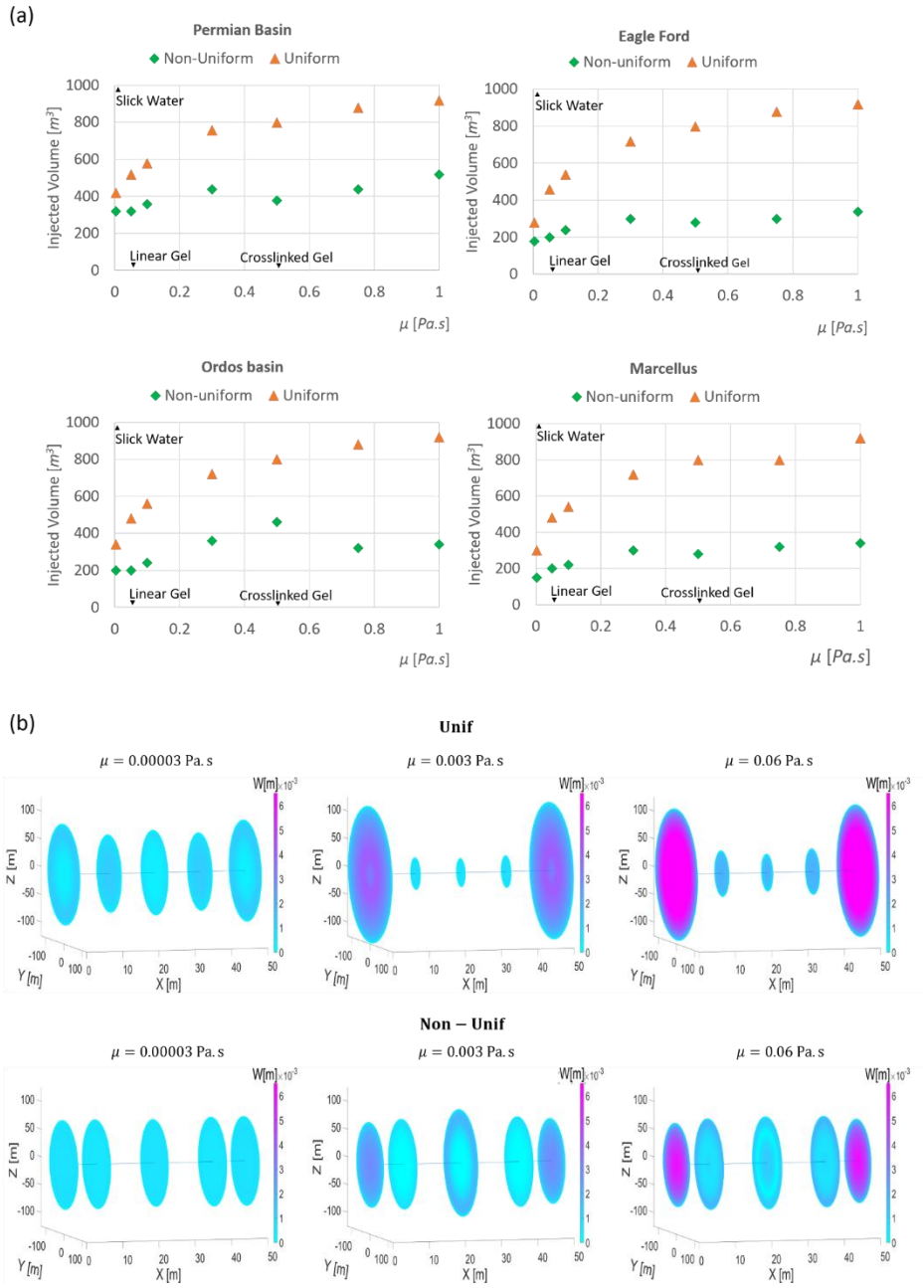

Figure B10: Comparison between the uniform and non-uniform space. (a) Total injected volume at A =100,000m2 for Eagle Ford, Marcellus, Ordos and Permian Basin. The triangle mark indicates the viscosity of slick water, linear gel and crosslinked gel. (b) Crack Propagation for uniform and non-uniform spacing at $\mu = 0.003$, 0.05 and 0.5 Pa.s for the Marcellus cases showing reduction in stress-shadow related fracture suppression in the non-uniform cases.

The first observation concerns the main impact of fluid viscosity, and it is best illustrated firstly by considering the uniform spacing cases in **Figure B10(a).** In general, for high viscosity, more volume is consumed to reach the same fracture area because high viscosity generates more crack opening and hence less fracture area per injected volume. For the selected basins, required fracture volume to achieve a desired fracture area increases monotonically with viscosity over the range considered. Hence it is apparent that choosing an optimal viscosity can have a significant impact on the required fluid volume for uniformly spaced hydraulic fractures. The benefit of slick water compared to crosslinked gel in all selected formations is on the order of a 50% savings in water use.

However, it is arguably more striking is that there is a huge volume savings potential associated non-uniform spacing (up to the point that benefits can be attenuated by in-situ variability, as discussed in the main body of the paper). For example, in the Marcellus, non-uniform spacing can give a required volume reduction of around 50% for slick water, about 60% for linear gel, and around 65% for crosslinked gel. A similar potential benefit is further anticipated in the Eagle Ford, Ordos Basin and Permian Basin, with quantitative differences but related to the same general phenomenon.

It is also observed that the benefits of choosing optimized viscosity are available across a much wider range of viscosities for the non-uniform spacing cases compared with the uniform spacing cases. This is in accordance to the previously observed lower sensitivity to variation of viscosity near the optimal value for non-uniform cases. Additionally, the advantages of non-uniform spacing becomes greater with increasing viscosity; as much as half volume is saved at 0.003 Pa.s, rising to 70% at 1 Pa.s.

The reason for the advantageous behavior of non-uniform spacing cases is explained with the assistance of 3D plots of fracture geometry, as shown in **Figure B10(b)**. Here the multiple fracture growth is shown for viscosities of 0.003, 0.05 and 0.5 Pa.s. The Z and Y axes represent the radial extension and color gradient represents the crack opening (aperture). The Marcellus is used here for illustrative purposes, noting a similar behavior is responsible for the impact of non-uniform spacing in other formations.

Examining **Figure B10(b)** indicates firstly that for uniform spacing, higher viscosity reduces leak-off and hence promotes more fracture growth, but the higher extension is not achieved for inner and middle fractures. Instead, these inner fractures are significantly suppressed. This behavior is due to the presence of increased interaction stress associated with higher viscosity cases, due mainly to higher fluid pressures accompanied by greater crack opening. By adjusting the spacing between the outer and inner fractures, higher stress is enforced on the outer fractures, giving a chance for others to develop. Hence, a much more uniform growth is obtained with more uniform fluid distribution, which is important for efficient utilization of injected materials. Indeed, such uniformity appears to be a very important factor in reducing fluid requirements for a desired fracture surface area.

Bibliography

Abass, H. H., Soliman, M. Y., Tahini, A. M., Surjaatmadja, J., Meadows, D. L., & Sierra, L. (2009). Oriented fracturing: A new technique to hydraulically fracture an openhole horizontal well. In Proceedings SPE Annual Technical Conference and Exhibition. New Orleans, LA, USA. SPE 124483.

Abou-Sayed A.S., Guo Q., Meng F., & Zaki K. (2003). Ultimate Capacity of a Disposal Well in Drilling Waste Injection Operations, in: Proceedings SPE/IADC Drilling Conference, Amsterdam, Netherlands, 2003.

Adachi, J., Siebrits, E., Peirce, A., & Desroches, J. (2007). Computer simulation of hydraulic fractures. *International Journal of Rock Mechanics and Mining Sciences,* 44, 739-757.

Adachi J. (2001). Fluid-Driven Fracture in Permeable Rock. PhD thesis. Minneapolis, MN, USA: University of Minnesota.

Baihly, J. D., Malpani, R., Edwards, C., Han, SY., Kok, J. C. L., Tollefsen, E. M., & Wheeler, C.W. (2010). Unlocking the shale mystery: How lateral measurements and well placement impact completions and resultant production. In Proceedings SPE Tight Gas Completions Conference. San Antonio, Texas, USA. SPE 138427.

Batchelor, G. K. (1976). Brownian diffusion of particles with hydrodynamic interaction. *Journal of Fluid Mechanics*, 74, 1–29.

Batchelor, G. K. (1967). An Introduction to Fluid Dynamics (Cambridge University Press, Cambridge, UK).

Brantley, S. L., Vidic, R. D., Brasier, K., Yoxtheimer, D., Pollak, J., Wilderman, C., & Wen, T. (2018). Engaging over data on fracking and water quality. Science. 359, 395-397.

Bunger, A. P. (2013). Analysis of the power input needed to propagate multiple HFs. *International Journal of Solids and Structures,* 50, 1538–1549.

Bunger, A. P., Jeffrey, R. G., & Zhang, X. (2014). Constraints on Simultaneous Growth of Hydraulic Fractures from Multiple Perforation Clusters in Horizontal Wells. *SPE Journal,* 19, 608-620.

Bunger, A.P., & Cardella, D.J. (2015). Spatial distribution of production in a Marcellus Shale well: Evidence for hydraulic fracture stress interaction, *Journal of Petroleum Science and Engineering*, 113, 162-166.

Bunger, A.P., Zhang, X., & Jeffrey, R.G. (2012). Parameters effecting the interaction among closely spaced HFs. *SPE Journal*, 17, 292–306.

Bunger, A.P., & Lecampion, B. (2017). 4 Critical Issues for Successful Hydraulic Fracturing Applications. In: Feng XT, editor. *Rock Mechanics and Engineering*: Balkema; Volume 5, ed., Chapter 16.

Carl T.M., Michael B.S. (2010). Hydraulic Fracturing: History of an Enduring Technology, *Journal of Petroleum Technology*, 62, 26-40.

Carter, E. (1957). in Optimum fluid characteristics for fracture extension. G. C. Howard, C. R. Fast, Eds. (Drilling and Production Practices), pp. 261–270.

Cheng, C., & Bunger, A. P. (2019). Optimizing Fluid Viscosity for Systems of Multiple Hydraulic Fractures. *AICHE Journal.* DOI:10.1002/aic.16564.

Cheng, C., & Bunger, A. P. (2019). Reduced order model for simultaneous growth of multiple closely-spaced radial hydraulic fractures. *Journal of Computational Physics*, 376, 228-248.

Cheng, C., & Bunger, A. P. (2016). Rapid Simulation of Multiple Radially-Growing HFs Using an Energy-Based Approach. *International Journal for Numerical and Analytical Methods in Geomechanics*, 71, 281–282.

Cheng, C., Bunger, A. P., & Peirce, A. P. (2016). Optimal Perforation Location and Limited Entry Design for Promoting Simultaneous Growth of Multiple Hydraulic Fractures, in: Proceedings SPE Hydraulic Fracturing Technology Conference, The Woodlands, Texas, United States, 9-11 February 2016. SPE 179158.

Cipolla, C., Weng, X., Onda, H., Nadaraja, T., Ganguly, U., & Malpani, R. (2011). New algorithms and integrated workflow for tight gas and shale completions. In Proceedings SPE Annual Technology Conference and Exhibition. Denver, Colorado, USA. SPE 146872.

Crouch, S. L., & Starfield, A. M. (1983). Boundary Element Methods in Solid Mechanics (George Allen & Unwin, London).

Crump, J. B., & Conway, M. W. (1988). Effects of perforation-entry friction on bottomhole treating analysis. Journal of Petroleum Technology, 15474, 1041–1049.

Damjanac, B., & Cundall, P. (2016). Application of distinct element methods to simulation of hydraulic fracturing in naturally fractured reservoirs. *Computers and Geotechnics*, 71, 283–94.

Desroches, J., Detournay. E., Lenoach, B., Papanastasiou, P., Pearson, J. R. A., Thiercelin, M., & Cheng, A. (1994). The crack tip region in hydraulic fracturing. *Proceedings of the Royal Society of London. Series A*, 447, 39–48.

Detournay, E. (2016). Mechanics of Hydraulic Fractures. *Annual Review of Fluid Mechanics*, 48, 311-339.

Detournay, E., & Peirce, A. (2014). On the moving boundary conditions for a hydraulic fracture. *International Journal of Engineering Science*, 84, 147–155.

Detournay, E. (2004). Propagation regimes of fluid-driven fractures in impermeable rocks. *International Journal of Geomechanics,* 4, 1–11.

Dontsov, E.V. (2016). An approximate solution for a penny shaped hydraulic fracture that accounts for fracture toughness, fluid viscosity and leak-off. *Royal Society Open Science.* 3, 160737

Dontsov, E.V., & Peirce, A.P. (2017). A multiscale implicit level set algorithm (ILSA) to model hydraulic fracture propagation incorporating combined viscous, toughness, and leak-off asymptotics. *Computer Methods in Applied Mechanics and Engineering,* 313, 53-84.

Economides, M., & Nolte, K.G. (2000). Reservoir Stimulation, John Wiley & Sons.

Ellsworth, W. L. (2013). Injection-Induced Earthquakes. *Science.* 341, 142-149.

Energy Information Administration. (2018). Permian Basin Wolfcamp Shale Play Geology review. 2018.

Energy Information Administration. (2017). Marcellus Shale Play Geology review.

Energy Information Administration. (2014). Marcellus Updates to the EIA Eagle Ford Play Maps.

Energy Information Administration. (2012). Annual Energy Outlook 2012.

Energy Information Administration. (2011). World Shale Gas Resources: An Initial Assessment of 14 Regions Outside the United States; EIA, International Energy Statistics; Freedom House, Freedom in the World.

Energy Information Administration. (2020). Natural Gas Gross Withdrawals and Production.

Energy Information Administration. (2020). Tight oil production estimates by play.

Entrekin, S., Trainor, A., Saiers, J., Patterson, L., Maloney, K., Fargione, J., Kiesecker, J., Baruch-Mordo, S., Konschnik, K., Wiseman, H., Nicot, J. P., & Ryan, J. N. (2018). Water Stress from High-Volume Hydraulic Fracturing Potentially Threatens Aquatic Biodiversity and Ecosystem Services in Arkansas, United States. *Environmental Science & Technology, 52*, 2349-2358.

Fischer, T., & Guest, A. (2011). Shear and tensile earthquakes caused by fluid injection. *Geophysical Research Letters,* 38. L045447.

Fisher, M. K., Heinze, J. R., Harris, C. D., Davidson, B. M., Wright, C. A., & Dunn, K. P. (2004). Optimizing horizontal completion techniques in the Barnett shale using microseismic fracture mapping. In Proceedings SPE Annual Technology Conference and Exhibition. Houston, Texas, USA. SPE 90051.

Fisher, M., Wright, C., Davidson, B., Goodwin, A., Fielder, E., Buckler, W., & Steinsberger, N. (2002). Integrating fracture mapping technologies to optimize stimulations in the Barnett Shale.In SPE Annual Technical Conference and Exhibition. San Antonio, Texas. SPE 77441;

Garagash, D. (2000). Hydraulic fracture propagation in elastic rock with large toughness. in Pacific Rocks 2000 'Rock around the rim', J. Girard, M. Liebman, C. Breeds, T. Doe, Eds (A.A. Balkema, Rotterdam), pp. 221-228.

Garagash, D.D., & Detournay, E. (1999). The Tip Region of a Fluid-Driven Fracture in an elastic medium. *Journal of Applied Mechanics,* 67,183-192.

Germanovich, L.N., Ring, L.M., Astakhov, D.K., Shlyapobersky, J., & Mayerhofer, M.J. (1997). Hydraulic fracture with multiple segments - I: Observations and model formulation, *International Journal of Rock Mechanics and Mining Sciences,* 34, 98e1-98e15.

Guglielmi, Y., Cappa, F., Avouac, J.P., Henry, P., & Elsworth, Derek. (2015). Seismicity triggered by fluid injection–induced aseismic slip, *Science*, 348, 1224-1226.

He,Y., Flynn, S. L., Folkerts, E. J., Zhang, Y., & Goss, Greg. G. (2017). Chemical and toxicological characterizations of hydraulic fracturing flowback and produced water. *Water Research,* 114, 78-87.

Howard, G. C., & Fast, C. R. (1970). Hydraulic fracturing. New York, Society of Petroleum Engineers.

Irwin, G. R. (1957). Analysis of stresses and strains near the end of a crack traversing a plate. *ASME. Journal of Applied Mechanics,* 24, 361–364.

Izadi, M., & Dubljevic, S. (2013). Order-reduction of parabolic PDEs with time-varying domain using empirical eigenfunctions, *AICHE Journal*, 59, 4142-4150.

Izadi, M., & Dubljevic, S. (2013). Computation of empirical eigenfunctions of parabolic PDEs with non-trivial time-varying domain, in: Control Conference (ECC), European, 53-58.

Jeffrey, R.G., Bunger, A.P., Lecampion, B., Zhang, X., Chen, Z., van, As A., Allison, D. P., De Beer, W., Dudley, J. W., Siebrits, E., Thiercelin, M., & Mainguy, M. (2009). Measuring Hydraulic Fracture Growth in Naturally Fractured Rock, in: Proceedings SPE Annual Technology Conference and Exhibition, New Orleans, Louisiana, USA.

Kanninen, M. F., & Popelar, C. H. (1985). Advanced Fracture Mechanics, in Oxford Engineering Science Series, (Oxford Univ. Press, Oxford, UK), vol. 15.

Kargbo, D. M., Wilhelm, R. G., & Campbell, D. J. (2010). Natural Gas Plays in the Marcellus Shale: Challenges and Potential Opportunities. *Environmental Science & Technology,* 44, 5679-5684.

Khristianovich, S.A., & Zheltov, Y.P. (1955). Formation of Vertical Fractures by Means of Highly Viscous Liquid, Proc., Fourth World Pet. Congress, Rome 2, 579–586.

Kondash, A. J., Lauer, N. E., & Vengosh, A. (2018). The intensification of the water footprint of hydraulic fracturing. *Science Advances,* 4, 5982-5990.

Kresse, O., Weng, X., Gu, H., & Wu, R. (2013). Numerical Modeling of Hydraulic Fractures Interaction in Complex Naturally Fractured Formations, *Rock Mechanics and Rock Engineering,* 46, 555-568.

King, G.E. (2012). Hydraulic fracturing 101: what every representative, environmentalist, regulator, reporter, investor, university researcher, neighbor, and engineer should know about hydraulic fracturing risk. *Journal of Petroleum Technology,* 64, 34-42.

Laurenzi, I. J., & Jersey, G. R. (2013). Life Cycle Greenhouse Gas Emissions and Freshwater Consumption of Marcellus Shale Gas. *Environmental Science & Technology,* 47, 4896-4903.

Lecampion, B., Bunger, A. P., & Zhang, X. (2017). Numerical methods for hydraulic fracture propagation: A review of recent trends. *Journal of Natural Gas Science and Engineering,* 49, 66-83.

Lecampion, B., & Desroches, J. (2015). Simultaneous initiation and growth of multiple radial hydraulic fractures from a horizontal wellbore. Journal of the Mechanics and Physics of Solids, 82, 235–258.

Lecampion, B., & Detournay, E. (2007). An implicit algorithm for the propagation of a hydraulic fracture with a fluid lag. *Computer Methods in Applied Mechanics and Engineering,* 196, 4863-4880.

Lecampion, B., Desroches, J., Weng, X., Burghardt, J., & Brown, J.E. (2015). Can We Engineer Better Multistage Horizontal Completions? Evidence of the Importance of Near-Wellbore Fracture Geometry From Theory, Lab and Field Experiments, in: Proceeding SPE Hydraulic Fracturing Technology Conference, The Woodlands, Texas, USA, SPE 173363.

Lecampion, B., & Detournay, E. (2007). An implicit algorithm for the propagation of a hydraulic fracture with a fluid lag. *Computer Methods in Applied Mechanics and Engineering.* 196, 4863-4880.

Mendelsohn, D.A. (1984). A review of hydraulic fracture modeling—part I: general concepts, 2D models, motivation for 3D modeling. *Journal of Energy Resources Technology.* 106, 369-376.

Meyer, B., & Bazan, L. (2011). A discrete fracture network model for hydraulically induced fractures-theory, parametric and case studies. In Proceedigs SPE Hydraulic Fracturing Technology Conference and Exhibition. The Woodlands, Texas, USA. SPE 140514.6.

Miller, C., Waters, G., & Rylander, E. (2011). Evaluation of production log data from horizontal wells drilled in organic shales. In SPE North American Unconventional Gas Conference and Exhibition, The Woodlands, Tx, USA, 14-16 June 2011. SPE 144326.

Mitchell, A. L., Small, M., & Casman, E. A. (2013). Surface water withdrawals for Marcellus Shale gas development: Performance of alternative regulatory approaches in the Upper Ohio River Basin. *Environmental Science & Technology,* 47, 12669−12678.

Montgomery, C. T. (2013). Fracturing Fluids. In A. P. Bunger, J. McLennan, R. G. Jeffrey, (Eds.), Effective and Sustainable Hydraulic Fracturing. Chapter 1. Rijeka, Croatia: Intech.

Narasingam, A., & Kwon, J.S.I. (2017). Development of local dynamic mode decomposition with control: Application to model predictive control of hydraulic fracturing, *Computers & Chemical Engineering,* 106, 501-511.

Narasingam, A., Siddhamshetty, P., & Kwon, J.S.I. (2017). Temporal clustering for order reduction of nonlinear parabolic PDE systems with time-dependent spatial domains: Application to a hydraulic fracturing process, *AICHE Journal,* 63, 3818-3831.

National Research Council. (2013). Induced seismicity potential in energy technologies. National Academies Press.

Nordgren, R.P. (1972). Propagation of a Vertical HF, *SPE Journal*, 12, 306–314.

Olson, J., & Pollard, D.D. (1989). Inferring paleostresses from natural fracture patterns: A new method. *Geology*, 17, 345-348.

Olson, J.E. (1995). Fracturing from Highly Deviated and Horizontal Wells: Numerical Analysis of Non-planar Fracture Propagation, in: Proceedings Low Permeability Reservoirs Symposium, Denver, Colorado, SPE 29573.

Olson, J.E., & Dahi-Taleghani, A. (2009). Modeling simultaneous growth of multiple hydraulic fractures and their interaction with natural fractures, in: Proceeding Society of Petroleum Engineers - SPE Hydraulic Fracturing Technology Conference, The Woodlands, Texas, United States, SPE 119739.

Olson, J.E. (2008). Multi-fracture Propagation Modeling: Applications to Hydraulic Fracturing in Shales and Tight Gas Sands, in: Proceedings of 42nd US Rock Mechanics Symposium, San Francisco, California, 08-327.

Peirce, A. P., & Bunger, A. P. (2015). Interference Fracturing: Non-Uniform Distributions of Perforation Clusters that Promote Simultaneous Growth of Multiple HFs. SPE Journal, 20, 384-395

Peirce, A. P., & Detournay, E. (2008). An implicit level set method for modeling hydraulically driven fractures. *Computer Methods in Applied Mechanics and Engineering,* 197, 2858-2885.

Perkins, T.K., & Kern L.R. (1961). Widths of HFs. *Journal of Petroleum Technology*, 13, 937–949.

Regenauer, L.K., Bunger, A.P., Chua, H.T., Dyskin, A., Fusseis, F., Gaede, O., Jeffrey, R.G., Karrech, A., Kohl, T., Liu, J., Lyakhovsky, V., Pasternak, E., Podgorney, R., Rahman, S., Schrank, C., Trefry, M., Veveakis, M., Wu, B., Yuen D., Wellmann, F., & Zhang, X. (2015). Deep Geothermal: The 'Moon Landing' Mission in the Unconventional Energy and Minerals Space, *Journal of Earth Science,* 26, 2-10.

Rice, J. R. (1968). in Fracture: An Advanced Treatise, H. Liebowitz, Ed. (Academic Press, New York), vol. 2, chap. 3. pp. 191-311.

Roussel, N.P., Manchanda, R., & Sharma, M.M. (2012). Implications of Fracturing Pressure Data Recorded during a Horizontal Completion on Stage Spacing Design, in: Proceeding SPE Hydraulic Fracturing Technology Conference, The Woodlands, Texas, USA, SPE 152631.

Ruppel, S. (2019). Stratal Architecture and Facies Development in a Middle Wolfcampian Platform Carbonate Reservoir: University Block 9 Field, Andrews County, Texas.

Savitski, A. A., & Detournay, E. (2002). Propagation of a penny-shaped fluid-driven fracture in an impermeable rock: asymptotic solutions. *International Journal of Solids and Structures,* 39, 6311–6337.

Scanlon, B. R., Reedy, R. C., & Nicot, J. P. (2014). Will water scarcity in semiarid regions limit hydraulic fracturing of shale plays? *Environmental Research Letters,* 9, 124011-124025.

Sesetty, V., & Ghassemi, A. (2013). Numerical simulation of sequential and simultaneous hydraulic fracturing. In A. P. Bunger, J. McLennan, R. G. Jeffrey, (Eds.), Effective and Sustainable Hydraulic Fracturing. Chapter 33. Rijeka, Croatia: Intech.

Shrestha, N., Chilkoor, G., Wilder, J., Gadhamshetty, V., & Stone, J. J. (2017). Potential water resource impacts of hydraulic fracturing from unconventional oil production in the Bakken shale. *Water Research,* 108, 1-24.

Sidhu, H.S., Narasingam, A., Siddhamshetty, P., & Kwon, J.S.I. (2018). Model order reduction of nonlinear parabolic PDE systems with moving boundaries using sparse proper orthogonal decomposition: Application to hydraulic fracturing, *Computers & Chemical Engineering,* 112, 92-100.

Slocombe, R., Acock, A., Fisher, K., Viswanathan, A., Chadwick, C., Reischman, R., & Wigger, E. (2013).Eagle Ford completion optimization using horizontal 32 log data. In Proceedings SPE Annual Technology Conference and Exhibition, New Orleans, Lousiana, USA

Smakhtin, V., Revenga, C., & Doll, P. (2004). A pilot global assessment of environmental water requirements and scarcity. *Water International,* 29, 307−317.

Sneddon, I. N. (1951). Fourier Transforms (McGraw-Hill, New York).

Sneddon, I. N. (1946). The distribution of stress in the neighborhood of a crack in an elastic solid. *Proceedings of the Royal Society of London. Series A,* 187, 229-260.

Spence, D.A., & Sharp, P.W. (1985). Self-similar solution for elastohydrodynamic cavity flow. *Proceedings of the Royal Society of London. Series A,* 400, 289–313.

Spencer, A.J.M. (1992). Continuum Mechanics (1st edition). Dover: Courier Corporation.

Sun, M., Lowry, G. V., & Gregory, K. B. (2013). Selective oxidation of bromide in wastewater brines from hydraulic fracturing. *Water Research,* 47, 3723-3731.

Vafi, K., & Brandt, A. (2016). GHGfrack: An Open-Source Model for Estimating Greenhouse Gas Emissions from Combustion of Fuel during Drilling and Hydraulic Fracturing. *Environmental Science & Technology*, *50*, 7913-7920.

Vengosh, A., Jackson, R. B., Warner, N., Darrah, T. H., & Kondash, A. A. (2014). Critical Review of the Risks to Water Resources from Unconventional Shale Gas Development and Hydraulic Fracturing in the United States. *Environmental Science & Technology,* 48, 8334-8348.

Warpinski, N., Kramm, R.C., Heinze, J.R., & Waltman, C.K. (2005). Comparison of single-anddual-array microseismic mapping techniques in the Barnett Shale. In SPE Annual TechnicalConference and Exhibition, Dallas, Texas. SPE 95568;

Weng, X. (1993). Fracture Initiation and Propagation From Deviated Wellbores. Society of Petroleum Engineers. doi:10.2118/26597-MS.

Wong, S.W., Geilikman, M., & Xu, G. (2013). Interaction of multiple hydraulic fractures in horizontal wells. In SPE Unconventional Gas Conference and Exhibition. Society of Petroleum Engineers. Muscat, Oman.

Wu, K., & Olson J.E. (2013). Investigation of critical in situ and injection factors in multifrac treatments: Guidelines for controlling fracture complexity, in: Proceeding SPE Hydraulic Fracturing Technology Conference, The Woodlands, Texas, SPE 163821.

Xiong, B., Zydney, A. L., & Kumar, M. (2016). Fouling of microfiltration membranes by flowback and produced waters from the Marcellus shale gas play. *Water Research,* 99, 162-170

Yang, H., Liu, X., Yan, X., & Zhang, H. (2015). Discovery and reservoir-forming geological characteristics of the Shenmu Gas Field in the Ordos Basin. *Natural Gas Industry B,* 24, 295-306.